DEVELOPMENT OF MEMS-BASED CHEMICAL PRE-CONCENTRATORS WITH INTEGRATED SENSING UNITS FOR ANALYSIS OF GAS-PHASE VOLATILE ORGANIC COMPOUNDS

A Thesis
Presented to
The Academic Faculty

by

Christopher John Carron

In Partial Fulfillment
of the Requirements for the Degree
Masters in the
School of Electrical and Computer Engineering

Georgia Institute of Technology
August 2015

THE DEVELOPMENT OF MEMS-BASED CHEMICAL PRE-CONCENTRATORS WITH INTEGRATED SENSING UNITS FOR ANALYSIS OF GAS-PHASE VOLATILE ORGANIC COMPOUNDS

Approved by:

Dr. Oliver Brand, Advisor
School of Electrical and Computer Engineering
Georgia Institute of Technology

Dr. Muhannad Bakir
School of Electrical and Computer Engineering
Georgia Institute of Technology

Dr. Bruno Frazier
School of Electrical and Computer Engineering
Georgia Institute of Technology

Date Approved: July 20, 2015

To Tressa

ACKNOWLEDGEMENTS

I wish to thank Dr. Oliver Brand for his patient and unwavering support. These last several years have been very trying for my family and me, and he has been patient, kind, and understanding throughout. Additionally, I thank Dr. Muhannad Bakir and Dr. Bruno Frazier for their willingness to serve on my committee and offer their feedback and guidance. I also wish to thank the IEN staff for their technical support and advice. I would specifically like to thank Harley Hayden and C.S. Pai for their help in improving several aspects of the metal deposition processing used in this work. I would also like to specifically thank Ben Hollerbach for his help in developing the partial dicing technique. Special thanks are also in order for Patrick Getz, who improved the measurement capabilities of our custom gas system, and for Mingu Kim and his help and encouragement in developing the first ‘no flow’ pre-concentration tests. Finally, my deepest gratitude to Tressa and my children who gave me hope and courage to soldier on through this the most difficult and terrifying period of my life.

TABLE OF CONTENTS

LIST OF TABLES

Page

LIST OF FIGURES

Page

LIST OF EQUATIONS

Page

LIST OF SYMBOLS AND ABBREVIATIONS

BOX	buried oxide
DCM	dichloromethane
DIL	dual in-line
DMM	digital multimeter
DRIE	deep reactive ion etching
EPCO	ethylene co-propylene
FEA	finite element analysis
GC	gas chromatography
KOH	potassium hydroxide
LoD	limit of detection
µ-	micro-
µTPC	micro thermal pre-concentrator
MEMS	micro electro-mechanical systems
MFC	mass flow controller
PDMS	polydimethylsiloxane
PECH	polyepichlorohydrin
PIB	polyisobutylene
PVAc	poly-vinyl acetate
SEM	scanning electron microscope
SiO_2	silicon dioxide
SOI	silicon-on-insulator
VOC	volatile organic compound

SUMMARY

A MEMS-based micro thermal pre-concentration (μTPC) system for enhanced detection of gas phase volatile organic compounds (VOCs) is presented. The system implements a suspended membrane geometry, enhancing thermal isolation and enabling high temperature elevations even for low levels of heating power. The membranes have a large surface area-to-volume ratio but low thermal mass (and therefore, low thermal time constant), with arrays of 3-D high aspect-ratio features formed via DRIE of silicon. Integrated onto the membrane are sets of diffused resistors designed for performing thermal desorption (via joule heating) and for measuring the temperature elevation of the device due to the temperature-dependent resistivity of doped silicon.

The novel system features integrated real-time chemical sensing technology, which allows for reduced sampling time and a reduced total system dead volume of approximately 10 μL. The system is capable of operating in both a traditional gas-flow setup and also in a static atmosphere which requires no external fluidic flow system, thereby enabling novel measurement methods and applications. The ability to operate without a forced-flow fluidic system is a distinct advantage and can considerably enhance the portability of a sensing system, facilitating deployment on mobile airborne platforms as well as long-term monitoring stations in remote locations.

Finally, the real-time measurement capabilities of the integrated chemical sensors allow for transient analysis of thermally generated signals, which has been demonstrated to improve analyte discrimination for VOCs without the need for a separation column or external fluidic system Initial tests of the system have demonstrated a pre-concentration factor of 50% for toluene.

CHAPTER 1 – INTRODUCTION

We live in an information-rich era that has come to expect ubiquitous on-demand data delivered at low cost to mobile platforms. This drive for ever-increasing amounts and types of data has expanded to include chemical and biological information, with the hope that such data hold keys to improving our lives. As a result of this motivation, recent years have seen increased interest and activity in the area of micro-sized chemical sensors, which are both portable and low-cost [1-14]. The purpose of this research is to develop MEMS-based chemical sensing systems suitable for use in mobile platforms, to meet the growing need for real-time on-site chemical analyses. Specifically, this research presents the development of a MEMS-based micro thermal pre-concentration (μTPC) system for enhanced detection of volatile organic compounds (VOCs) in the gas phase. The novel system features integrated chemical sensing technology, which can be used to improve the performance of previously developed cantilever-based resonant micro-sensors and enables novel modes of operation without the need of an external fluidic system. Initial tests of the system have demonstrated a pre-concentration factor of 50% for toluene.

All chemical sensors are constrained by an inherent limit of detection (LoD), and are incapable of reliably detecting chemical species at concentrations below this limit [3, 4, 15-19]. The LoD for a cantilever-based resonant chemical sensor is defined as three times the noise-equivalent analyte concentration (Equation 1), which can be approximated by

$$LoD = 3\frac{\Delta f_{min}}{S}$$

Equation 1 – Limit of detection for resonant cantilever sensors.

where Δf_{min} is the lowest detectable frequency change (determined by the noise and stability) and S is the sensitivity determined by sorption into a sorbent coating [20]. From Equation 1, it is clear that the LoD (i.e. minimum detectable concentration) can be improved by increasing either the Q-factor of the resonator (i.e. by decreasing Δf_{min}) or the sensitivity, or both, and that an arbitrarily low LoD can be achieved by doing so

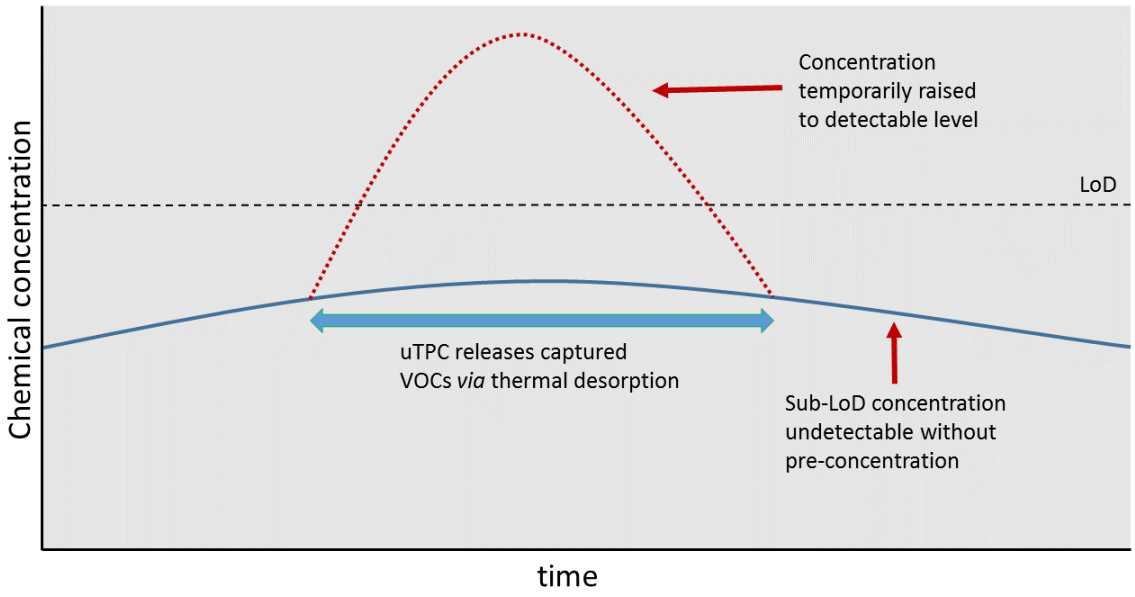

Figure 1 – Graphical representation demonstrating how chemical pre-concentration can improve the effective LoD for chemical sensors, enabling detection of sub-LoD concentration levels that would otherwise be undetectable by the sensor alone.

Alternatively, chemical pre-concentration systems can improve the effective LoD of chemical sensors by accumulating target chemical species at sub-LoD concentrations over time and rapidly releasing them within the vicinity of the chemical sensor [3, 4, 15, 16, 21-24]. This rapid release of captured analytes can temporarily raise the chemical concentration above the sensor's inherent LoD, enabling measurement (Figure 1). Through analysis of the accumulation and release cycle times and the measured concentration spike,

the previously undetectable sub-LoD concentration can be deduced, effectively enabling the system to detect concentrations below the theoretical LoD of the chemical sensor alone [3, 4, 15, 16, 18, 19, 21-23].

Various chemical and biological pre-concentration systems have been developed by several groups in the academic and commercial communities, for a wide range of applications [1, 3, 4, 17-19, 21-25]. This work focuses on those that can be categorized as μTPCs used to enhance detection of VOCs in the gas phase. Specifically, a μTPC in this context is a MEMS-based chemical pre-concentration device which utilizes rapid thermal cycling to purge target chemical compounds from an active sorbent layer, in a process known as thermal desorption [3, 4, 18, 19, 22, 23, 26, 27]. Thermal desorption is typically performed just prior to the μTPC reaching full saturation, to maximize the amount of VOCs -- and thus the concentration -- released into the vicinity of the corresponding chemical sensor. The term 'dead volume' is often used to refer to the fixed volume surrounding the sensor, which includes the chamber volumes of the sensor and μTPC as well as the adjacent volumes introduced by interconnect tubing and valves due to interfacing with an external gas flow system [3, 4, 18, 21, 23, 24, 27-29].

A key objective of μTPC design is to minimize the dead volume so that the transient concentration spike due to thermal desorption is maximized [22, 28, 29]. Minimizing the thermal time constant of the μTPC is also preferable, as this reduces the temporal width of the thermal desorption event, which in turn maximizes the peak height of the concentration spike [30-35]. Other design considerations include minimizing the pressure drop across the device – so that it can operate without the need for a high-pressure gas cylinder – and maximizing the 'breakthrough volume' [14, 17, 29, 36]. Breakthrough volume refers to the

volume of analyte-loaded gas at a fixed concentration that must pass over the μTPC before it becomes saturated [4, 23, 24, 27, 29, 37, 38]. The breakthrough volume can be maximized by increasing the sorbent-coated inner surface area that comes into contact with the analyte-loaded gas stream, and by using sorbent materials with either high partition coefficients or high specific surface area, as discussed below [3, 4, 18, 23, 24, 27, 39]. For a given fixed device volume, there is often a compromise between decreasing the pressure drop and increasing the breakthrough volume as it becomes increasingly difficult to force gas flow through areas of densely packed sorbent material which are necessary for capturing large amounts of VOCs. Finally, the most important metric for μTPC design is the pre-concentration factor, which is defined as the ratio of the peak concentration during thermal desorption to the original concentration during accumulation [3, 4, 19, 24, 26, 40, 41].

Typically, the specific target application determines the desired thermal desorption temperature, as various gas-phase species desorb at different temperatures from a given sorbent based on the vapor pressure and boiling point of the compounds and interaction between the analyte and sorbent [3, 27-29, 34, 37, 42-48]. This property also enables arrays of μTPC devices to perform coarse pre-filtering of samples by coating each device in the array with a sorbent which targets a specific class of VOC compounds [2, 27, 29, 34, 42]. When a complex gas mixture is introduced into the array, individual compounds segregate and partition by class into separate devices in the array. Individual addressing of devices during thermal desorption enables the various classes of compounds to be desorbed at different times, thereby accomplishing an initial rough temporal separation prior to chemical measurement. In applications where the μTPC is used for injection into a GC

system, coarse pre-filtering in this manner can enhance separation of co-eluting compounds and improve the overall performance of the system [30, 34, 39, 42, 49-56].

The choice of sorbent materials used in a μTPC device can vary widely, and depends on the properties of the target VOC analytes, desired thermal desorption temperature, and whether the pre-concentration approach is exhaustive or equilibrium-based [15, 17, 18, 21, 28, 30, 31, 42, 49, 57-63]. With an exhaustive μTPC approach, the design goal is to capture all target VOCs in the sample volume, typically through the use of a high-surface area activated carbon sorbent layer, and perform thermal desorption once the sorbent layer approaches saturation [14, 15, 17, 23, 28, 29, 32-36, 46, 48, 51, 56, 63-68]. Equilibrium μTPCs are also designed to initiate thermal desorption just prior to saturation, but no attempt is made to capture all of the VOCs flowing past the device. Rather, thermal desorption is initiated when an equilibrium is reached between the sample concentration in the chamber and the concentration of VOCs in the sorbent layer of the μTPC [18, 21, 39, 42, 49, 55, 57-62, 69-73]. This equilibrium point is determined by the partition coefficient of the given sorbent material and the corresponding target VOC concentrations as they diffuse into the sorbent [16, 27, 61, 72, 74-78]. Equilibrium μTPCs typically utilize thin-film polymer-based sorbents, such as polydimethylsiloxane (PDMS) and Tenax TA, rather than the activated carbon sorbents employed in an exhaustive μTPC system [15, 17, 32-35, 63, 68].

Often, a μTPC interfaces with a downstream gas chromatography (GC) system and serves to inject concentrated VOC samples into the GC separation column [34, 42, 49-52, 79-83]. Operation of arrayed or cascaded μTPC devices, in combination with appropriate sorbent choices for target VOCs, can enable rough pre-filtering of sample analytes (e.g.,

based on vapor pressure differences) prior to analysis or injection into the GC system, which can improve measurement cycle time and precision of the system as a whole [30, 39, 48, 53-56]. Due to their small size, μTPCs are capable of operating at low power and can be combined directly with existing MEMS-based sensor technologies and micro-GC systems for deployment on mobile platforms, enabling novel applications for real-time on-site data collection [34, 35, 51, 68, 80-82, 84, 85].

The specific focus of this work is to develop a novel equilibrium-based μTPC system that is integrated on-chip with existing resonant cantilever-based chemical sensors developed at Georgia Tech. The integrated design improves the effective LoD of the cantilever-based chemical sensors, enhancing their effective sensitivity, and enables measurements to be completed within in a few seconds of thermal desorption, improving significantly on reported measurement cycle times for state-of-the-art systems demonstrated in the literature. For example, subsequent analysis of VOCs via separation downstream in a conventional GC column can require the sample to be transported off-site to a dedicated testing facility, precluding applications where immediate real-time data is the highest priority (e.g., clinical monitoring of patient in critical condition, quarantine of a developing hazardous situation) [9, 15, 17, 18, 26, 34, 35, 39, 50, 51, 66, 68, 80, 81, 84-88]. Portable GC systems have recently been demonstrated, but still require tens of minutes to perform a measurement or require complex fluidic control systems with costly reagents, support fluids and high-pressure gas cylinders [15, 17, 23, 51, 84]. The integrated sensing platform presented in this work can perform measurements in less than 30 seconds and is capable of operating in both a traditional gas-flow setup and also in a static atmosphere which requires no external fluidic flow system, thereby enabling novel measurement

methods and applications. The ability to operate without a forced-flow fluidic system is a distinct advantage and can considerably enhance the portability of a sensing system, facilitating deployment on mobile airborne platforms as well as long-term monitoring stations in remote locations.

Furthermore, since ideal operation of a µTPC requires thermal desorption to occur just below the saturation point of the sorbent-analyte combination, real-time knowledge of the VOC uptake rate into the sorbent of the µTPC is desirable. The rapid measurement cycling of the proposed design enables more accurate tracking of the saturation state of the µTPC, which can be used to improve overall system performance. For example, if multiple sequential measurement cycles reveal that the µTPC was saturated when thermal desorption occurred, the next measurement can reduce the µTPC accumulation time until the µTPC is being operated just below full saturation. Since the cycle time for this system is on the order of seconds (rather than minutes or hours), the saturation loading state of the µTPC can be tracked essentially in real-time, ensuring that the system is operating in an optimal state. Finally, the real-time measurement capabilities of the integrated chemical sensors allow for transient analysis of thermally generated signals, which has been demonstrated to improve analyte discrimination for VOCs without the need for a separation column or external fluidic system [74, 89].

CHAPTER 2 – DESIGN & SIMULATION

To achieve the stated design goals necessary for optimal pre-concentration – low dead volume, high breakthrough volume, low thermal time constant, and high temperature elevation with low power consumption – the system demonstrated here implements a suspended membrane geometry formed from an SOI substrate. This design choice has the advantage of enhancing thermal isolation of the device and enabling relatively high temperature elevations even for low levels of applied heating power. The membrane is designed to have a large surface area-to-volume ratio but low thermal mass (and therefore, low thermal time constant), with arrays of 3-D high aspect-ratio ridges and pillars on the back surface formed via DRIE of silicon. Integrated onto the front surface of the membrane are sets of diffused resistors which are designed for performing thermal desorption (via joule heating) and for measuring the temperature elevation of the device due to the temperature-dependent resistivity of doped silicon (Figure 2).

This approach combines into one cohesive whole the individual strengths from various μTPC devices presented in the literature. For example, some groups have implemented a membrane structure – which provides excellent thermal isolation, enabling rapid heating and low-power operation – but did not incorporate high aspect-ratio 3D features necessary to achieve a high surface-area-to-volume ratio [3, 90]. As a result, the pre-concentration factor for such designs is limited due to the low surface area available for sorbent placement. Other groups avoided a membrane structure and instead focused on fabrication simplicity, which in turn minimizes dead volume and maximizes surface area and sorbent capacity [15, 17, 18, 28, 30, 31, 39, 42, 49, 91]. This approach, however, has the disadvantage of increased thermal mass – which leads to longer thermal time constants –

and reduced thermal isolation which ultimately limits the practical thermal desorption temperature and requires higher power consumption to achieve the same thermal desorption temperature as a membrane-based device. Similar to both groups, the design presented here implements arrays of individually-addressable µTPC devices which enables coarse pre-filtering by desorption of each device in the array one at a time. The final design resulted in a packaged dead volume (i.e. inner chamber volume) of approximately 10 µL, a thermal time constant of less than one second and a temperature elevation in excess of 200ºC for less than one watt of applied heating power. Additionally, experimental results have demonstrated an initial proof-of-concept pre-concentration factor of 50% for toluene when operated in a novel no-flow setup.

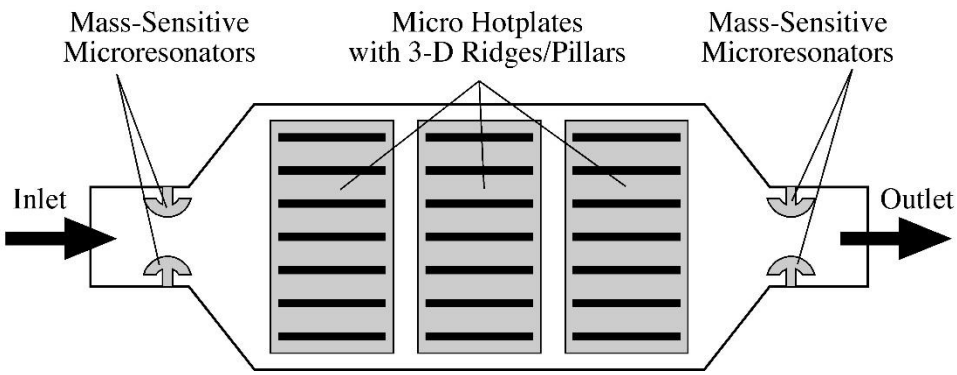

Figure 2 - Graphical representation of pre-concentrator concept, with array of micro hotplate structures, inlet and outlet ports, and integrated mass-sensitive chemical sensors.

Each die is designed to accommodate an array of two or three µTPCs of varying sizes and four cantilever-based chemical sensors (Figure 2). The chemical sensors are placed at the inlet and outlet ports of the die to allow for monitoring of both upstream and downstream concentration levels when operated in a traditional gas-flow configuration. The system also has the capability of operating in a static atmosphere setup, where no

external flow system is required. Two of the four sensors can remain uncoated as reference devices in a differential setup to allow for the possibility of removing temperature effects in real-time during measurement.

The mass-sensitive micro-sensors, based on hammerhead-type resonator structures, which have been studied extensively at Georgia Tech [12, 74, 75, 92-94], have a mass resolution in the pico-gram regime, and are fabricated within the same process sequence as the μTPC arrays. The direct, on-chip integration of cantilever-based chemical sensors into the same chamber as the μTPC devices represents a novelty and has distinct advantages over systems which separate the two. For example, this arrangement results in a reduced total dead volume for the system as a whole (by reducing e.g. interconnect volume for valves and tubing between sensors and μTPCs), and reduced measurement cycle times. As discussed previously, the integrated sensors can monitor in real-time the loading state of the μTPC and also enable novel modes of operation which can allow the system to be operated in a static atmosphere, without the need for an external fluidic system. The cantilever-based sensors are well-understood and feature novel integrated heating units, which allow for the on-chip generation of thermal transients via temperature modulation of the heating units [95]. The use of signal transients has been demonstrated to improve analyte discrimination and the generation of signal transients via thermal modulation can be performed in a static, non-flowing atmosphere which allows the system to maintain its capability of operating without an external fluidic system [74, 89, 95]. Ultimately, this novel form of operation can add significant value to applications where the cost and complexity of integrating and operating an external flow system are prohibitive or restrictive to the application, such as placement on an airborne mobile drone or long-term environmental monitoring in remote locations [43, 59, 96-100].

Thermal Design

Prior to the development of a suitable fabrication process flow that would be compatible at the wafer-level with the existing cantilever-based microsensors, the μTPC devices were designed at a high level with a focus on making appropriate compromises among the several conflicting variables (e.g. pressure drop vs. breakthrough volume, thermal rise time vs. maximum temperature elevation vs. power consumption). The first design constraint examined was the target temperature elevation and thermal rise time during thermal desorption. External pre-existing system specifications required the design to achieve a maximum temperature elevation of 200˚C in less than 1 second, with minimal power consumption. For example, data from Supelco sorbents show typical desorption temperatures greater than 200 °C for commonly-used VOCs [101]. From the theory of heat transfer, it can be shown that the temperature elevation for a given power dissipation in a system dominated by heat conduction is given by

$$\Delta T = Q \cdot R_{thermal}$$

Equation 2 – Temperature elevation as a function of heating power.

where ΔT is the temperature elevation, Q is the instantaneous power dissipation, and $R_{thermal}$ is the effective resistance to heat conduction given by

$$R_{thermal} = \frac{L}{k \cdot A}$$

Equation 3 – Thermal resistance.

where A, the cross-section, and L, the length over which the heat conduction occurs, are determined by the geometry of the system and k is the thermal conductance of the material. The thermal time constant, $\tau_{thermal}$, is given by

$$\tau_{thermal} = R_{thermal} \cdot \rho \cdot c_p \cdot V$$

Equation 4 – Thermal time constant.

where $\tau_{thermal}$ is the thermal time constant, $R_{thermal}$ is the equivalent thermal resistance of the system, ρ is the material density, C_p is the specific heat, and V is the volume. It should be noted that these equations assume that the system can be described by lumped elements, with a uniformly heated volume V that is connected through a (massless) thermal resistance $R_{thermal}$ to a heat sink. From these equations it becomes clear that a theoretical maximum temperature elevation can be achieved by maximizing $R_{thermal}$ and minimizing k, while the thermal time constant is minimized by reducing $R_{thermal}$ and the thermal mass. To satisfy both conditions, however, a compromise must be made with regards to $R_{thermal}$. Additionally, for real devices there are practical, physical limits to the lower bounds of A and the upper bounds of L, and one is further constrained by k values offered from available materials (e.g. silicon, SiO_2). In addition to the external design specifications of achieving a maximum temperature elevation of 200˚C in less than 1 second, the choice to integrate cantilever-based sensors on-chip with the μTPC requires that the silicon membrane thickness falls between 5-25 μm. Since both the sensors and the μTPC membranes will be fabricated together on the same SOI substrate and with the same process sequence, their suspended thicknesses will be identical. Previous work with the cantilever-based sensors has shown that ideal thicknesses for resonance fall between 5-25 μm, thus constraining the thickness of the μTPC membranes to this range. As a result of these constraints, initial designs focused on exploring via finite element simulation the practical membrane geometries that are physically realizable with current MEMS/IC fabrication techniques at Georgia Tech, while still optimizing for temperature elevation and thermal rise time.

For the various device geometries presented, static thermal analyses were undertaken to find the temperature elevation (and temperature uniformity across the membrane) for a given heating power, while transient thermal analyses were employed to extract thermal time constants. Additionally, mechanical analyses were used to find the resonance frequency and the membrane deformation under gravity (with sorbent mass included). Finally, fluidic analysis of the μTPC arrays, with simulated flow through inlet and outlet

ports, were performed to optimize the fluid flow through the ridge and pillar structures (and, hence, the pressure drop across the μTPC module for a given sample flow). Especially in the case of the fluidic simulations, it was necessary to simplify the model geometry considerably due to limitations of available computing resources. Nonetheless, the results gave important guidelines for the spacing of the ridge and pillar structures: too narrow a spacing resulted in the sample flow bypassing the ridge structures, while too wide a spacing had a negative effect on the effective surface area available for sorbent deposition. Thus, the fluidic simulations aided in the optimization of ridge and pillar arrangements, resulting in reduced impedance for sample flow through the device.

Suspended Membrane without Pillars or Ridges

Operating under the initial assumption that a design for a simple 4 mm x 4 mm x 8μm silicon membrane suspended by four 2 mm x 200 μm x 8 μm legs could be successfully manufactured in the cleanroom facilities at Georgia Tech, this geometry was simulated via finite element analysis (FEA) software (COMSOL, Multiphysics). The theory discussed above predicts that such a membrane would have a total thermal resistance dominated by the geometry and material properties of the long, thin support legs. Since the four support legs offer equal and parallel thermal conduction paths, an effective thermal resistance of 1917 [K/W] can be calculated for this structure, resulting in a predicted thermal rise time of 0.44 sec and a maximum temperature elevation of 192˚C for 100 mW of dissipated power. It should be noted that these numbers assume heat transfer by conduction through the membrane material only and as discussed later, other heat transfer paths (conduction through surrounding air, convection and radiation) need to be considered for more accurate results. Simulation resulted in a thermal rise time of 0.5 sec and a maximum temperature elevation of 226˚C for 100 mW of dissipated power, which agrees with the simplified theoretical model to within 12-1

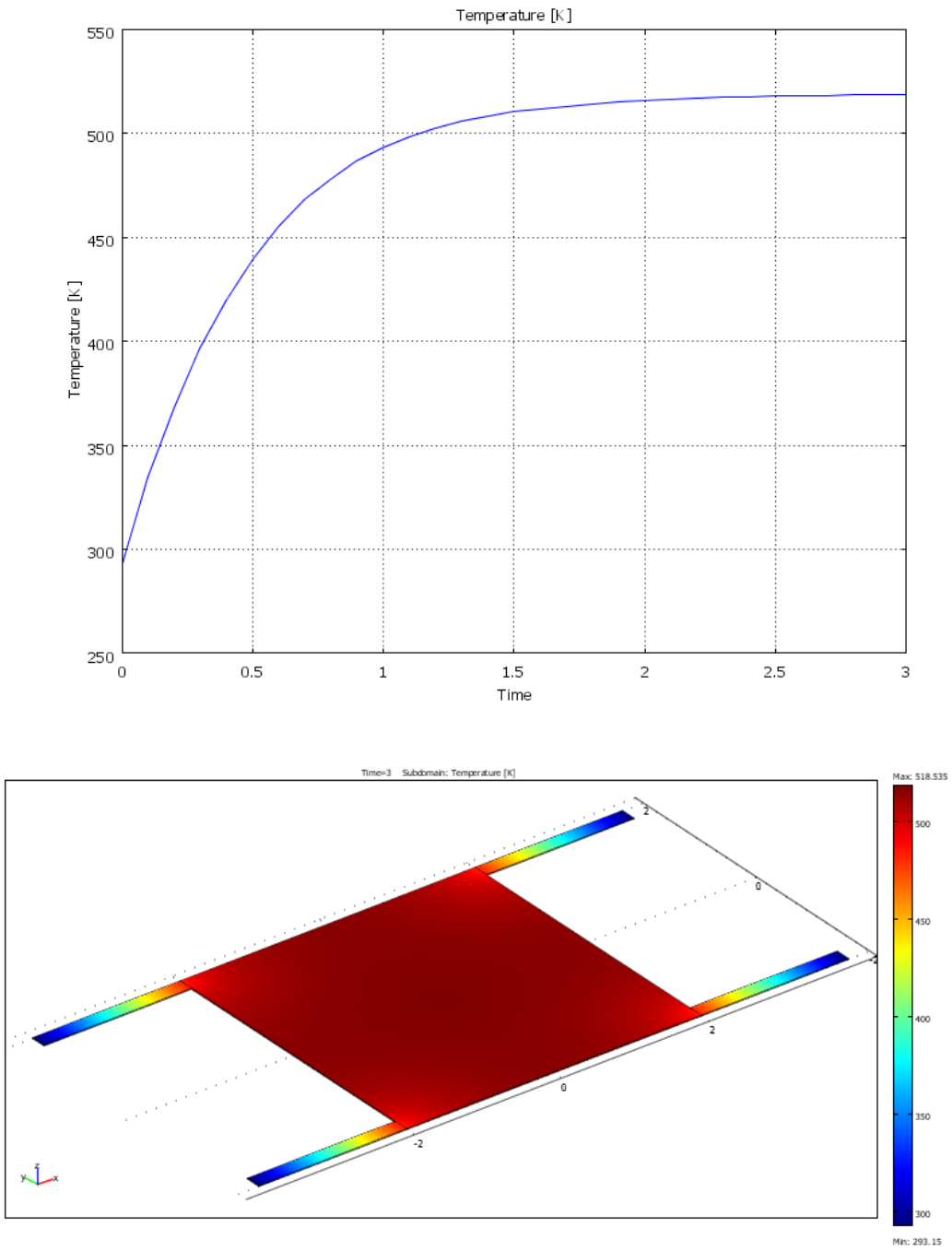

Figure 3 - FEA simulation results for 4 mm x 4 mm x 8 µm silicon membrane suspended by 2 mm x 200 µm x 8 µm legs, exhibiting an effective thermal resistance of 1917 [K/W]. The thermal properties of this device result in a predicted thermal rise time of 0.5 sec (top) and a maximum temperature elevation of 226˚C for 100 mW of dissipated power (bottom). The temperature distribution across the membrane appears very uniform, and the long, thin support legs provide excellent thermal isolation.

As a result of the support legs dominating the thermal resistance of the system, the largest temperature gradient appears across the length of the legs, between the room-

temperature substrate and the actively-heated membrane (Figure 3). As can be observed from the simulation results, the membrane itself exhibits a relatively uniform temperature distribution and reaches a temperature elevation similar to the result predicted by theory. A uniform heating distribution in the membrane is desirable so that thermal desorption of the sorbed VOCs occurs at the same temperature for all regions on the membrane.

Repeating the process for a device with the same membrane area (4 mm x 4 mm) but with 4 mm long support legs and a slightly thicker membrane of 20 μm (as opposed to 8 μm) results in a simulated thermal rise time of 1.5 sec and a maximum temperature elevation of 161˚C for 100 mW of dissipated power. In this case, fabrication of the thicker membrane requires correspondingly thicker support legs, as both features would be formed and released from the same SOI substrate, which results in a slightly reduced thermal resistance of 1533 [K/W] even though the length of the support legs has been doubled to 4 mm.

In both examples described above, the total effective surface area of each device is 32 mm^2 (membrane front and back side), yielding nearly identical sorption and concentration capacity from a chemical standpoint. In terms of thermal performance, however, it is apparent that the 8 μm thick membrane can achieve higher temperature elevation for a given heating power (due to increased thermal resistance in the legs), and can reach this temperature more quickly than the 20 μm thick device (due to reduced thermal mass). The thinner membrane would also result in a reduced dead volume following final packaging, due to the reduced footprint of the shorter support legs, which would in turn increase the overall pre-concentration factor. When considering system performance as a whole, it becomes clear that for similar chemical performance due to effective surface area for sorbent coating, a thinner membrane is desirable due to its improved thermal properties and footprint. Thus, a thinner membrane can achieve thermal desorption of sorbed analytes more quickly, at a higher temperature, and with lower power

dissipation. This results in a sharper desorption peak which is both narrower in time and higher in total peak concentration, yielding an increased pre-concentration effect.

Suspended Membranes with Ridges and Pillars

The effect of increasing the surface area of the device by adding high-aspect ratio ridges to the membrane area was also examined via FEA simulation of a smaller-area 2 mm x 2 mm x 8 µm membrane with 2 mm x 200 µm x 8 µm thick legs (Figure 4). The thermal mass equivalent of 100 ridges, each having dimensions of 200 µm x 10 µm x 2 mm, was modeled in a simplified way (i.e. without accounting for convection due to increased surface area) by simulating a single block membrane with an increased thickness of 108 µm (due to the added volume and mass of the arrayed ridges). The decision to move to a smaller membrane area was made based on external system constraints that limit practical die size to 9 mm x 9 mm, which will be discussed further in Chapter 3. Simply stated, there is not enough space within such a die to accommodate an array of even two 4 mm x 4 mm devices, when the necessary wire traces and packaging tolerances are accounted for. Thus, this simulation featured a smaller membrane area and resulted in a thermal rise time of 2 sec and a maximum temperature elevation of 194˚C for 100 mW of dissipated power (Figure 4). In this case the transient thermal properties of the design are less desirable, but the effective surface area of the device has nearly tripled to 88 mm^2 while the membrane footprint has been simultaneously reduced to one quarter of its original size. The reduction in footprint also reduces the dead volume in final packaging and allows for an arrayed approach (i.e. enabling the option of coarse pre-filtering). The results of these simulations are summarized in Table 1.

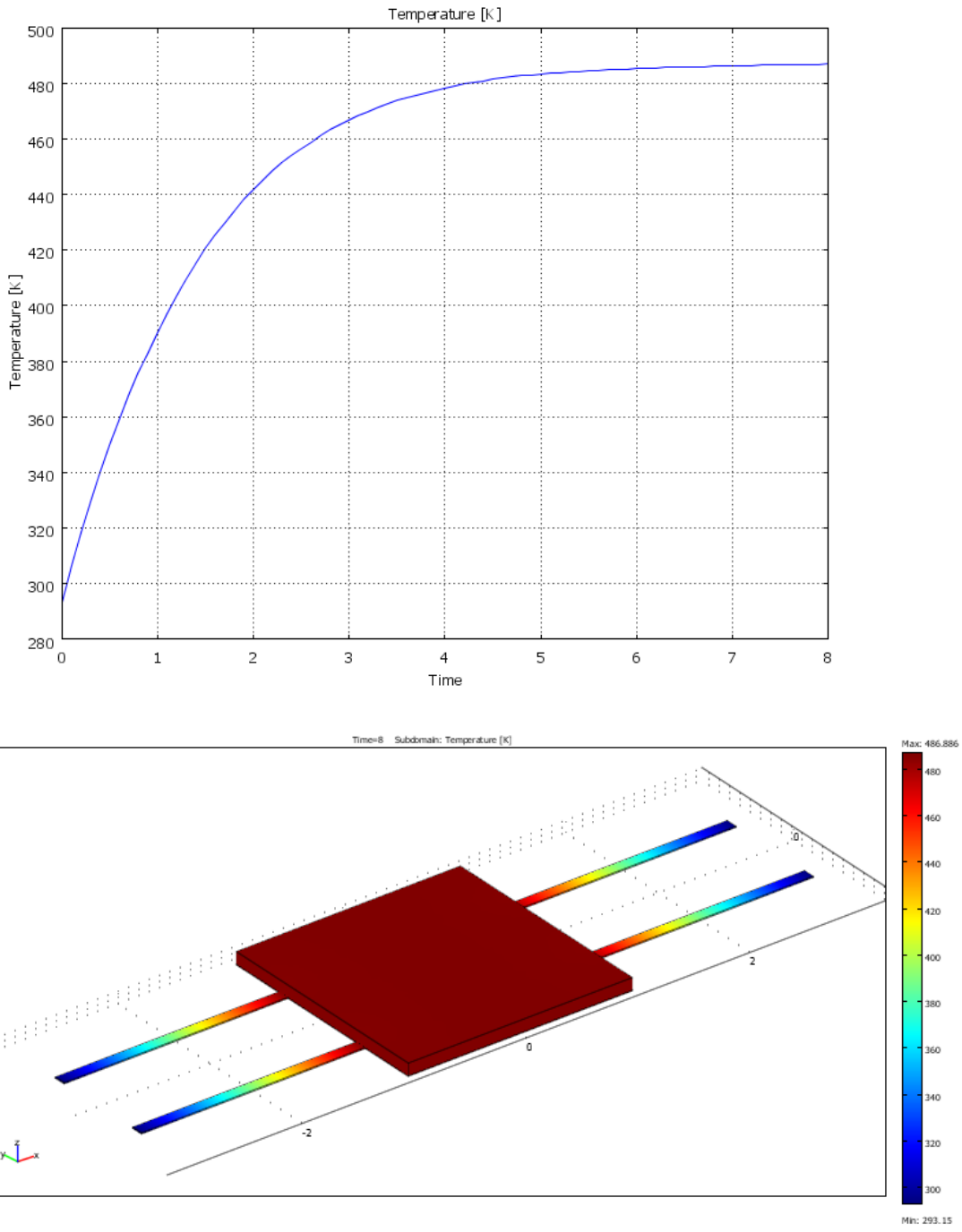

Figure 4 - FEA simulation results for 2 mm x 2 mm x 8 µm silicon membrane with added mass representing 100 high-aspect ratio ridges with dimensions of 200 µm x 10 µm x 2 mm each. The structure is suspended by 2 mm x 200 µm x 8 µm legs, exhibiting an effective thermal resistance of 1917 [K/W]. The thermal properties of this device result in a thermal rise time of 2 sec (top) and a maximum temperature elevation of 194˚C for 100 mW of dissipated power (bottom).

Table 1 – Summary of simulation results for simplified membrane geometries.

Device dimensions	4 mm x 4 mm x 8 µm membrane 2 mm x 200 µm x 8 µm legs (no ridges)	4 mm x 4 mm x 20 µm membrane 4 mm x 200 µm x 20 µm legs (no ridges)	2 mm x 2 mm x 8 µm membrane 2 mm x 200 µm x 8 µm legs (100 ridges, 200 µm x 10 µm x 2 mm each)
Effective surface area [mm^2]	32	32	88
Max. temperature elevation [K]	226	161	194
$\tau_{thermal}$ [sec]	0.5	1.5	2.0
$P_{applied}$ [mW]	100	100	100

The footprint – and corresponding dead volume – of these designs can be further reduced without sacrificing thermal isolation due to leg length, L, by simply moving the support anchors for the legs to the side of the membrane and bending the legs around the membrane perimeter, as depicted in Figure 5. This geometry has the additional advantage of improving leg compliance and flexibility through the addition of the bent angles, thereby improving device yield during manufacturing. This design also retains the ability to array several devices side-by-side on the die without a significant increase to total footprint.

Final Design

With this new insight, several geometries were designed using the simplified theory discussed previously as an initial guide and FEA simulation as a confirmation of expected

performance. The finite element simulations described below not only include heat transfer by conduction through the silicon, but also heat transfer through the air by conduction. Initially, the air around the membrane was simulated using a thermal conductivity of 0.026 W/mK. The resulting models are computationally demanding and, thus, in subsequent models heat transfer through the air was simulated using a heat transfer coefficient of h = 50 [$W/m^2 \cdot K$] applied to the surfaces is the membrane. This heat transfer coefficient corresponds to a conduction over 500 µm of air.

The first of these designs features a 1 mm x 1 mm x 20 µm membrane supported by four bent legs with total lengths of 1.3 mm each and cross-sections of 100 µm x 20 µm (Figure 5). The effective thermal resistance of the four parallel support legs was calculated to be 997 K/W. For a simulated input power of 500 mW, $\tau_{thermal}$ was found to be 0.2 sec with a temperature elevation of 265 K. This design also features six high-aspect ratio ridges on the membrane, each having dimensions of 1 mm x 500 µm x 50 µm, yielding a total surface area of 7 mm^2 per device and a total surface area of 21 mm^2 for an array of three devices. The mechanical properties of the design were also simulated *via* FEA, yielding a simulated fundamental resonance frequency of 5948.8 Hz and a deflection of 105 nm for an estimated additional sorbent mass of 5 mg. Finally, the fluidic properties of the design were simulated, revealing a relatively low estimated pressure drop of 35.6 Pa across an array of three devices.

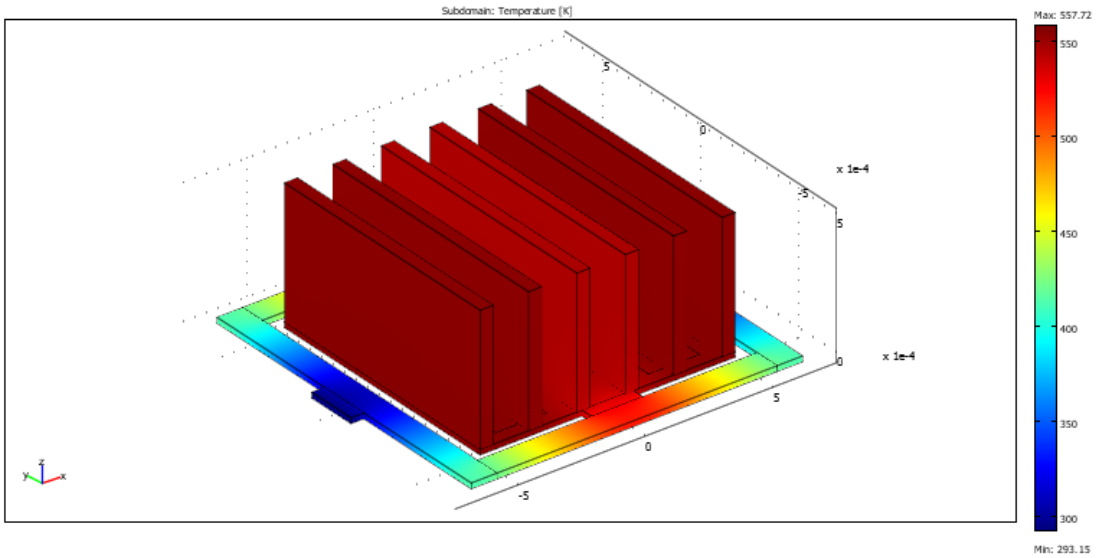

Figure 5 - Thermal simulation of a 1 mm x 1 mm x 20 µm membrane with sorbent ridges included.

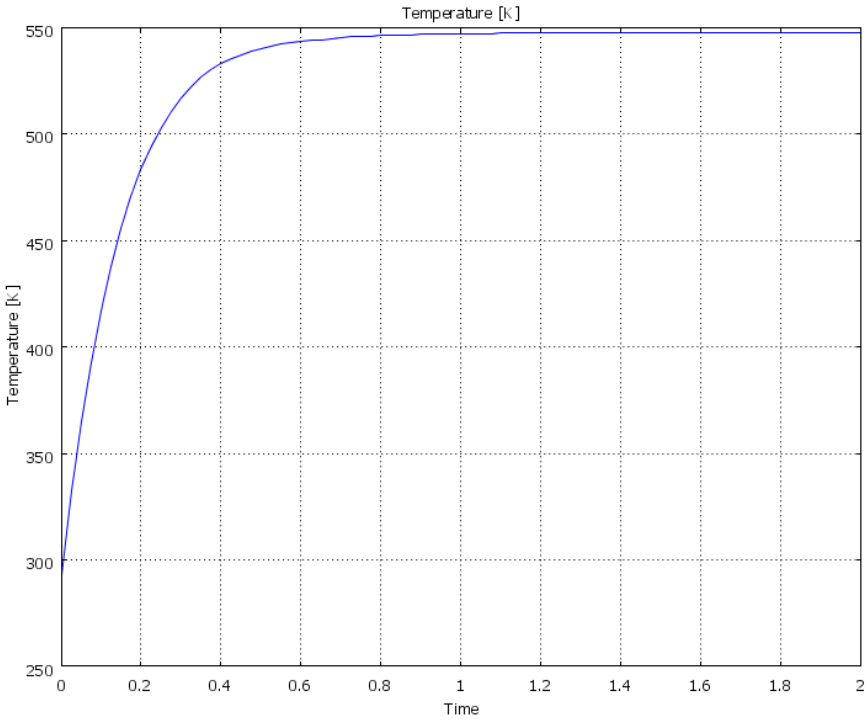

Figure 6 - Thermal simulation of transient response of a 1 mm x 1 mm x 20 µm membrane with sorbent ridges included.

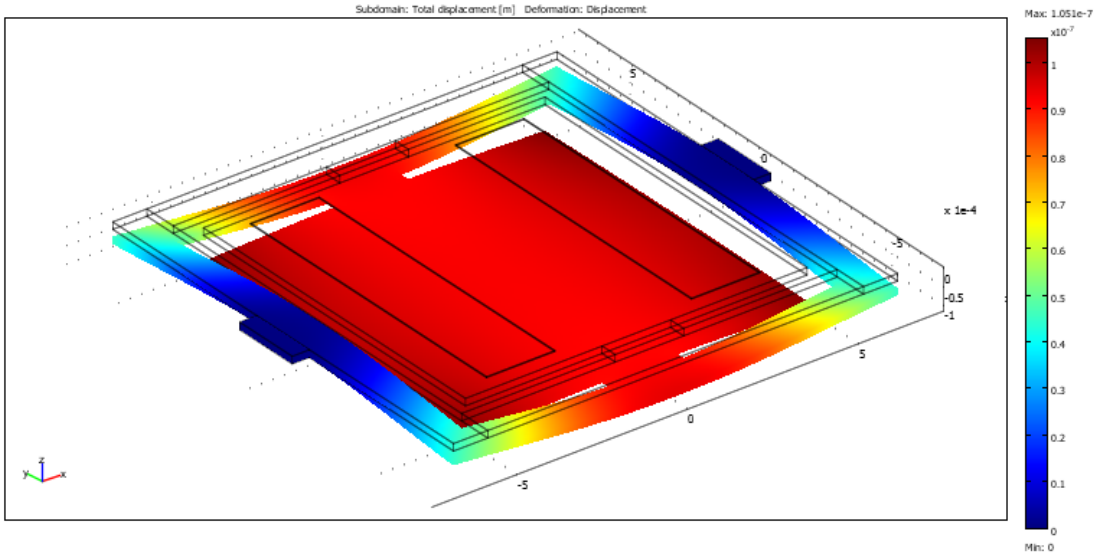

Figure 7 - Gravitational deflection of 1 mm x 1 mm x 20 µm membrane with ridges and additional 5 mg of sorbent mass included (ridges not pictured).

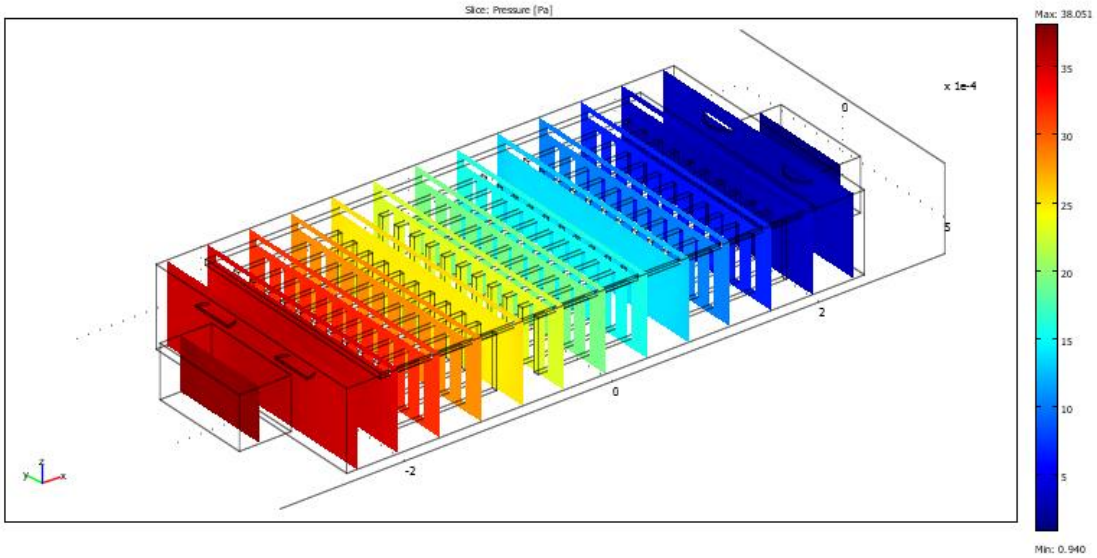

Figure 8 - Pressure drop across an array of three 1 mm x 1 mm x 20 µm membranes with sorbent ridges included.

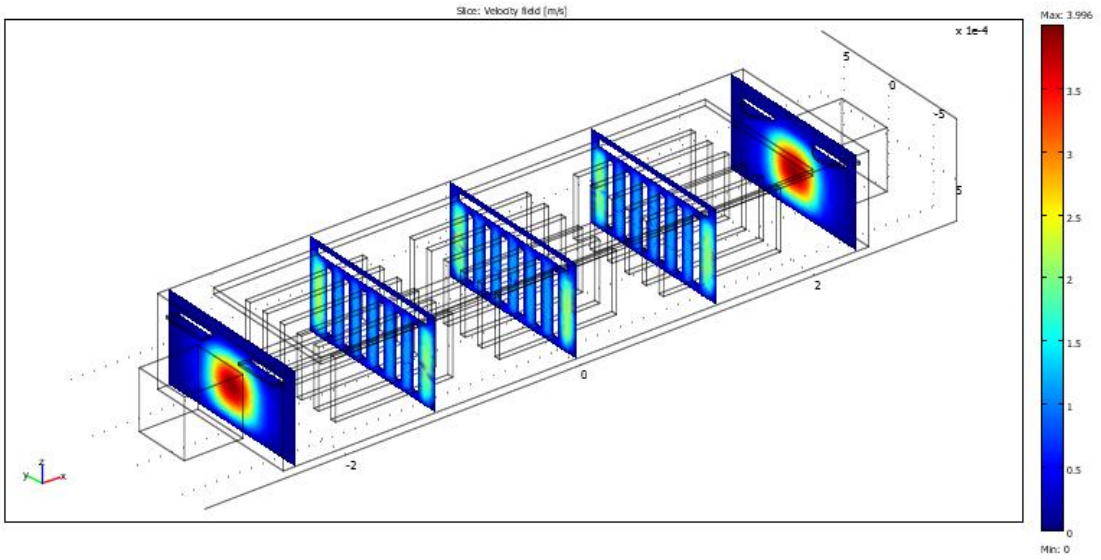

Figure 9 - Fluid flow through an array of three 1 mm x 1 mm x 20 µm membranes with sorbent ridges included.

The second design features a larger 2 mm x 1 mm x 20 µm membrane supported by four bent legs with total lengths of 1.8 mm each and cross-sections of 100 µm x 20 µm (Figure 10). The effective thermal resistance of the four parallel support legs was calculated to be 1380 K/W. For a simulated input power of 500 mW, $\tau_{thermal}$ was found to be 0.4 sec with a temperature elevation of 229 K. This design also features eleven high-aspect ratio ridges on the membrane, each having dimensions of 1 mm x 500 µm x 50 µm, yielding a total surface area of 13 mm^2 per device and a total surface area of 39 mm^2 for an array of three devices. The mechanical properties of the design were simulated *via* FEA, yielding a simulated fundamental resonance frequency of 2333.8 Hz and a deflection of 443 nm for an estimated additional sorbent mass of 5 mg. Finally, the fluidic properties of the design were simulated, revealing a relatively low estimated pressure drop of 40.7 Pa across an array of three devices.

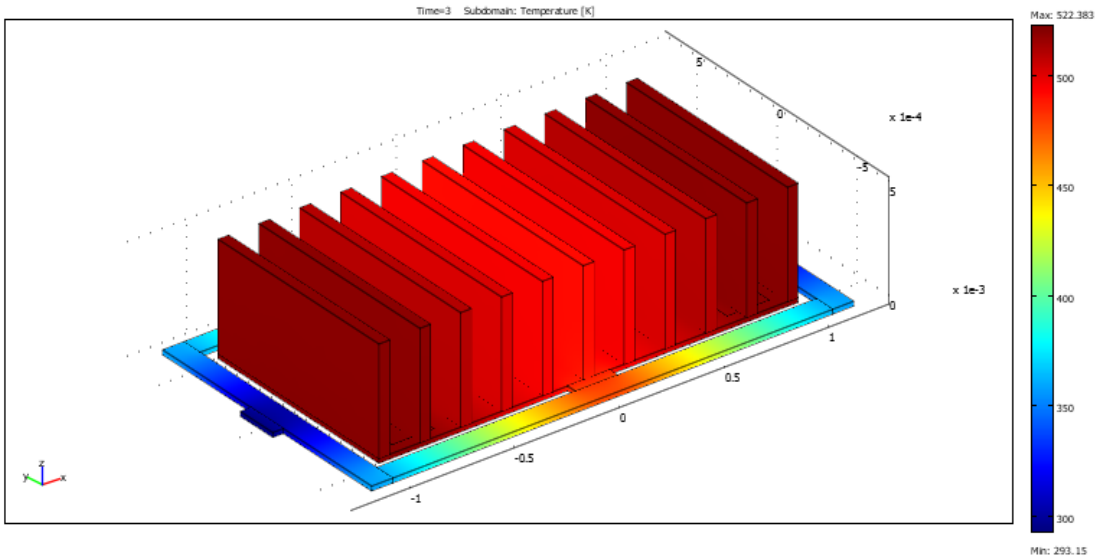

Figure 10 - Thermal simulation of a 2 mm x 1 mm x 20 µm membrane with sorbent ridges included.

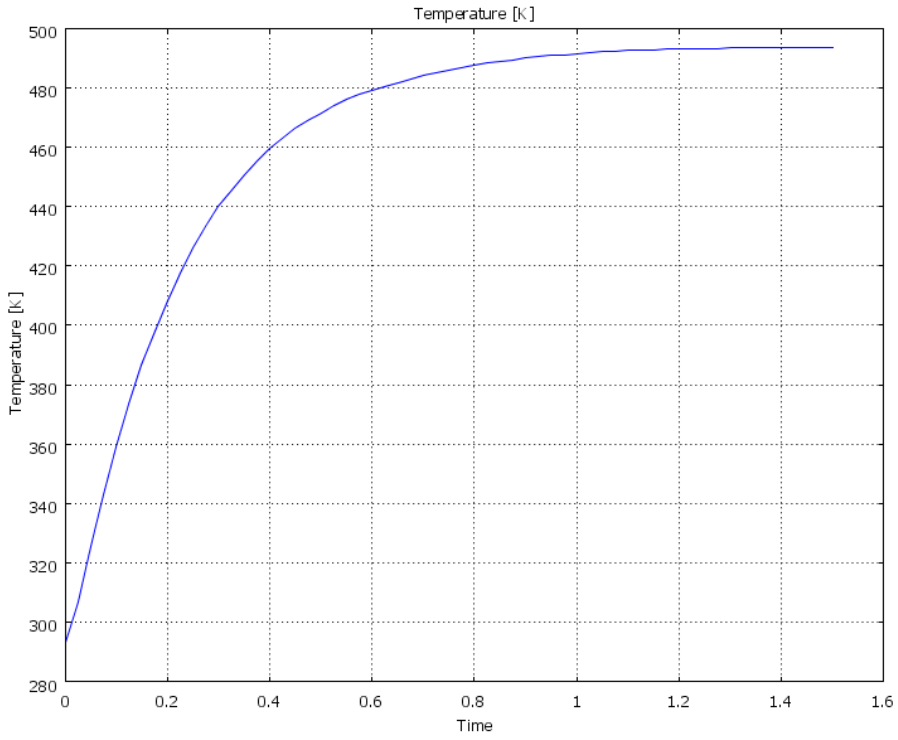

Figure 11 - Thermal simulation of transient response of a 2 mm x 1 mm x 20 µm membrane with sorbent ridges included.

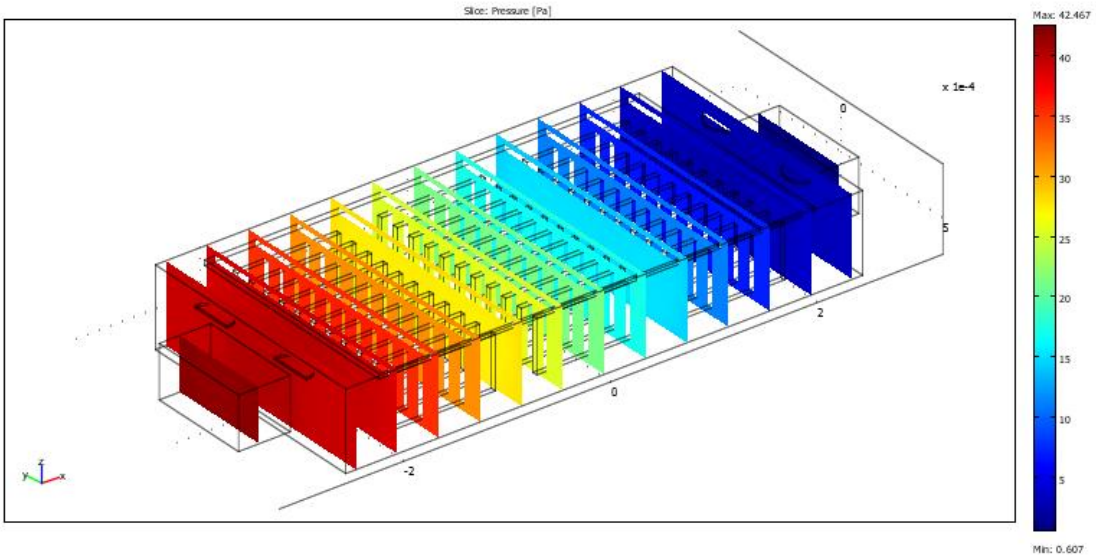

Figure 12 - Pressure drop across an array of three 2 mm x 1 mm x 20 µm membranes with sorbent ridges included.

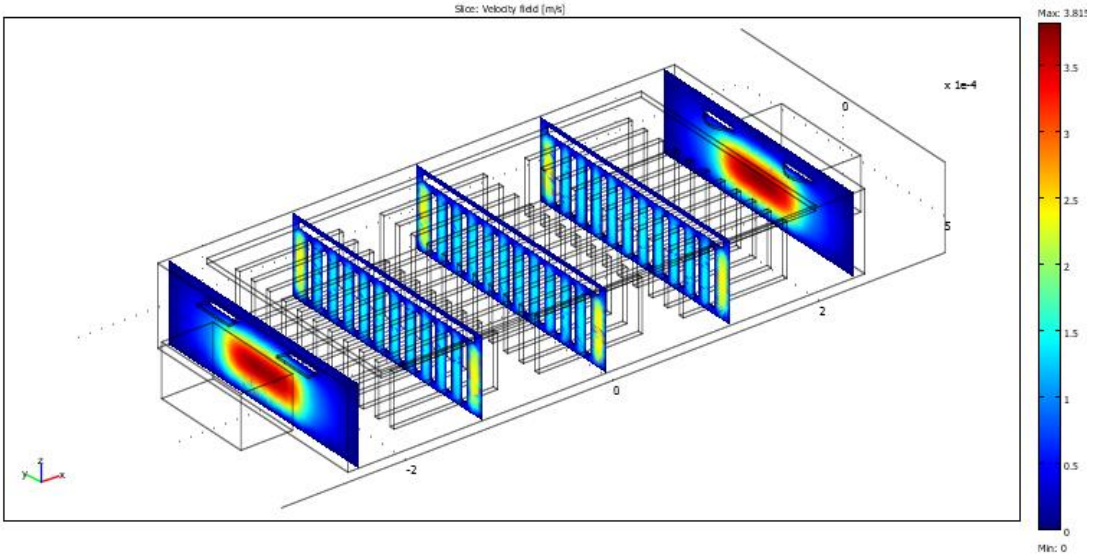

Figure 13 - Fluid flow through an array of three 2 mm x 1 mm x 20 µm membranes with sorbent ridges included.

The third and final design features an even larger 2 mm x 2 mm x 20 µm membrane supported by four bent legs with total lengths of 2.3 mm each and cross-sections of 100 µm x 20 µm (Figure 14). The effective thermal resistance of the four parallel support legs was calculated to be 1763 K/W. For a simulated input power of 1 W, $\tau_{thermal}$ was found to

be 0.6 sec with a temperature elevation of 271 K. This design also features eleven high-aspect ratio ridges on the membrane, each having dimensions of 2 mm x 500 µm x 50 µm, yielding a total surface area of 26 mm^2 per device and a total surface area of 52 mm^2 for an array of two devices. The mechanical properties of the design were simulated *via* FEA, yielding a simulated fundamental resonance frequency of 1333.8 Hz and a deflection of 821 nm for an estimated additional sorbent mass of 5 mg. Finally, the fluidic properties of the design were simulated, revealing a relatively low estimated pressure drop of 52.0 Pa across an array of two devices.

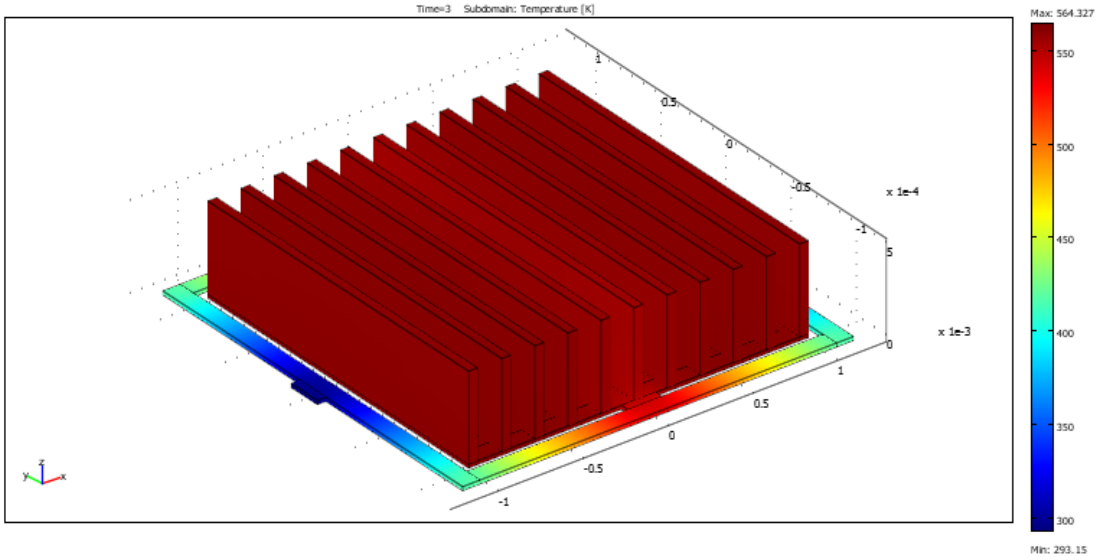

Figure 14 - Thermal simulation of a 2 mm x 2 mm x 20 µm membrane with sorbent ridges included.

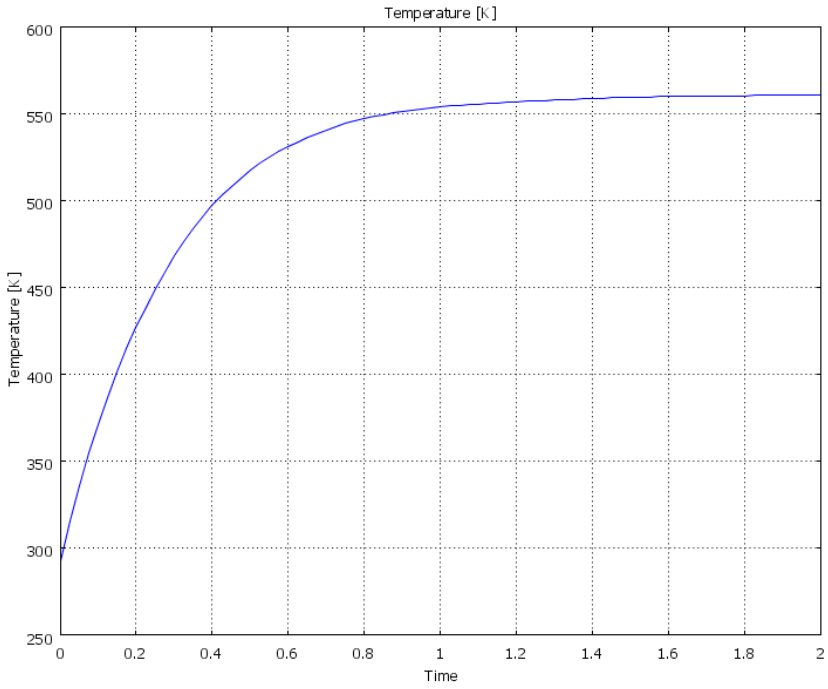

Figure 15 - Thermal simulation of transient response of a 2 mm x 2 mm x 20 µm membrane with sorbent ridges included.

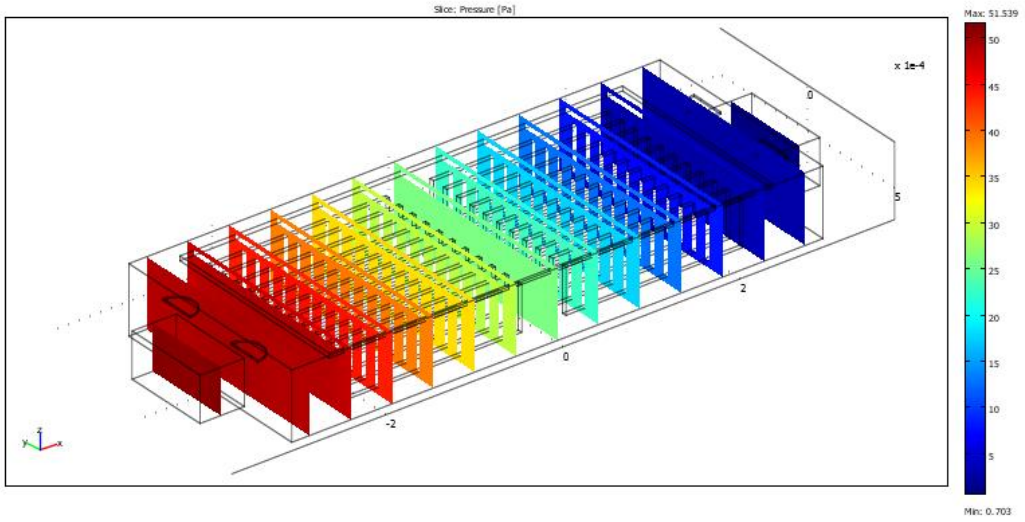

Figure 16 - Pressure drop across an array of two 2 mm x 2 mm x 20 µm membranes with sorbent ridges included.

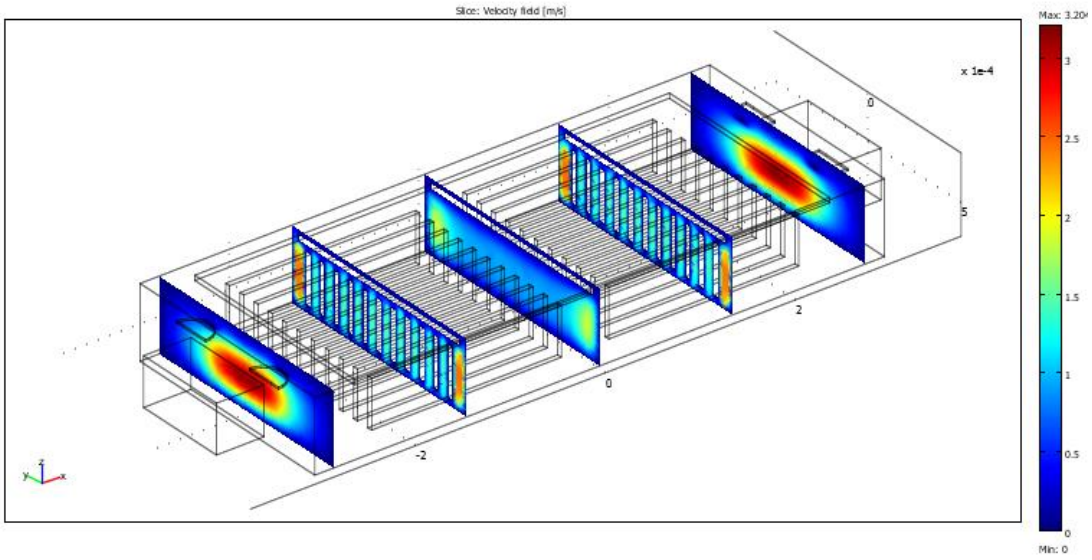

Figure 17 - Fluid flow through an array of two 2 mm x 2 mm x 20 µm membranes with sorbent ridges included.

The simulation results for these three designs are summarized in Table 2. In all three designs, the simulated fundamental resonance frequencies were designed to be orders of magnitude smaller than the resonance frequencies of the integrated resonant cantilever-based sensors. This difference in resonance frequencies is important, in order to minimize mechanical coupling and interference between the sensors and µTPCs during operation. The simulations also show that all three designs exhibit relatively uniform heating across the central membrane surfaces, and possess excellent thermal isolation enabling optimal temperature elevation for thermal desorption from the proposed sorbent coatings with minimal power dissipation. Additionally, the mechanical deflection due to gravitational forces acting on the µTPC devices (including added sorbent mass) was found in all three designs to be negligible, indicating a low probability of mechanical failure during normal operation. Finally, Table 2 shows that these three designs meet the required thermal specifications discussed previously, with minimal on-chip footprint. The designs also cover a wide range of the target design space to allow for extensive "real-world" testing of the

effects of the various parameters (e.g. surface area vs. $\tau_{thermal}$) in anticipation of future designs based on knowledge gained from this work. Additionally, several other designs were simulated and evaluated which featured wide ranges of ridge and pillar densities, but the results of these are not included here for the sake of brevity.

Table 2 – Summary of simulation results for final designs, featuring bent-leg geometries and incorporating high aspect-ratio features on the suspended membranes.

	1 mm x 1 mm x 20 µm	2 mm x 1 mm x 20 µm	2 mm x 2 mm x 20 µm
Surface area per device [mm^2]	7	13	26
Surface area per die [mm^2]	21	39	52
Fundamental resonant mode [Hz]	5948.8	2333.8	1333.8
Gravitational deflection with 5 mg of added sorbent [nm]	105	443	821
Pressure drop across array [Pa]	35.6	40.7	52.0
Input power [mW]	500	500	1000
Maximum temperature elevation [K]	265	229	271
$\tau_{thermal}$ [sec]	0.2	0.4	0.6

CHAPTER 3 – MASK LAYOUT & PROCESS DEVELOPMENT

Upon verification of viable thermal and mechanical designs, a compatible fabrication process flow for integration of the proposed µTPC designs with existing cantilever-based sensor technology was developed, and corresponding photomasks were designed and manufactured (DeltaMask, Netherlands) using CAD layout software.

This deeper level of the development process saw the introduction of additional design constraints imposed both by fabrication limitations and also by the necessity of interfacing the completed devices with pre-existing, external circuitry required for performing chemical measurements and experiments. For example, the circuit board used to excite and track the resonance frequency shifts of the resonant chemical sensors was previously designed to accommodate a 28-pin ceramic DIL package. As a result of the package dimensions, the maximum practical die size for the µTPCs was limited to 9 mm x 9 mm. Thus, the mask layout design is constrained to have die sizes below these dimensions, while simultaneously accommodating arrays of large-area membrane-based µTPCs and also the large-area inlet and outlet ports necessary for introducing analyte gas concentrations into the measurement chamber.

Additionally, each die must have space to place four on-chip cantilever-based chemical sensors, with the many wire traces necessary to carry the signals that excite the sensors into resonance and perform chemical measurements. These wire traces must also terminate in bond pads of sufficient size near the edge of the die to allow for all 28 wirebonds between the ceramic DIL package and die to make connections without overlap or interference. As discussed previously, while large-area 4 mm x 4 mm membranes can be fabricated with current MEMS/IC fabrication techniques, such were deemed unsuitable

for this particular design due to the requirement for an arrayed pre-concentration system and the external constraints placed on die size and footprint. As a result of these restrictions, several smaller-footprint membrane-based pre-concentrators were designed and placed in arrays of two or three devices each, yielding a relatively large total surface area for the system while simultaneously offering reduced thermal time constants (due to reduced thermal mass of the individual membranes) and enabling the possibility of coarse pre-filtering of complex gas mixtures.

In addition to restrictions imposed on individual membrane footprint, an example of a design constraint introduced when considering the possibility of device failure is the support leg dimensions. As discussed previously, the legs must be capable of supporting the weight of the suspended membrane – with added sorbent mass – during manufacture, final packaging, and normal operation following final packaging. Simulations were performed to verify that device failure during normal operation is unlikely, but it is more difficult to accurately assess forces experienced during the fabrication and packaging process (e.g. shear forces due to rinsing the wafer in DI water). Thus, an examination of similarly-dimensioned suspended structures fabricated previously in the IEN cleanroom facilities at Georgia Tech was conducted and confirmed a reasonable likelihood of successful fabrication with high yield for the final designs discussed in Chapter 2.

In addition to supporting the weight of the suspended membrane, the legs must also carry long, thin metal traces with the capability of delivering fairly significant amounts of power without failure (e.g. 12.5 GW/m^3 in the 2 mm x 2 mm x 20 μm membrane). Since this system is designed with the goal of mobile operation without the availability of high voltages, the power must be supplied primarily using a large current. Due to the thin

metallization layer required for processing the cantilever sensors, which are integrated into the same die and process sequence as the μTPCs, this requirement results in a situation where the metal traces along the legs must be made as wide as possible to facilitate the delivery of high current to the membrane with minimal power dissipation in the traces (i.e. low resistance) and minimal likelihood of device failure due to overheating and electromigration. With these considerations taken into account, and based on an examination of the current-carrying capacity of the metal traces for previously-developed devices, it was determined that a trace width of 50 μm would exhibit sufficient current-handling capacity for the designs. Since this proposed trace width (including the additional setback tolerances from the edge necessary in manufactured devices) is much less than the 100 μm width of the support legs in the previously-discussed thermal designs, no change in leg dimensions was necessary to accommodate the high-current metal traces. Figure 18 shows a detail from the final mask layout, illustrating the implementation of the support legs from the thermal design stage, overlaid with the proposed metal traces.

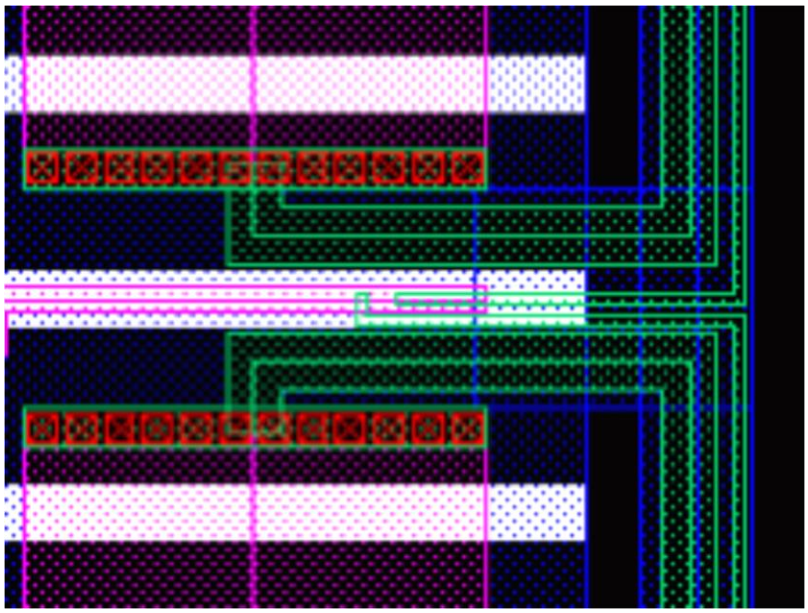

Figure 18 - Detail from final mask layout of current-carrying metal traces (green) on support legs and membrane (blue). The traces make contact to the diffused heaters (purple) by way of arrays of contact vias (red). The white bars show the placement of high aspect-ratio ridges on the back surface of the pre-concentrator membrane, and the black areas indicate the areas of the silicon handle wafer that are removed by a DRIE step from the back of the wafer.

Heater Design

With initial compatibility established between the thermal-mechanical designs and the proposed metallization and device placement on the die, development shifted to design of the integrated heating units. The heaters, which are formed as boron-doped diffused resistors in silicon, were designed to deliver efficient, localized power dissipation in the suspended membrane region *via* joule heating. Examination of the properties of the boron diffusion step in the cantilever sensor fabrication process revealed a sheet resistance of approximately 110 Ω/□. This measured sheet resistance value was achieved *via* boron diffusion from solid sources boron sources into a silicon substrate in a conventional tube furnace at 930 C for 40 min with a constant nitrogen flow throughout. Prior to performing the diffusion, the geometry of the resistors is defined by removal of the field oxide *via* dry

etching of SiO_2 with C_4F_8 in the regions to be doped. Following diffusion, drive-in was performed in a tube furnace. In addition to measuring the sheet resistance of completed devices, the diffusion and drive-in process was also simulated in software *via* SUPREM (Figure 19).

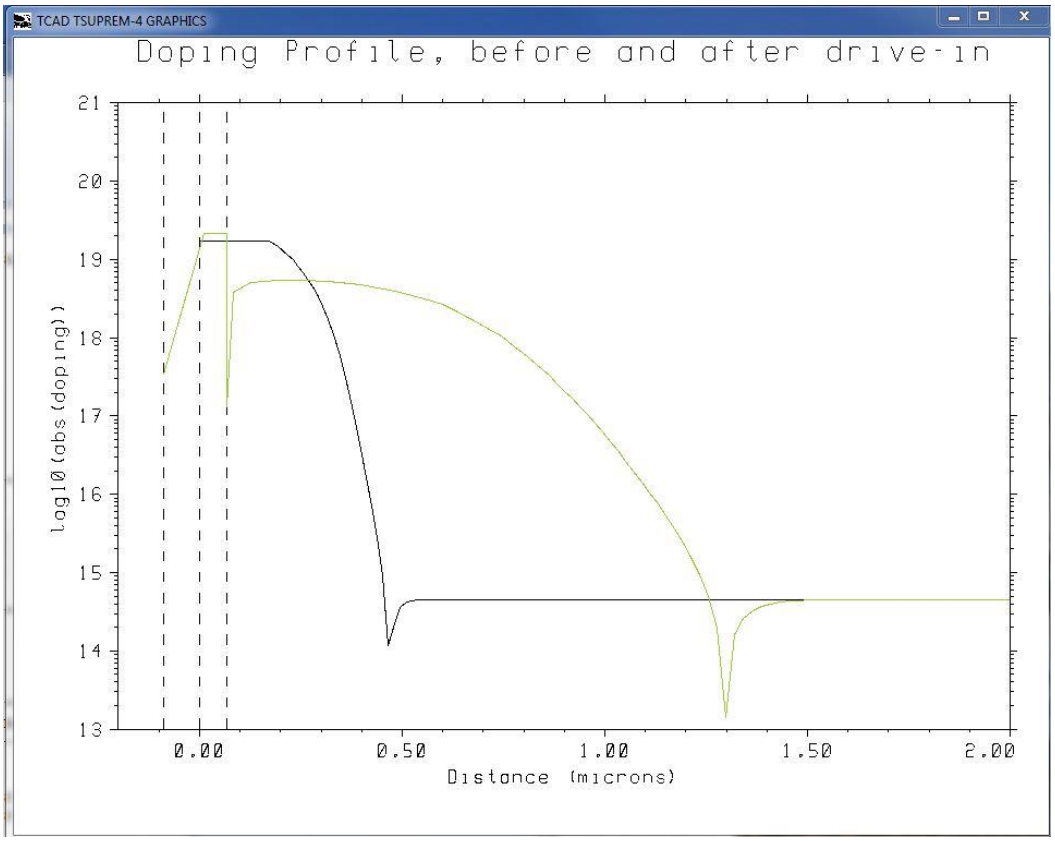

Figure 19 - Result of SUPREM simulation for boron diffusion and drive-in sequence, performed during manufacture of diffused heaters. Prior to drive-in, the simulated junction depth is approximately 0.45 µm; following drive-in, the junction has deepened to approximately 1.2 µm with a simulated sheet resistance of 248 Ω/□.

The code and file output for this simulation can be found in Appendix A. The simulation reveals that the initial diffusion results in a predicted junction depth of approximately 0.45 µm, with the drive-in moving the junction further into the silicon to approximately 1.2 µm. The simulated sheet resistance is 248 Ω/□.

With an estimated range of the expected sheet resistance for the diffused heaters, and a desire for mobile operation limiting heating voltages to less than 12 V, the integrated heaters were designed to have nominal resistances of approximately 500 Ω. The aspect ratio required to achieve this resistance for each heater was approximately 5:1. The measurement resistors were designed to have resistances in the mid-kΩ range. During mask layout, the heaters were placed along the membrane edges most distant from the anchor points of the support legs, and two heaters were placed on each membrane (Figure 20). This placement is the same as that used in the previously-discussed thermal simulations, ensuring optimal thermal isolation and temperature uniformity across the entire membrane region.

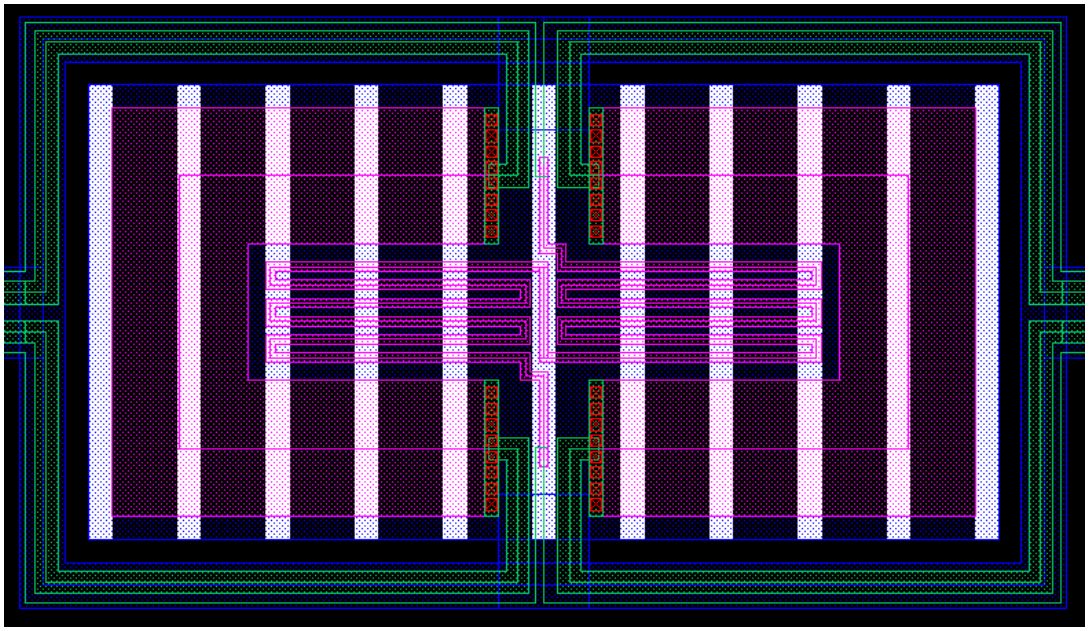

Figure 20 - Detail from final mask layout showing placement of two diffused heaters (purple) on suspended 2 mm x 1 mm pre-concentrator membrane (blue). Electrical traces (green) make contact to the heaters and measurement resistors by way of arrays of contact vias (red). The white bars show the placement of high aspect-ratio ridges on the back surface of the pre-concentrator membrane.

The two heating resistors have separate electrical traces, and can therefore be wired in series or in parallel during packaging, lending flexibility for the system to adjust its equivalent resistance to match differing external interface requirements. For example, if higher voltages are available at the circuit level, the heaters can be wired in series in order to reduce the number of wire-bonds and external pin connections. If, however, voltages above 12 V are not available, the heaters can be wired in parallel to reduce the heating voltage necessary to achieve the same heating power.

In addition to the two heating resistors, each membrane was also equipped with a long, thin measurement resistor in the center (Figure 20) designed to gauge the real-time temperature of the membrane during heating. The measurement resistor was designed to be capable of performing an accurate 4-wire measurement and a high aspect-ratio geometry was chosen to result in maximum absolute resistance change with respect to temperature, further enhancing resolution of the temperature measurement. This integrated resistive temperature sensor allows the μTPCs to be embedded in a simple feedback loop, so that an accurate desorption temperature can be maintained even under the presence of manufacturing variations. In addition, such a control loop allows for the implementation of more complex temperature profiles. An example of such a control loop is shown in Figure 21, where an operational amplifier controls the voltage applied across the heating resistor based on the voltage drop across the resistive temperature sensor. The cross-domain model for the resulting feedback system was implemented in Simulink using the experimental data from a fabricated 2 mm x 2 mm pre-concentrator. Figure 21 (b) shows how such a feedback signal can heat the membrane to approximately 150˚C in about 0.4 seconds and

then maintain a constant temperature. The presented feedback model is based on a single operational amplifier (and a current source to bias the resistive temperature sensor).

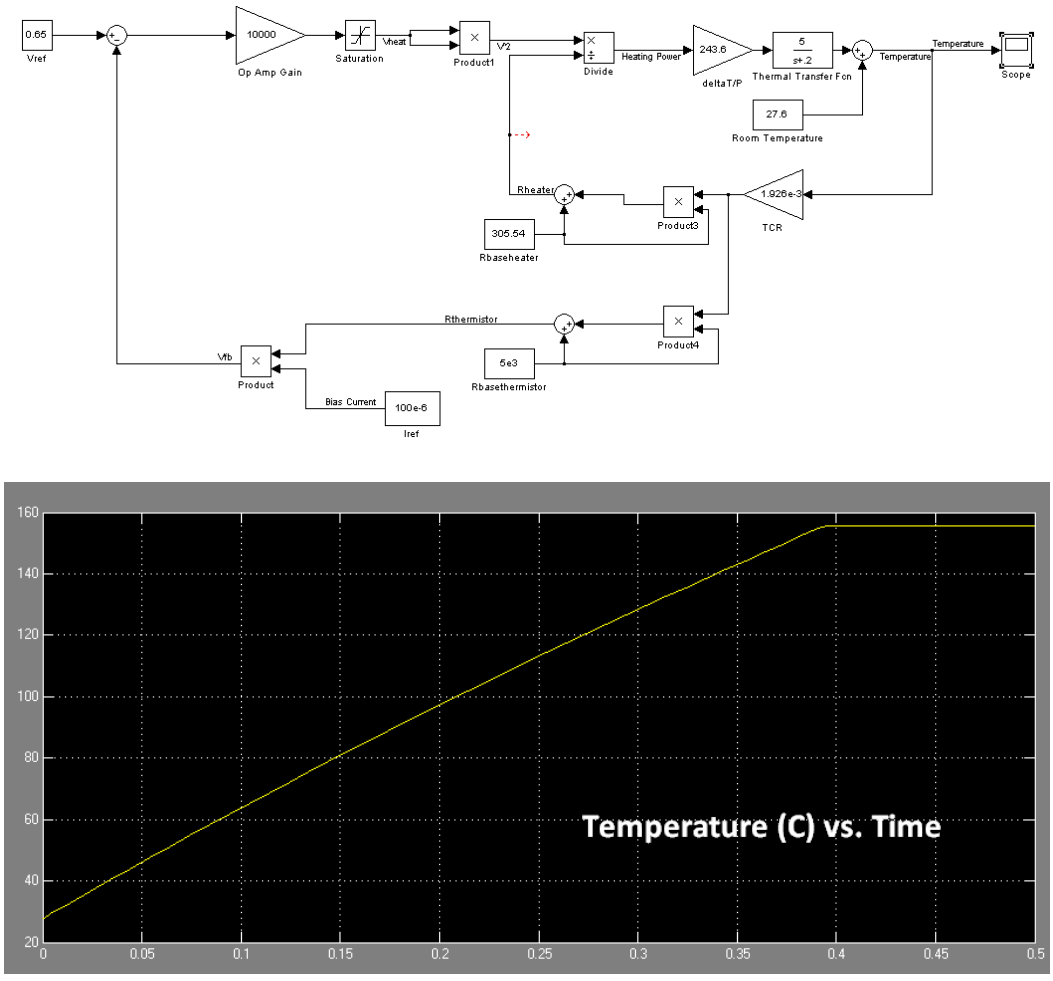

Figure 21 - Example of cross-domain SIMULINK model (top) of a feedback system controlling the micro hotplate temperature, and µTPC temperature (bottom) as a function of time demonstrating control of µTPC temperature (the model is based on experimental data obtained from the 2 mm x 2 mm pre-concentrators).

Ridge and Pillar Placement

In addition to integrated heaters, the final thermal-mechanical designs discussed in Chapter 2 incorporated arrays of high aspect-ratio ridges on the surface of the membrane

in order to increase the surface area available for sorbent coating, and in turn increase the sorption capacity of the μTPC. Ultimately, a higher sorption capacity leads to a higher pre-concentration factor, as the dead volume remains fixed while more analyte will be released during thermal desorption. This increased amount of released analyte into a fixed volume results in an increased concentration peak, enhancing the effective sensitivity of the integrated chemical sensors.

Various densities and arrangements of ridges and pillars, with varying total surface areas, were designed for placement on the die during mask layout. Clearly, increasing the density and aspect-ratio for the arrays of pillars and ridges correspondingly increases the effective surface area of the device without increasing die footprint. There are practical limitations, however, to both the aspect-ratio and the density for these features. First, manufacturing capabilities limit the aspect ratio for a ridge or pillar formed *via* DRIE of silicon to be less than approximately 50:1. Furthermore, while 50:1 aspect-ratio pillars and ridges may be successfully fabricated, such features must also be sufficiently rugged to withstand sorbent coating and final packaging. As it can be difficult to estimate the forces present during sorbent coating (e.g. wetting/drying forces of the solvent/polymer mixes, air pressure from airbrush spray gun) a conservative design was chosen to ensure increased device yield during deposition of the sorbent layers. Finally, the effects of ridge and pillar density on airflow through the enclosed chamber must be considered. As density increases, flow through the chamber will be increasingly, and undesirably, shunted around the sides of the membrane and over the support legs rather than through the high surface-area regions of the ridges and pillars. Such a situation increases the pressure drop of the system and limits interaction between the gas sample and the device, reducing effective surface area.

Thus, as discussed in Chapter 2, fluidic simulations of various ridge and pillar densities were performed to ensure adequate interaction between the flowing gas sample and the sorbent-coated high aspect-ratio features on the membranes. When the device is operated in a static non-flowing atmosphere, however, gas-sorbent interactions are driven primarily by diffusion and not by forced flow, thereby allowing for the possibility of extremely high density arrangements to function without the reduced capacity (due to flow shunting) experienced by the forced flow approach. A summary of the ridge and pillar placements included in the final mask layout are listed in Table 3. In all cases outlined in the table, widths of both 20 μm and 50 μm for both the pillars and ridges were used.

Table 3 - Summary of die specifications present in final mask layout.

Membrane Area	Pillar vs. Ridge	Spacing	Heated Sensors?	# of Chips per Wafer
1 mm x 1 mm	Pillar	140 µm	Yes	4
	Ridge	120 µm	Yes	2
	Pillar	120 µm	Yes	2
	Pillar	50 µm	Yes	2
	Pillar	29 µm	Yes	2
	Ridge	140 µm	No	6
	Ridge	120 µm	No	2
	Pillar	120 µm	No	2
	Pillar	50 µm	No	2
	Pillar	29 µm	No	2
2 mm x 1 mm	Ridge	145 µm	Yes	2
	Pillar	145 µm	Yes	2
	Pillar	70 µm	Yes	4
	Ridge	145 µm	No	10
	Pillar	145 µm	No	8
	Pillar	70 µm	No	4
2 mm x 2 mm	Ridge	145 µm	Yes	2
	Pillar	145 µm	Yes	2
	Pillar	70 µm	Yes	4
	Ridge	145 µm	No	10
	Pillar	145 µm	No	10
	Pillar	70 µm	No	4

Figures 22-24 show several details from the final mask layout, demonstrating examples of die with either pillars or ridges placed on the arrays of suspended pre-concentrator membranes.

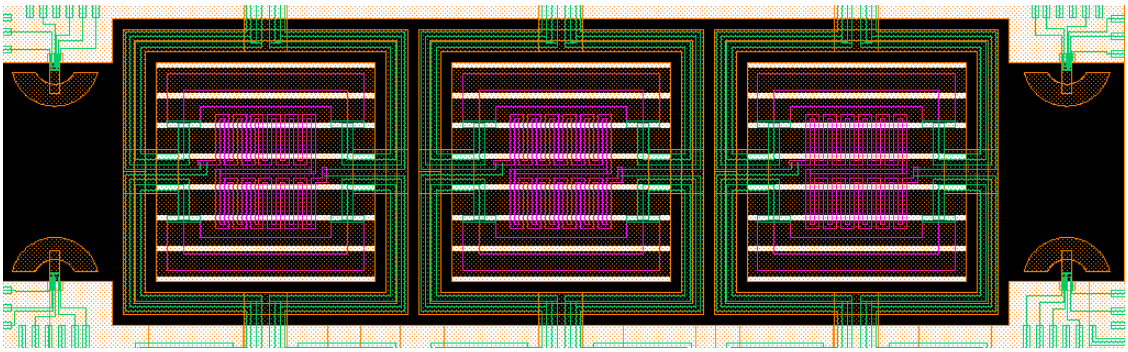

Figure 22 - Screenshot from final mask layout, illustrating design of die with array of three 1 mm x 1 mm µTPC devices. Non-heated sensors and 120 µm ridge spacing on the back surface of the suspended membranes.

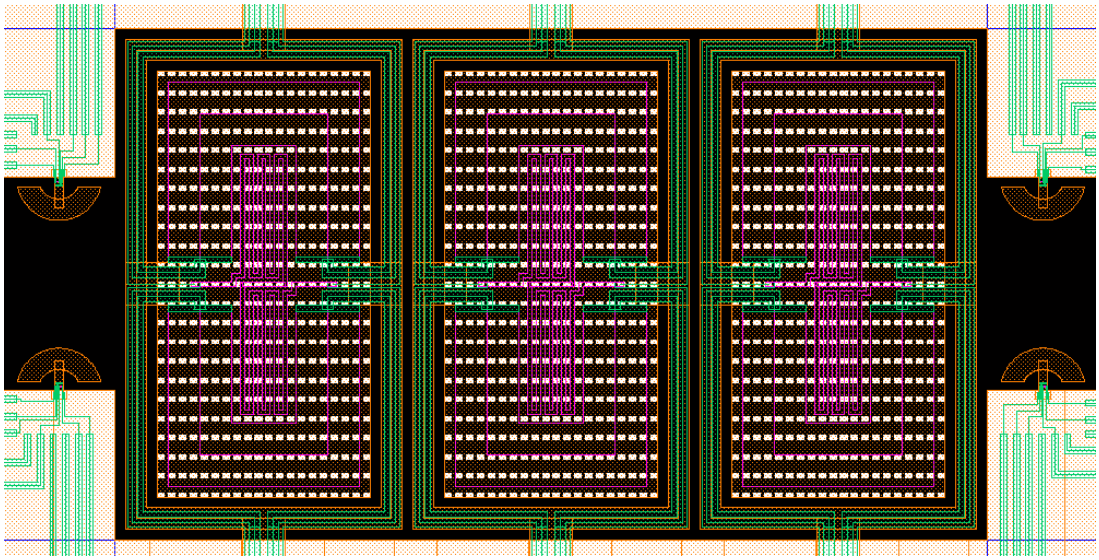

Figure 23 - Screenshot from final mask layout, illustrating design of die with array of three 2 mm x 1 mm µTPC devices. Non-heated sensors and 70 µm pillar spacing on the back surface of the suspended membranes.

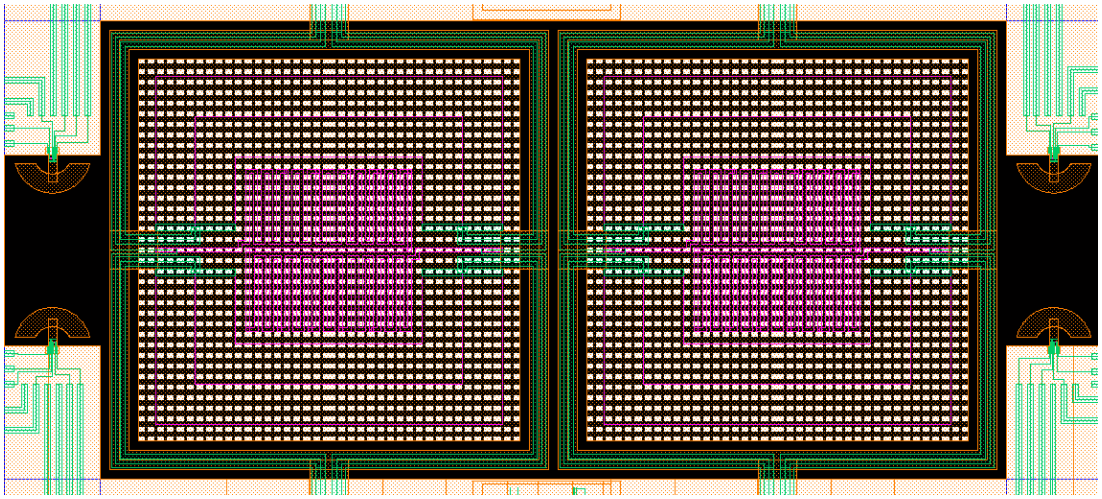

Figure 24 - Screenshot from final mask layout, illustrating design of die with array of two 2 mm x 2 mm µTPC devices. Non-heated sensors and 35 µm pillar spacing on the back surface of the suspended membranes.

With the pillar and ridge arrays determined, the bulk of the remaining mask layout process involved placement of the previously-discussed cantilever-based chemical sensors at each end of the pre-concentrator arrays (Figure 25). The sensors were placed in pairs, across from each other and adjacent to the 1 mm x 1 mm inlet and outlet ports arranged at each end of the chamber. In this configuration, one sensor pair is located upstream and one downstream so that loading of the pre-concentrator array can be monitored in real-time. Additionally, each sensor pair can be operated in a differential mode, where one sensor is coated with sorbent and one is uncoated, so that temperature effects can be filtered out in real-time. Shown in Figure 25 are non-heated designs of the mass-sensitive microsensors with six metallization lines connecting the two thermal excitation resistors and four piezoresistors in a Wheatstone bridge arrangement.

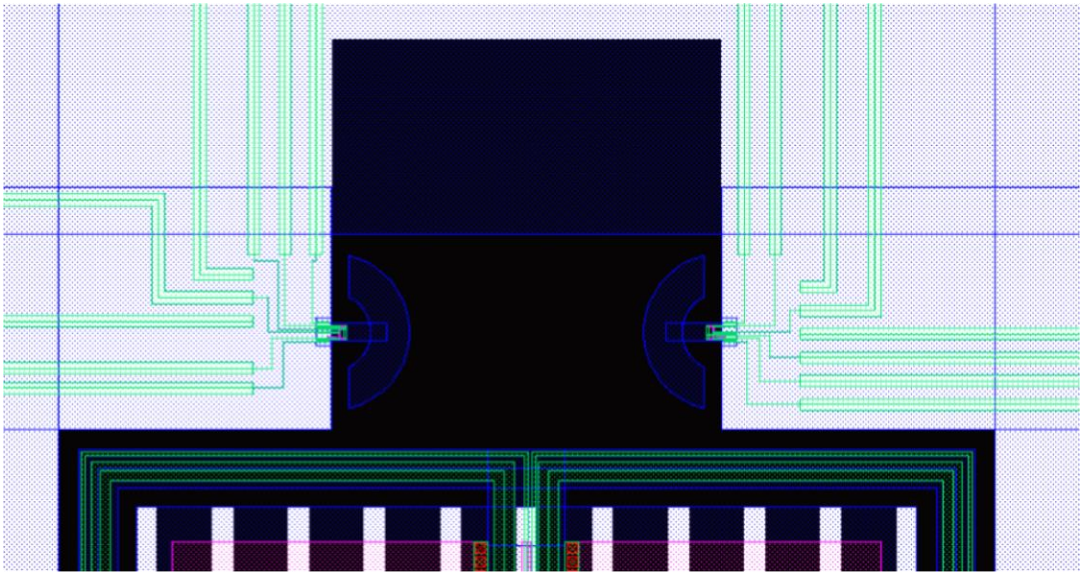

Figure 25 - Detail from final mask layout illustrating placement of cantilever-based chemical sensor pairs (blue semi-circular areas, mid-center) adjacent to inlet and outlet ports (blue rectangular area, top-center). The proximity of the sensor pair to the suspended pre-concentrator membrane (bottom-center) is also shown.

Figures 26-28 show several details of individual die from the completed mask design, illustrating examples of individual pre-concentrator membranes adjacent to a chemical sensor pair. Clearly visible in purple color are the diffused resistors on each µTPC: the largest two are used as heating resistors, while the central one is for temperature monitoring (using a 4-contact measurement). Shown as white rectangles on each of the screen shots are the high aspect-ratio 3-D structures, in this case parallel ridges. The metallization lines connecting the diffused heating resistors are shown in green with small red squares highlighting the contacts between metallization and p-type resistors. The shape of the released microstructures is shown in blue against the black background. Finally the black areas indicate the areas of the silicon handle wafer that are removed by a deep reactive ion etching step from the back of the wafer.

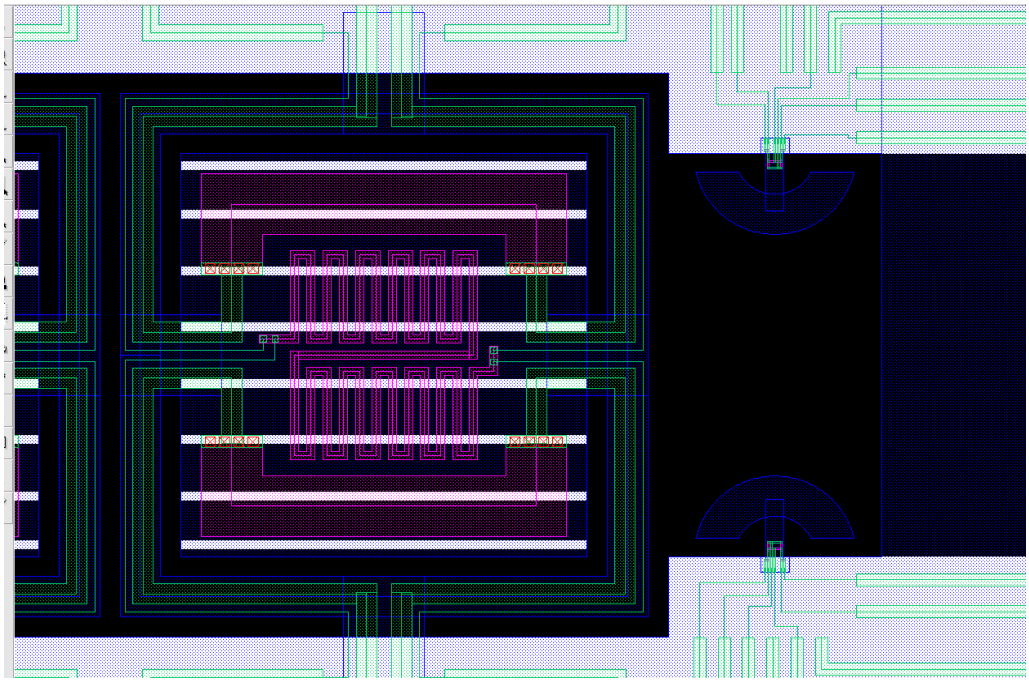

Figure 26 - Detail from final mask layout, illustrating 1 mm x 1 mm pre-concentrator device adjacent to two un-heated resonant sensors located at the integrated inlet/outlet port.

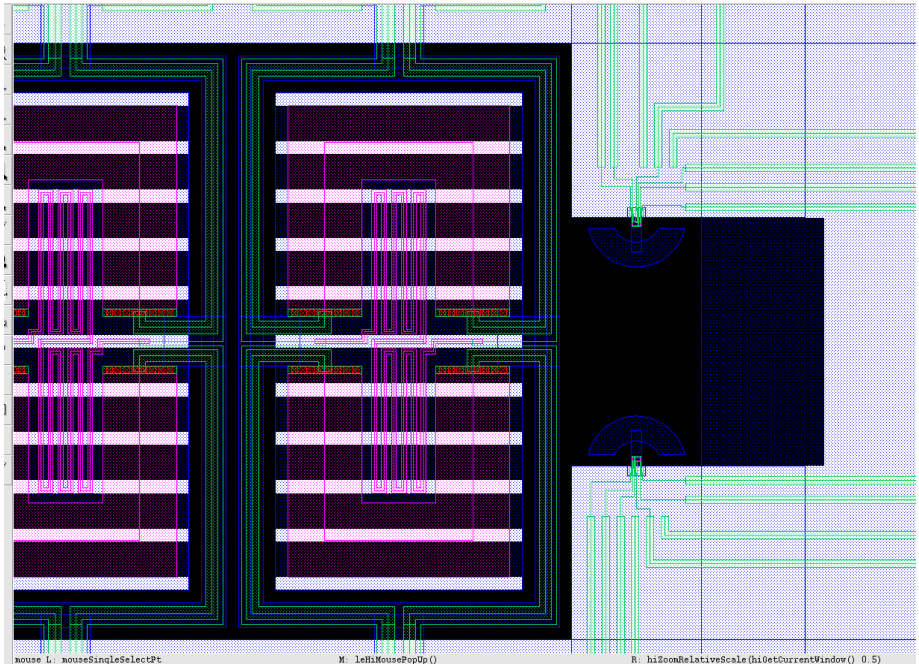

Figure 27 - Detail from final mask layout, illustrating 2 mm x 1 mm pre-concentrator device adjacent to two un-heated resonant sensors located at the integrated inlet/outlet port.

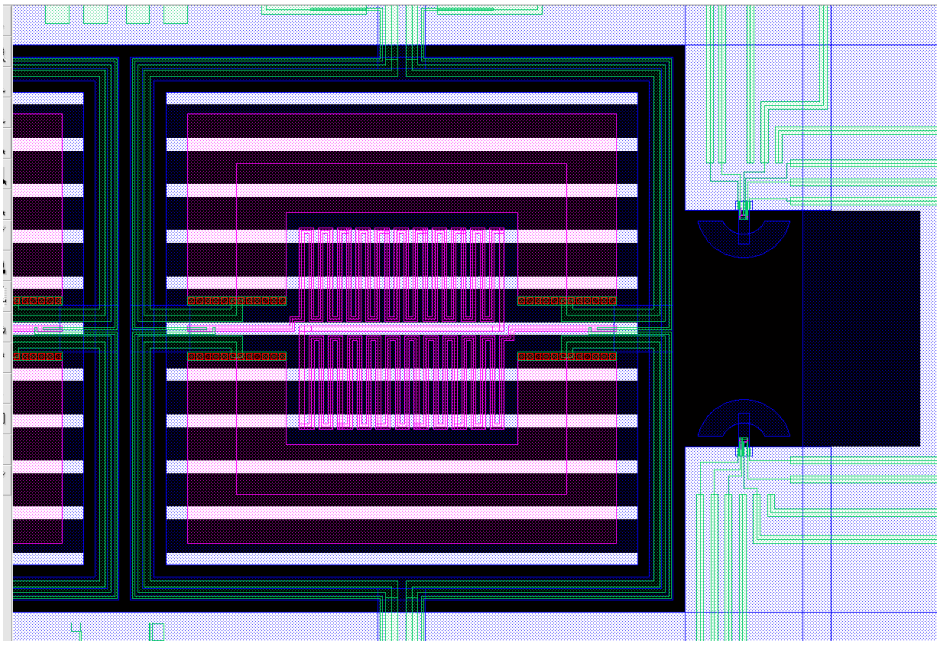

Figure 28 - Detail from final mask layout, illustrating 2 mm x 2 mm pre-concentrator device adjacent to two un-heated resonant sensors located at the integrated inlet/outlet port.

Figures 29 and 30 show large-area views of the final mask layout. The wafer-level die are grouped into three general groups, based on the size of the pre-concentration devices included on each die. Die also differ from one another according to the presence of a desorption heater on the embedded chemical sensors, and according to the number and spacing of high aspect ratio pillars/ridges on the back surface of the suspended membranes. Some die were included which feature only sensors (no pre-concentrators) for testing and characterization of the experimental on-board desorption heaters.

The final mask layout contains 1 x 1, 2 x 1 and 2 mm x 2 mm pre-concentrator designs, as listed in Table 3. Each pre-concentrator die has a size of 6.5 mm x 9 mm; in the case of the 1 mm x 1 mm and 2 mm x 1 mm designs, three µTPC structures are located on each chip, in the case of the 2 mm x 2 mm designs, each chip comprises two µTPC structures. In total, 88 pre-concentrator die are included on a 4-inch wafer (see Figure 30). In addition, the mask layout includes 28 die containing only arrays of mass-sensitive

microsensors, with dimensions of 4.5 mm x 6.5 mm. These cantilever die were used to characterize the mass-sensitive microsensors individually and separately from the µTPC devices, and as arrays coated with different sensing films.

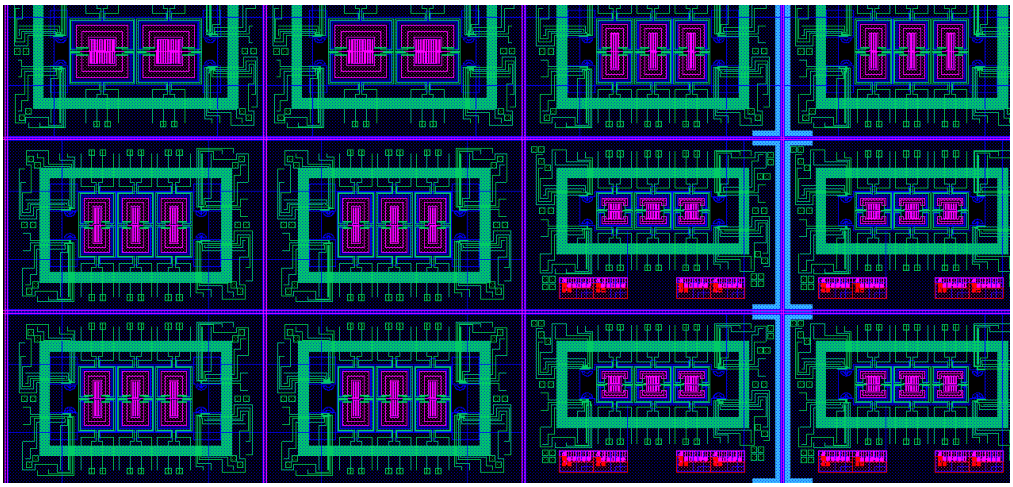

Figure 29 - Screenshot from final mask layout, illustrating placement of several die. The solid green rectangle surrounding each µTPC array is a capping piece formed on the separate packaging wafer, which is used to seal the chamber from the top surface. The bright pink features – near the bottom of the four die on the lower right side of the figure – are a series of alignment marks used as aides during photolithography.

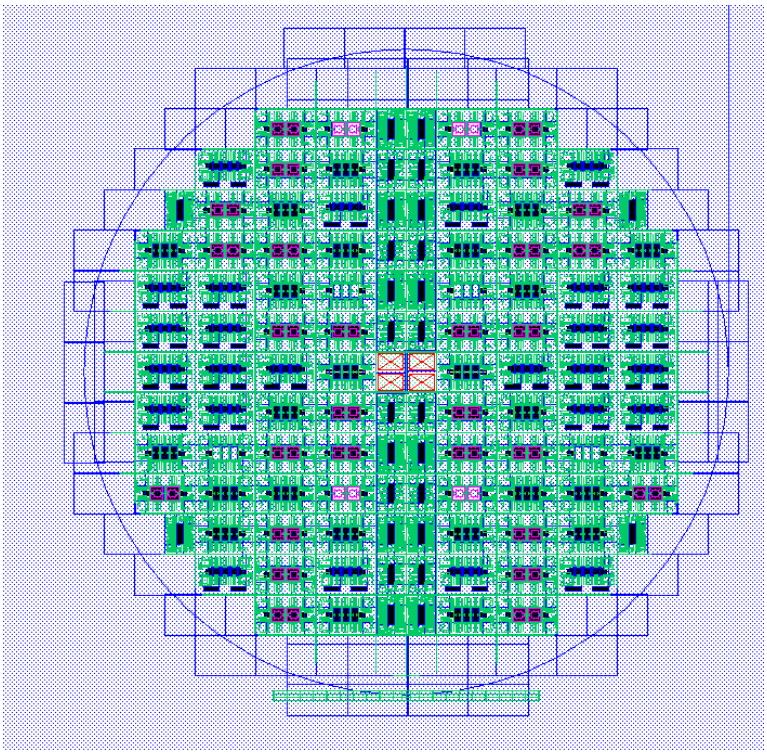

Figure 30 - Screenshot of entire wafer layout, with a total of 88 pre-concentrator dies (6.5 mm x 9 mm each) and 28 cantilever-only dies (4.5 mm x 6.5 mm each), placed vertically down the center column. The center die (marked with four red X's) is used for wafer centering.

The mask set also accounts for the fabrication of a packaging wafer to encapsulate the dies at the wafer-level, thereby minimizing device dead volume and improving future scalability. The complete process flow requires 6 photomasks for the device wafer and 2 photomasks for the packaging wafer, as summarized below:

Mask 1 – Diffusion of p-doped resistors
Mask 2 – Metal contact vias
Mask 3 – Metallization lines
Mask 4 – Device passivation
Mask 5 – Device release
Mask 6 – Backside DRIE etch of high-aspect ratio features

Mask 7 – Capping ring structure for sealing top surface of µTPC chamber
Mask 8 – Alignment marks for alignment between device and packaging wafer

Process Development

In parallel with the mask layout design, a suitable fabrication sequence compatible with both the μTPC arrays and the integrated cantilever-based sensors was developed. Due to the inter-related nature of and dependencies between the two, both the mask layout and the fabrication process design were developed simultaneously, in a cyclical and iterative manner. For example, the possibility of slight misalignment occurring during a lithography step requires the introduction of tolerances into the drawn layouts for sequential mask layers. Likewise, the design choice to implement a wet etch for defining the metal traces constrains the mask layout traces to be drawn wider than they actually appear on the completed device, due to undercutting that arises from the isotropic nature of the etch. Experience and knowledge gained from work on previous devices proved invaluable, and was leveraged as much as possible for the sake of speed and efficiency throughout this inter-dependent process.

In fact, the fabrication sequences for past sensors had already achieved a substantial level of complexity and maturity prior to the commencement of this work. These designs typically employed a 6-8 mask processing sequence, based on epitaxial silicon substrates [74, 93, 94, 102, 103]. An example processing sequence for cantilever-based resonant sensors is shown in Figure 31.

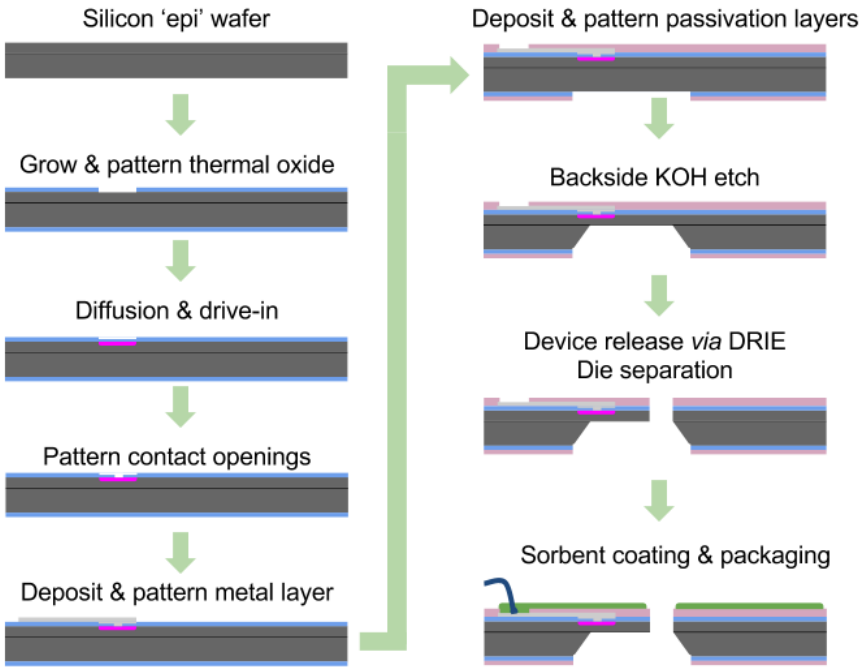

Figure 31 - Typical process flow for suspended resonant cantilever-based sensors formed from epitaxial silicon substrates. Device thickness is controlled with an electro-chemical etch stop.

Fabrication begins with thermal oxidation of an epitaxial silicon wafer, where the thickness of the epitaxial layer defines the final thickness of the released cantilevers. The thermally-grown oxide is then patterned and dry-etched down to the silicon surface to open diffusion windows. High-temperature boron diffusion through the oxide windows into the exposed silicon, followed by a drive-in step, is used to form the heating resistors and piezoresistive Wheatstone bridge necessary for operation of the completed sensors. Electrical contact is made to the diffused resistors *via* contact openings to the silicon and a thin aluminum metallization layer is deposited and patterned to define electrical traces and bond pads suitable for wire-bonding to an external circuit. Nitride passivation is deposited and patterned on the front surface of the wafer to protect the devices from scratches and corrosion, and to enable operation in conductive environments without short-circuiting adjacent metal traces. Additional dielectric thickness necessary for a sufficiently durable

hard mask is deposited and patterned on the back surface of the wafer, and the wafer is then placed in a KOH etch bath for several hours to remove the silicon exposed through the patterned dielectric mask on the back surface. The KOH etch is controlled with an electrochemical etch stop that inhibits the etch mechanism once it reaches the reverse-biased pn-junction formed between the P-type bulk layer and the N-type epitaxial layer. Completion of the KOH etch step results in thin, suspended membranes, which are subsequently patterned and etched *via* DRIE from the front side to release the suspended cantilevers. The importance of a reliable and accurate etch stop in this process cannot be overstated, as the thickness of the suspended cantilevers has a considerable effect on device performance (e.g. resonance frequency, Q-factor). By inhibiting the KOH etch electrochemically, the thickness of the epitaxial layer can be used to precisely control the thickness and uniformity of the released cantilevers resulting in consistent, optimal sensor performance.

SOI Fabrication Development

Due to the crystal-direction-dependence of silicon etching using KOH solutions, however, it cannot be readily adapted to form the high aspect-ratio pillars and ridges necessary to increase the surface area of the μTPC membranes. Such features are possible on SOI substrates, however, where the buried oxide (BOX) layer is used as an etch stop in conjunction with DRIE of silicon. Thus, a design decision was made to modify the well-established and mature epitaxial substrate-based processing sequence so that it could be implemented on SOI substrates, enabling both pre-concentrators (with their large-area membranes and high aspect-ratio pillars and ridges) and mass-sensitive chemical sensors

to be processed simultaneously on the same substrate. This modified fabrication process has been designed to be fully compatible with the existing chemical sensor designs so that sensor performance is not compromised by the switch to SOI. Figure 32 illustrates the modified fabrication sequence, requiring six masks for the device wafer.

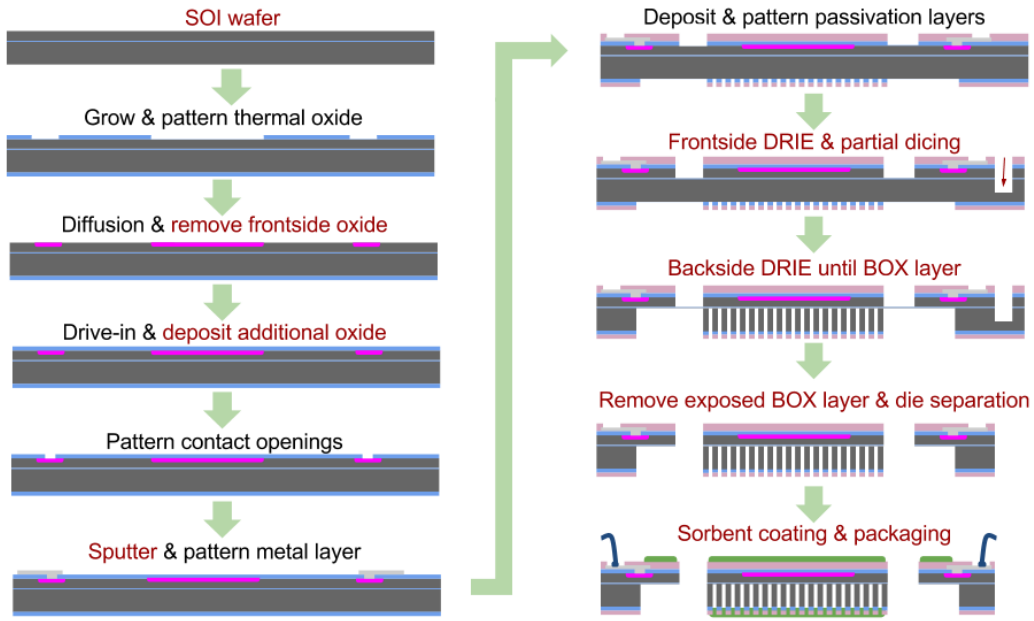

Figure 32 - Process flow diagram showing fabrication steps for µTPC devices formed on SOI substrates. The process sequence is compatible with existing resonant cantilever-based sensors. Red text indicates modifications to the previous process flow, which was based on epitaxial substrates.

In the modified sequence, fabrication begins with thermal oxidation of an SOI wafer, where the thickness of the device layer defines the final thickness of the released cantilevers and µTPC membranes while the thickness of the handle layer defines the height of the high aspect-ratio pillars and ridge structures. The thermally-grown oxide is then patterned and dry-etched down to the silicon surface to open diffusion windows, as before, and high-temperature boron diffusion through the oxide windows into the exposed silicon is used to form heating resistors and piezoresistors. In the modified sequence, however, all oxide is

removed completely from the front surface prior to drive-in. This step serves to re-planarize the front surface of the wafer, reducing unnecessary topography and improving the yield for all subsequent processing steps. Following drive-in, additional oxide is deposited *via* PECVD in order to increase dielectric thickness and reduce the possibility of dielectric breakdown during μTPC heating. Electrical contact is made to the diffused resistors *via* contact openings to the silicon and a thin aluminum metallization layer is deposited and patterned to define electrical traces and bond pads suitable for wire-bonding to an external circuit. While the previous processing sequence employed e-beam evaporation of pure aluminum for the metallization layer, the modified sequence opted instead for sputtering of Al-Cu(1%). Sputter coatings generally exhibit enhanced step coverage over e-beam evaporation, and the introduction of copper into the metallization has been demonstrated to reduce electromigration effects. As before, nitride passivation is deposited and patterned on the front surface of the wafer to protect the devices from scratches and corrosion, and to enable operation in conductive environments without short-circuiting adjacent metal traces. Additional dielectric thickness necessary for a sufficiently durable hard mask is deposited and patterned on the back surface of the wafer, and the wafer is then patterned and etched from the front surface down to the BOX layer *via* DRIE to define the shape of the cantilevers and membranes.

A significant design choice was made at this point to reorder the processing sequence so that the dicing step could be accomplished prior to final device release. As was discussed in Chapter 2, the ideal membrane would be as thin as possible (for reduced thermal mass, and increased surface-area-to-volume ratio) but there are practical limits to the dimensions of a physically-realizable suspended membrane structure. These limits are

determined by available fabrication and packaging technologies, and the corresponding decrease in yield imposed by reducing the thickness of a suspended membrane that is inherently fragile. In some cases, the choice of fabrication approach can dramatically affect the projected yield, with more fragile structures being more sensitive to manufacturing methods. For example, it is common practice to separate the die on a wafer with a dicing saw at the end of the manufacturing process, upon completion of all other fabrication steps. This presents a problem for a delicate, suspended membrane structure, however, as the necessary slurry used during dicing can fracture the exposed membranes and significantly reduce yield. If the dicing step can be moved up in the sequence so that it occurs prior to final membrane release then the loss in yield due to dicing can be virtually eliminated, enabling the manufacture of more aggressive membrane dimensions. In the case of the modified SOI process flow, a *partial* dicing of the wafer occurs where the wafer is diced partway through the handle layer immediately following the front-side DRIE etch. This technique allows for the wafer to be handled as a complete wafer for the remaining fabrication steps, with die separation accomplished by gently fracturing off individual die following completion of all processing. In this way, the partial dicing technique allows for more aggressive membrane geometries to be targeted by dicing – with its accompanying destructive slurry – before the membranes are released and fragile, without compromising on dicing yield. Alternatively, die could be laser diced (i.e. without slurry) at the end of the processing sequence, but this capability is not available at Georgia Tech.

Following the partial dicing step, fabrication continues with a DRIE etch from the back surface of the wafer down to the BOX layer, with subsequent removal of the BOX layer *via* dry plasma etching of SiO_2. Due to the high selectivity (200:1) of the DRIE

process for silicon vs. SiO_2, the BOX layer serves as a very effective etch stop resulting in all suspended features having uniform thicknesses despite non-uniformities in the DRIE etch rate across the wafer. Again, the use of a reliable and accurate etch stop to determine accurate thicknesses and maintain uniformity is critical for achieving high yield with consistent, optimal sensor performance.

Initial Fabrication Results

Prior to undertaking a complete processing sequence on costly SOI wafers, various aspects of the design were first qualified individually on less-expensive silicon prime wafers. For example, viability of the ridge and pillar dimensions was proven initially by processing only that particular mask with bare silicon wafers. Figures 33 and 34 illustrate some results from those initial experiments, demonstrating that the ridge and pillar arrays were capable of being formed as designed. It is clear, however, that the initial etching parameters were not optimized. For example, the pillar structures in Figure 33 show considerable under-etch stemming from non-90˚ sidewalls and would likely not survive sorbent coating. Nonetheless, with time the DRIE parameters were sufficiently optimized to enable processing the DRIE mask in conjunction with the front-side device release mask on a bare silicon wafer. Due to the lack of a BOX layer – and a corresponding etch stop – the etch depths for these initial tests were controlled simply by monitoring the number of etch cycles and estimating depth. This lack of precise control resulted in released membranes that were relatively thick (70 μm), with thicknesses varying roughly 10-15% across the wafer due to non-uniformities in the etch rate across the wafer surface.

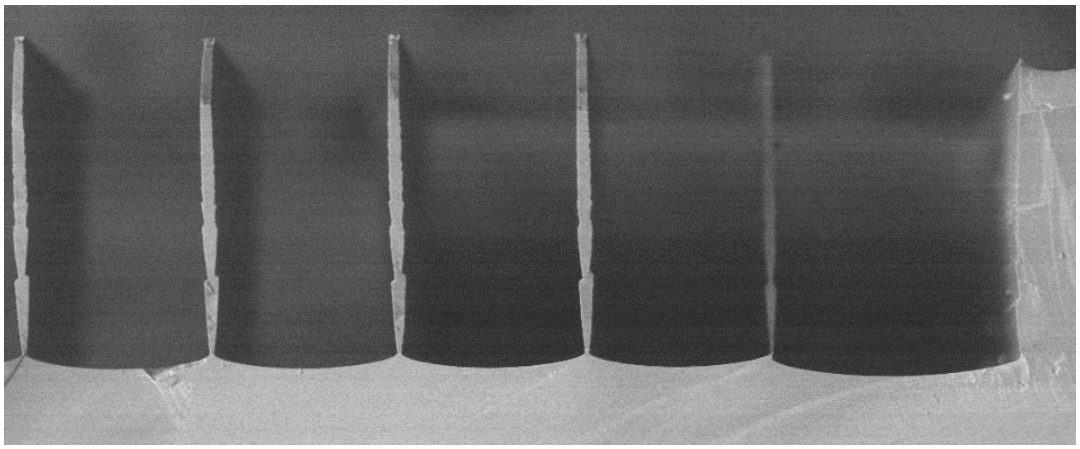

Figure 33 - SEM images illustrating results of initial DRIE development for ridges and pillars. Further refinement was necessary to reduce the undercutting and improve the sidewall angle.

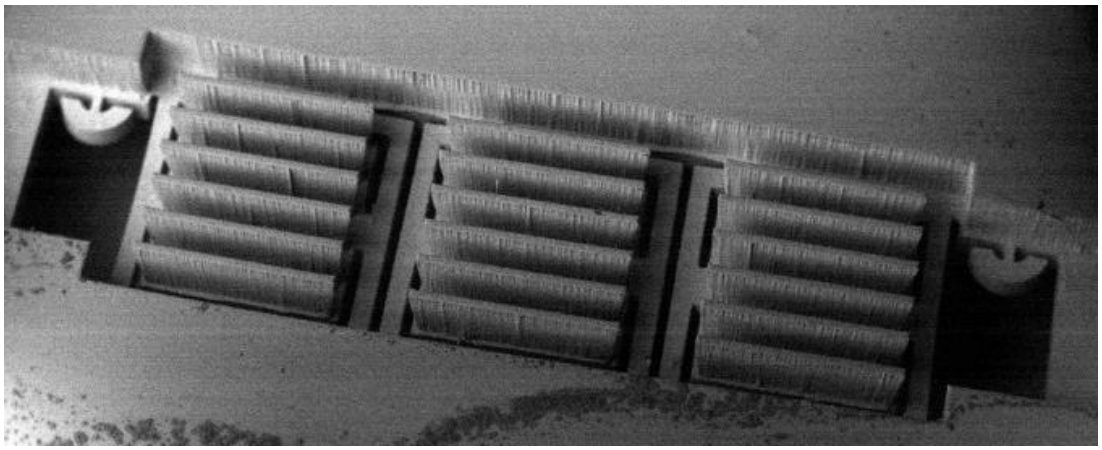

Figure 34 - SEM image of a released 1 mm x 2 mm pre-concentrator with ridge-type structures imaged from back surface. Also visible are the mass-sensitive resonator structures at the bottom of the image. These initial devices were fabricated without the use of an etch stop, resulting in membranes that were approximately 70 µm thick.

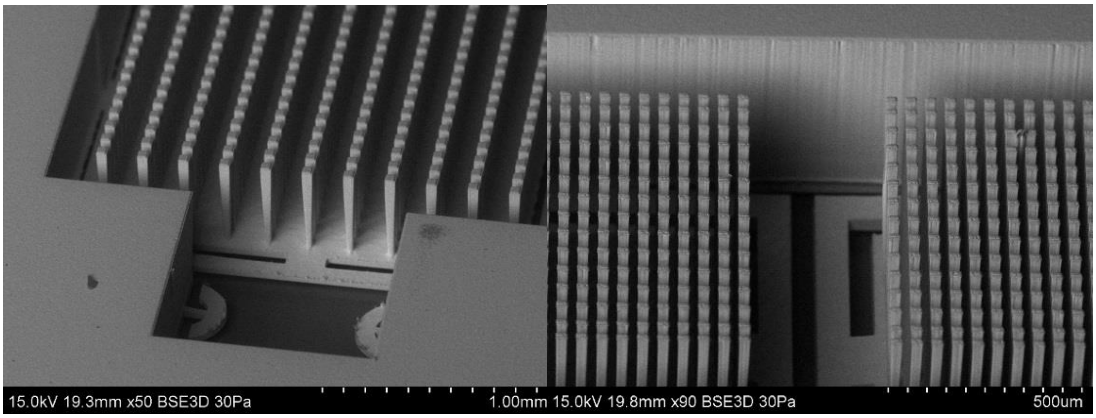

Figure 35 - SEM images of a released 1 mm x 1 mm pre-concentrator with pillar-type structures imaged from back surface. These initial devices were fabricated with an improved DRIE recipe but without the use of an etch stop, resulting in membranes that were approximately 35 µm thick and with poor thickness uniformity across the wafer.

Despite these drawbacks, the successful fabrication of initial devices demonstrated basic viability of the modified process sequence. Subsequent processing commenced on true SOI substrates, which soon resulted in successfully processed devices with uniform 25 µm thick membranes as illustrated in Figure 36.

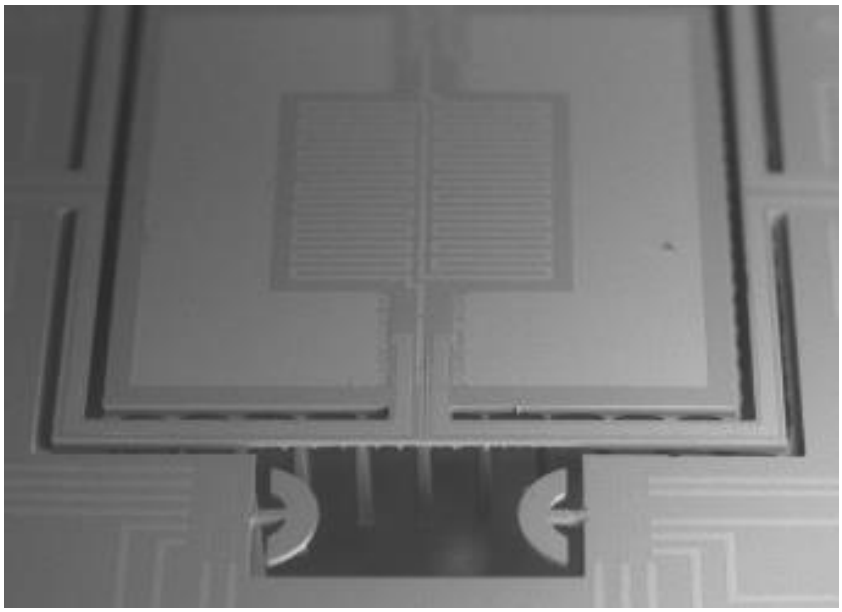

Figure 36 - SEM image of a released 2 mm x 2 mm pre-concentrator with pillar-type structures imaged from top surface. Also visible are the mass-sensitive resonator structures at the bottom of the image. These improved devices were fabricated from SOI substrates where the BOX layer was used as an etch stop for DRIE, resulting in membranes that were precisely 25 µm thick.

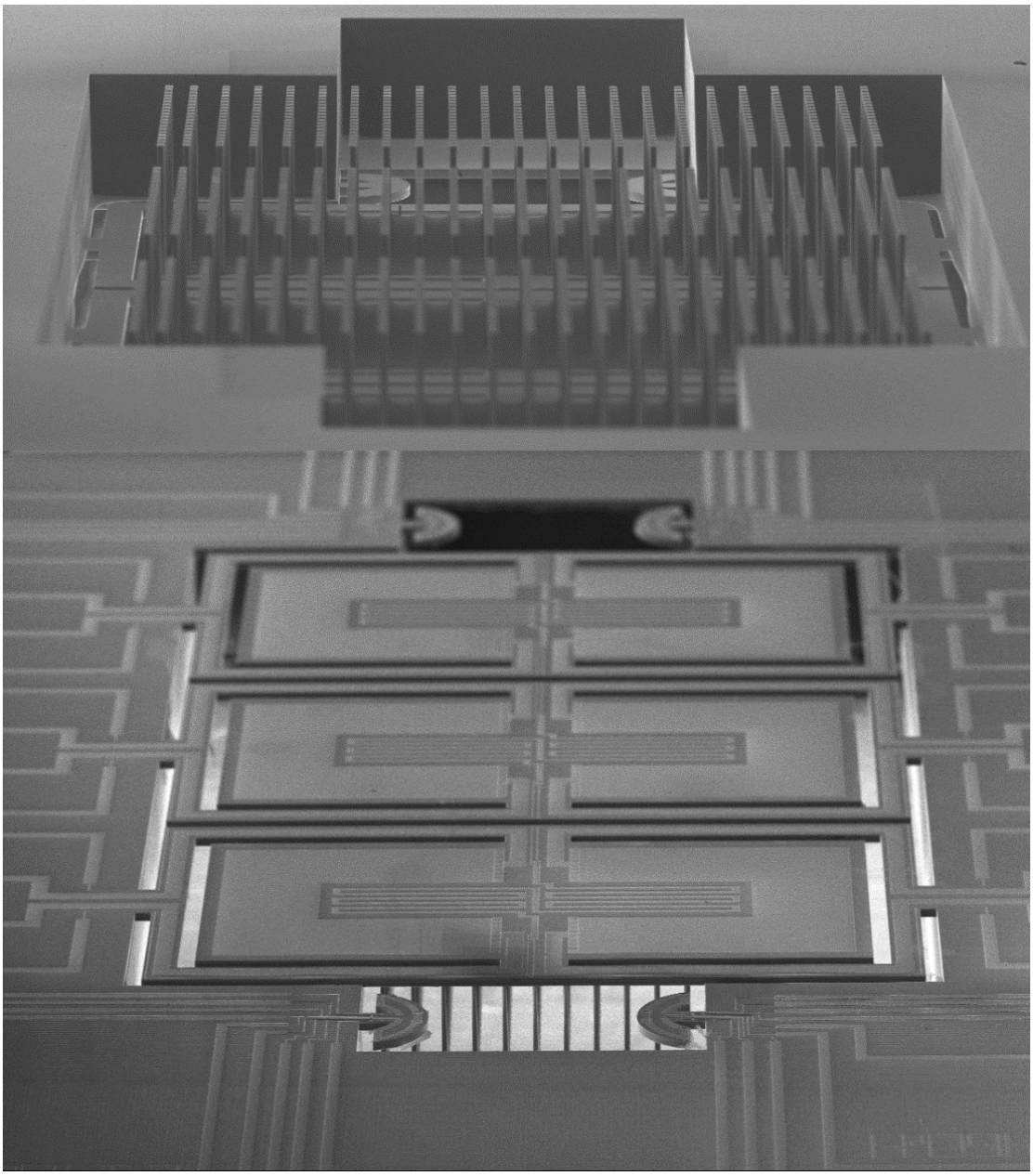

Figure 37 - SEM image of array of released 2 mm x 1 mm µTPC devices with pillar-type structures imaged from top (top) and back (bottom) surfaces. These improved devices were fabricated from SOI substrates where the BOX layer was used as an etch stop for DRIE, resulting in membranes that were precisely 25 µm thick.

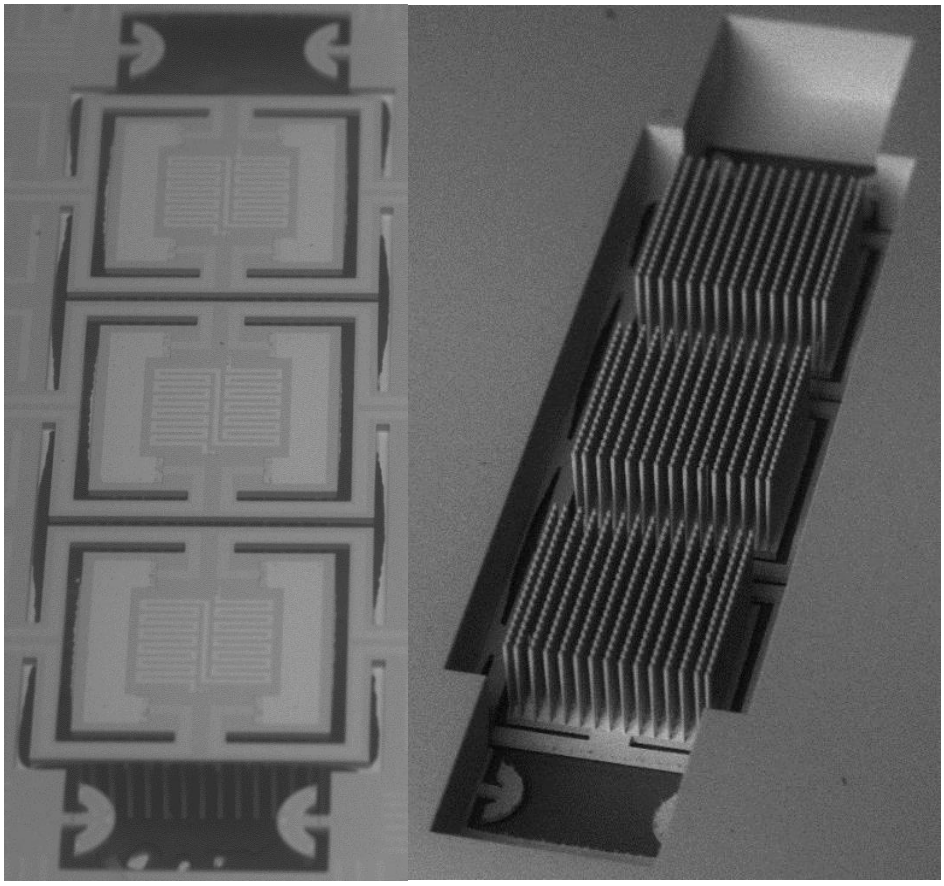

Figure 38 - SEM image of array of released 1 mm x 1 mm µTPC devices with pillar-type structures imaged from top (left) and back (right) surfaces. These improved devices were fabricated from SOI substrates where the BOX layer was used as an etch stop for DRIE, resulting in membranes that were precisely 25 µm thick.

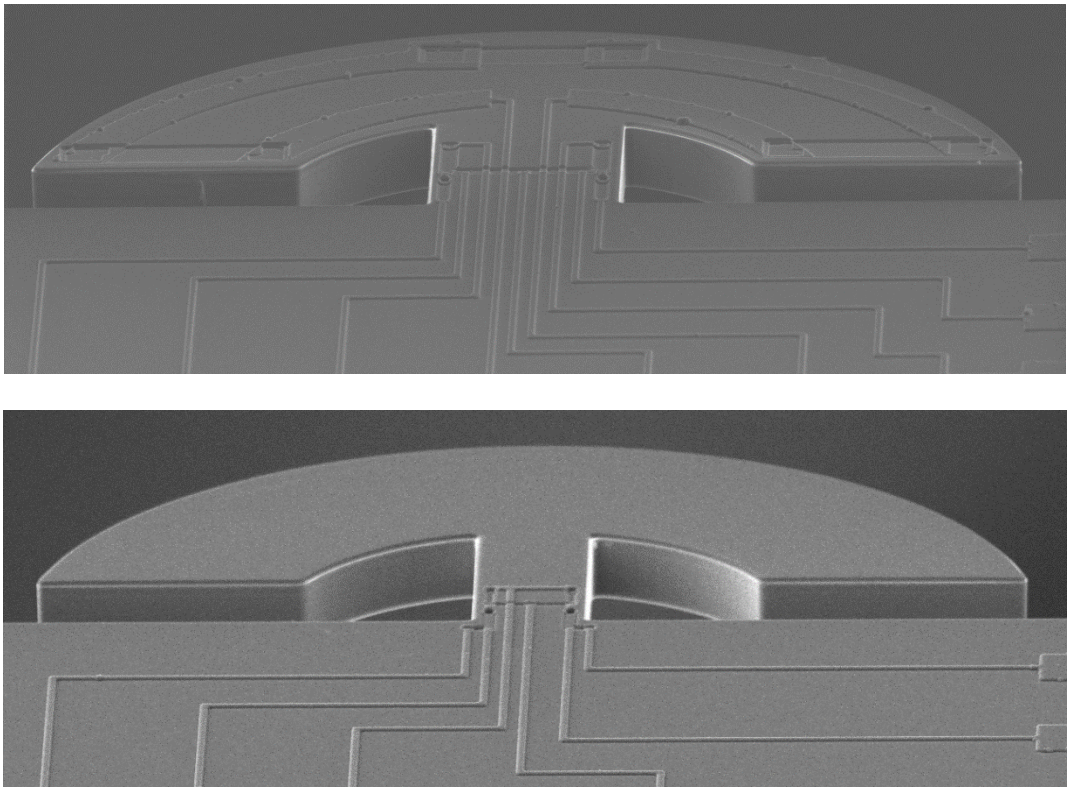

Figure 39 - SEM image of heated (top) and non-heated (bottom) integrated chemical sensors. The sensors were fabricated on-chip with the µTPCs, resulting in a device thickness of precisely 25 µm.

CHAPTER 4 – ELECTRICAL & THERMAL CHARACTERIZATION

Following successful fabrication in the Georgia Tech Institute for Electronics and Nanotechnology (IEN) cleanroom facilities, performance for the various designs was first evaluated *via* electrical and thermal characterization. To facilitate this process, die from each design were mounted into 28-pin DIL ceramic packages and wire-bonded to connect each die electrically to each package (Figure 40).

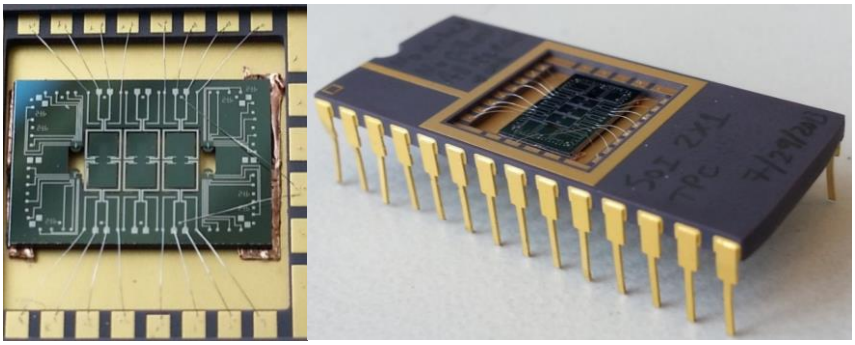

Figure 40 - Photographs of a 2 mm x 1 mm µTPC die mounted in ceramic DIL package.

Once mounted into the packages, the resistances of both the heating and measurement resistors were measured for each design, at room temperature in air. The results of these measurements are summarized in Table 4, and represent approximate values as the resistances varied slightly from wafer to wafer and from die to die. Examination of these results reveals the measured resistances to lie within 10-28% of the designed specifications, with the exception of the measurement resistors for the 2 mm x 2 mm devices (47%).

Table 4 - Summary of electrical and thermal measurement results, compared with the values expected from simulation and theory.

Device	1 mm x 1 mm		2 mm x 1 mm		2 mm x 2 mm	
	Designed	Measured	Designed	Measured	Designed	Measured
Heating Resistance [Ohms]	500	593	500	604	500	553
Measurement Resistance [Ohms]	25k	32k	35k	44k	75k	110k
τ_{therm} [sec]	0.2	0.35	0.4	0.8	0.6	1.3
Temp. Increase ΔT [deg C]	265	194	229	188	271	155
$P_{applied}$ [mW]	500	276	500	287	1000	309
ΔT/Papplied [˚C/mW]	0.53	0.70	0.46	0.66	0.27	0.50

Oven Measurements

Once baseline resistance values were established, the relative and absolute resistance changes due to temperature were evaluated by placing each packaged µTPC in a temperature-controlled chamber and ramping the temperature while monitoring the resistance of each resistor. A Keithley 2400 source-meter was used to apply +10 V of DC bias to the substrate, and an Agilent 34401A DMM was used to measure resistance. To enable relatively high temperatures up to 150 °C, a specialized circuit board was designed with temperature-resistant components and wires. This circuit board contained a socket for holding the ceramic DIL package, and served to interface between the packaged µTPCs

and external measurement equipment by way of electronic feed-through ports on the side of the oven (Figure 41).

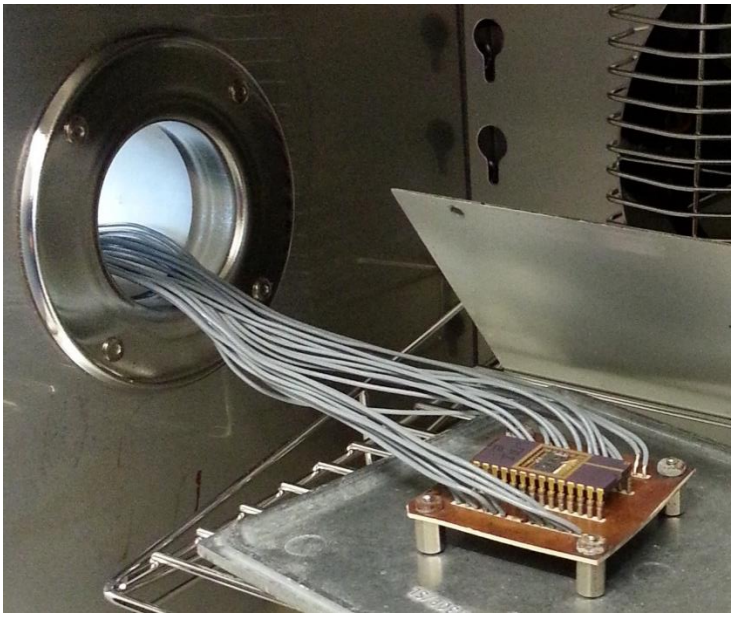

Figure 41 - Photograph of custom-built temperature-resistant PCB, connected to external measurement equipment by way of a feedthrough in the environmental chamber.

In this way, a plot of resistance as a function of temperature was generated for each design, as shown in Figures 42-46. Analysis of the data revealed that the resistance of the measurement resistor actually begins to *decrease* when the membrane temperature reaches approximately 120℃. It is believed that this phenomenon occurs due to expansion of the PN-junctions at elevated temperature, which causes overlap of the junctions to occur among the narrow bends in the long, thin resistor, thereby reducing the effective resistance. In anticipation of this possibility, electrical contacts to the substrate were added during the mask layout design stage so that a reverse-bias voltage could be applied between the n-type substrate and the p-type doping as a way of improving electrical isolation within the devices. With the application of a reverse-bias voltage to the substrate contacts, degradation of the measurement resistor's resistance disappeared and a monotonically-

increasing temperature calibration curve results (Figure 42). The application of the bias to the heating resistors, however, was found to have no effect on the relative resistance change as a function of temperature. In all cases, a reverse-biasing DC voltage of +10 V was applied *via* the substrate contacts between the n-type substrate and the p-type diffused resistors.

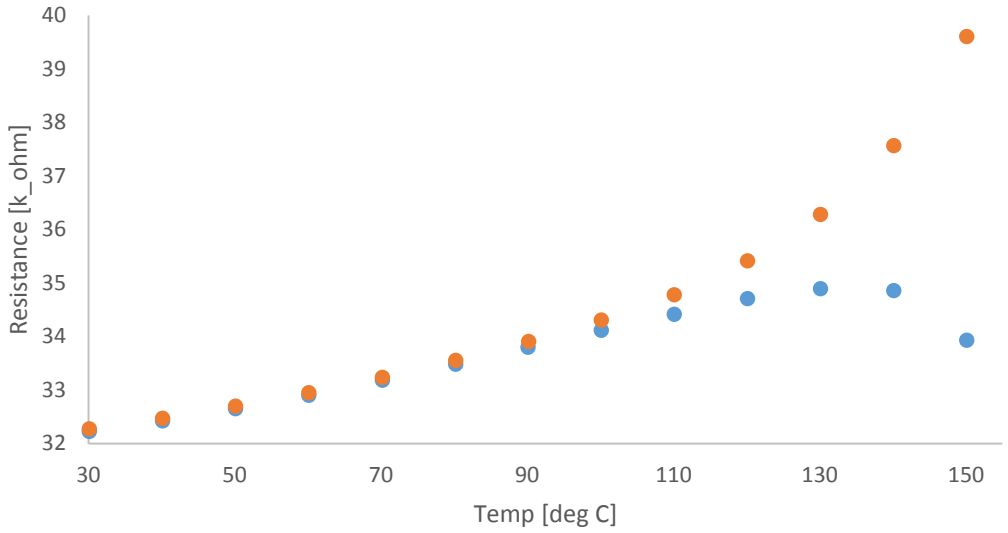

Figure 42 - Measured resistance as a function of ambient temperature for the measurement resistor of a 1 mm x 1 mm µTPC device. The resistance was measured both with (orange) and without (blue) a +10 V DC bias applied to the substrate.

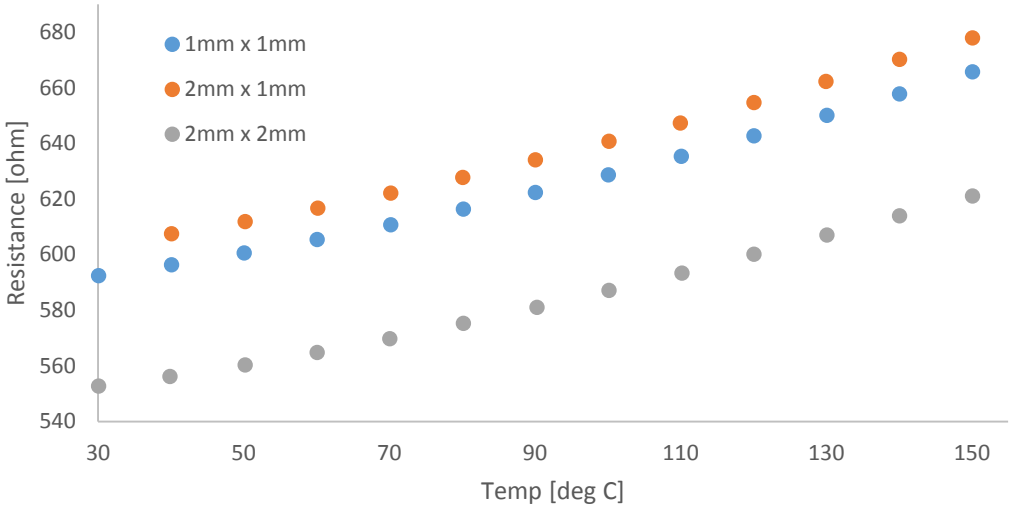

Figure 43 - Calibration data for the heating resistors on 1 mm x 1 mm (blue), 2 mm x 1 mm (orange), and 2 mm x 2 mm (gray) µTPC devices, measured with no bias applied to the substrate. In all three cases, analysis of the measured resistance as a function of the temperature results in a quadratic temperature coefficient of resistance which can be used to estimate temperature elevation of the device during self-heating by simply measuring the resistance.

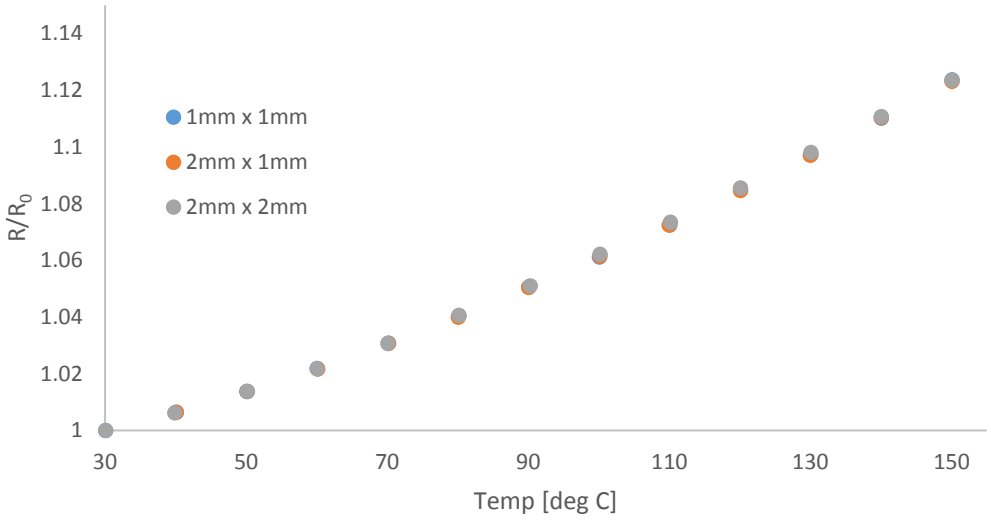

Figure 44 - Plot of normalized resistance change as a function of the chamber temperature for all three heater designs (using data from Figure 43).

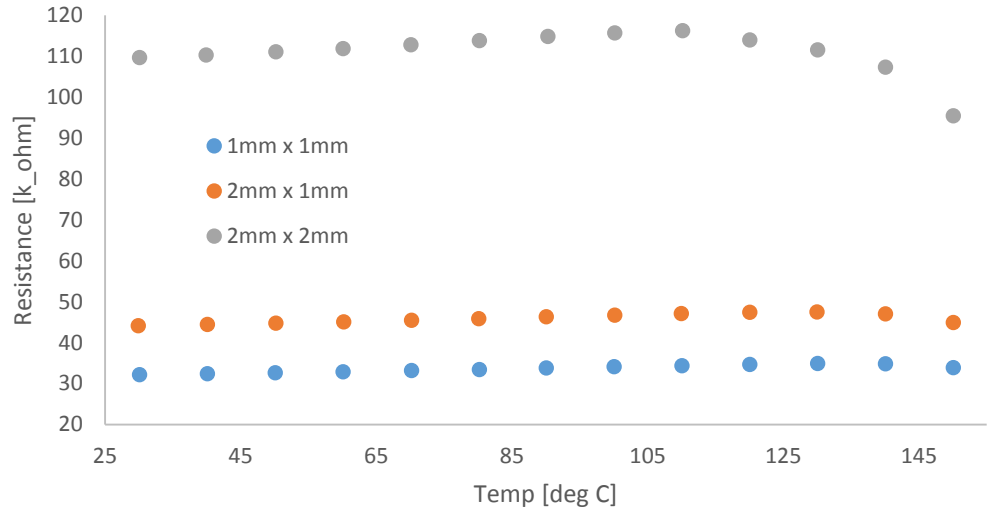

Figure 45 – Plot of absolute resistances as a function of chamber temperature for all three measurement resistors.

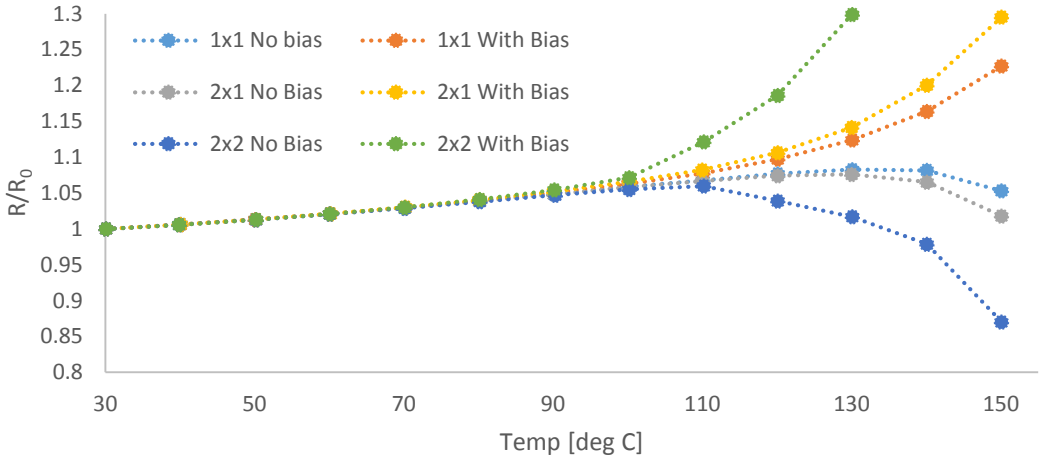

Figure 46 - Calibration data for the measurement resistors on 1 mm x 1 mm (blue), 2 mm x 1 mm (orange), and 2 mm x 2 mm (gray) µTPC devices, measured with and without bias applied to the substrate. In all three cases, analysis of the measured resistance as a function of the temperature does not result in a linear temperature coefficient of resistance which can be used to estimate temperature elevation of the device during self-heating by simply measuring the resistance.

A comparison of the temperature calibration curves for the measurement resistors with those of the heating resistors reveals that the heating resistor response with respect to

temperature is independent of the biasing voltage. This is not the case for the measurement resistors, however, which are more susceptible to changes in PN-junction overlap due to the many tight, narrow bends in their geometries. It is suggested that future designs examine removing the meandering bends from the measurement resistors, so that they will respond predictably and without the need for a substrate bias voltage. Because the temperature dependence of the heating resistors (Figure 43) is more consistent across the three designs and independent of the substrate bias, it was decided to use the heater resistance for temperature monitoring going forward. For the heating resistors, the normalized resistance change as a function of temperature is well described by a quadratic dependence,

$$\frac{R}{R0} = 0.982 + 4.99 \times 10^{-4} \cdot T + 3.02 \times 10^{-6} \cdot T^2$$

Equation 5 – Equation of fit for normalized heating resistance change as a function of temperature (in degrees Celsius).

Self-Heating

After quantifying the effect of ambient temperature on resistance change, heating power was applied directly to the membranes while monitoring the change in resistance for the various embedded resistors (Figures 47-50). These measurements were performed with a Keithley 2400 SourceMeter, by applying a voltage to the heating resistors (connected in parallel) and measuring the current flow. From the obtained I-V data, the heating power P = I V and the heating resistance R = V/I are readily extracted. In all cases, a +10 V bias was applied to the substrate contacts. Figures 47-50 plot the results of these experiments.

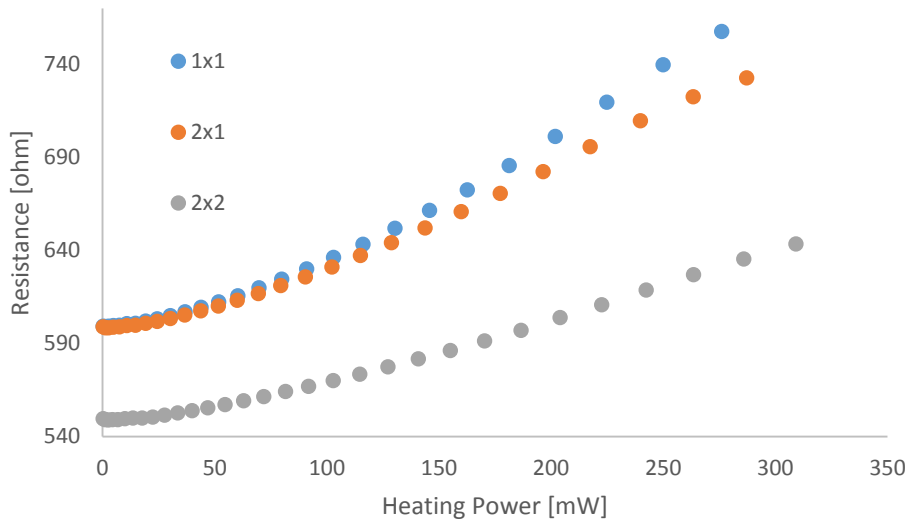

Figure 47 – Plot of absolute resistance values for all three heaters as a function of heating power.

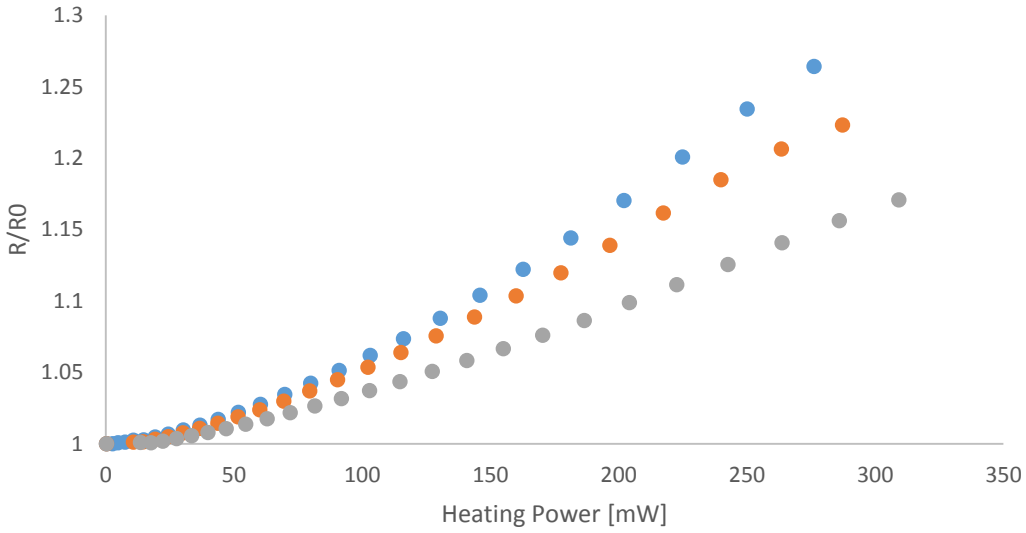

Figure 48 - Plot of normalized resistance values for all three heaters as a function of heating power.

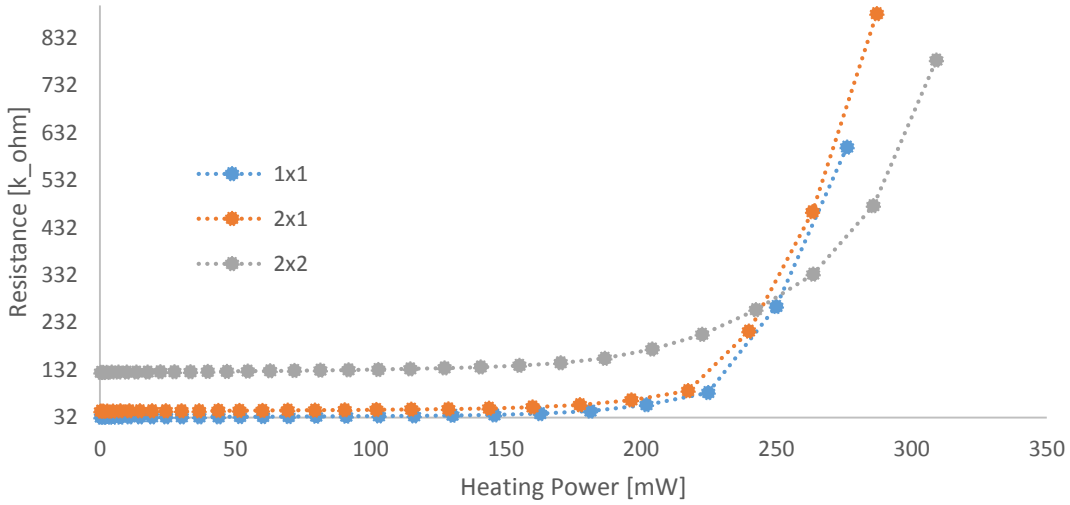

Figure 49 – Plot of absolute resistance values for all three measurement resistors as a function of applied heating power.

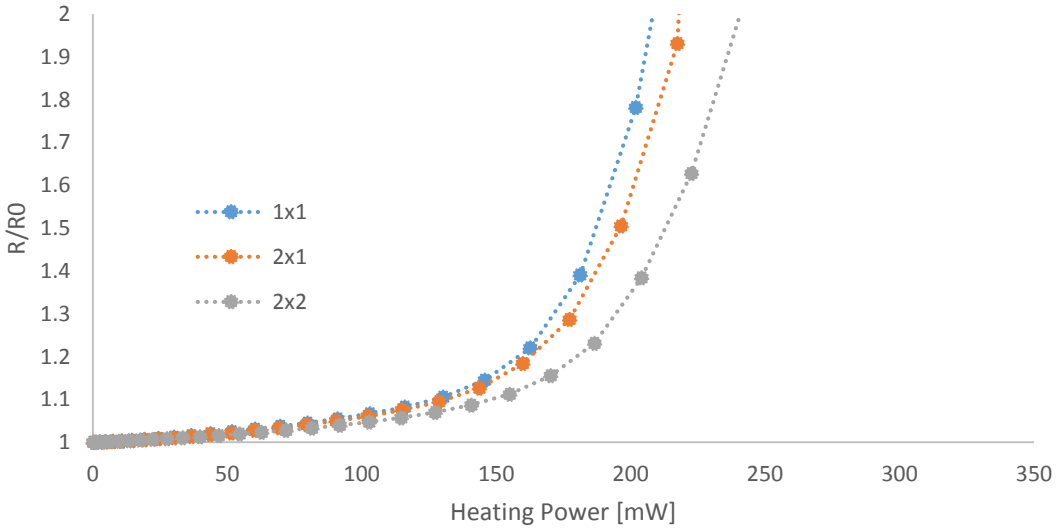

Figure 50 - Plot of normalized resistance values for all three measurement resistors as a function of applied heating power.

By utilizing the temperature calibration data from Figures 42-46, the membrane temperature can now be estimated by measuring the resistance change during self-heating (from the calibration curves for the heating resistors, it was assumed that the quadratic fit

can be extrapolated up to 250˚C). Figure 51 shows the resulting membrane temperature for each design as a function of the applied heating power. For example, a heating power of 287 mW applied to the 2 mm x 1 mm device results in a membrane temperature increase of 188˚C (461 K). As expected, the membrane temperature increases linearly with the applied heating power (Equation 1).

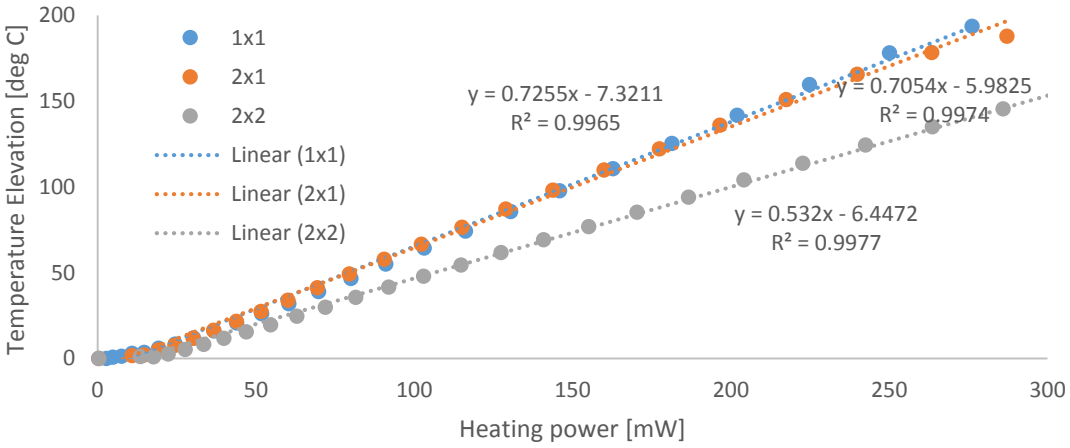

Figure 51 - Estimated membrane temperatures for 1 mm x 1 mm (blue), 2 mm x 1 mm (orange), and 2 mm x 2 mm (gray) µTPC devices, measured with a +10 V DC bias applied to the substrate. The temperatures are estimated by measuring the temperature-dependent resistance during self-heating and comparing this value with the temperature calibration data curves.

The measured temperature increases indicate that the simulations performed during the design stage underestimated the temperature elevation for a given heating power. For the 2 mm x 1 mm device with 20µm membrane thickness discussed in Chapter 2, simulations predicted a temperature increase of 229˚C for a heating power of 500 mW (see Figure 10), but the experimental data indicate a temperature increase of 188˚C for only 287 mW of applied heating power. Considering that the tested device is slightly thicker (25 µm) and is composed of additional materials (e.g. aluminum, SiO_2) compared to the pure silicon structure assumed in simulation, the measured temperature elevation should be even

less (e.g. due to reduced thermal resistance in the thicker support legs and increased thermal conduction along the metal lines). It appears that the heat transfer to the air, simulated in form of a constant heat transfer coefficient of $h = 50\ Wm^{-2}K^{-1}$ applied to all surfaces, has been overestimated. In fact, it is likely that in-between the ridges and pillars the heat transfer to the air is much less effective than e.g. at the top of the ridges or the opposite side of the membrane. To improve the simulation results, heat transfer through the air would have to be modeled more accurately by considering heat conduction through the air with the chip simulated within its full package.

It should also be noted that small non-linearities in the dependence of the membrane temperature on the heating power can be expected. As an example, the thermal conductivity of silicon and of the surrounding air are temperature-dependent, which would introduce non-linearities into the estimated temperature curve. As a final note, the temperature calibration data were taken with the entire packaged chip mounted inside of a temperature-controlled chamber, resulting in there being no temperature gradient between the suspended membrane and the ceramic packaging. In the case of self-heating, however, the membrane alone is heated while the ceramic package remains at a much cooler temperature. This situation results in a temperature gradient across the suspended membrane – and between the membrane and substrate – which leads to certain regions of the resistors having cooler temperatures (and therefore reduced resistances). These effects are not accounted for in the method used to calibrate the change in resistance as a function of membrane temperature. It is suggested that future work explore the use of a thermal imaging system as an independent verification of membrane temperature elevation during self-heating.

Thermal Transient Behavior

Following characterization of resistance change with respect to temperature, thermal transient measurements were performed. To extract the thermal time constant of the µTPC devices, a DC bias current of 100 µA was applied to the measurement resistor. A 200-mW heating pulse was then applied to the heating resistors while simultaneously measuring the voltage change across the biased measurement resistor (Figure 52).

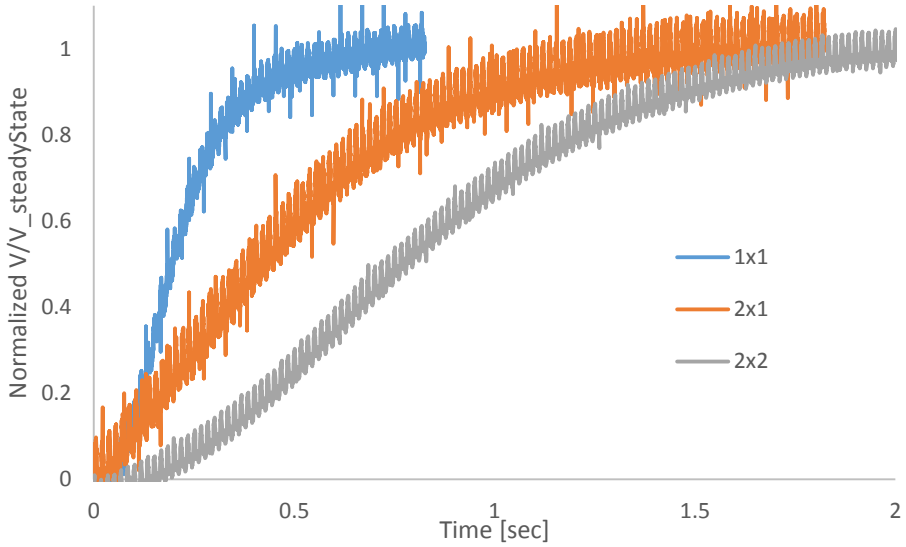

Figure 52 - Normalized thermal transients for all three designs.

The resulting normalized transients for each design are shown together in Figure 52, indicating thermal time constants below 1.5 seconds for all three designs. As expected the temperature exponentially approaches a steady state value when the heating pulse is applied, with the thermal rise time increasing as a function of the thermal mass of the suspended membranes. A comparison of the measured thermal time constants with the simulated predictions is summarized in Table 4.

CHAPTER 5 – SORBENT COATING & PACKAGING

While the designs have thus far been successfully fabricated and experimentally validated for proper electrical and thermal performance, application of a suitable sorbent layer is necessary for chemical functionality. For optimal chemical pre-concentration capacity, only the suspended membranes and high-surface-area 3-D ridge/pillar structures on the membranes would be (uniformly) coated with sorbent. Motivated by this requirement, various deposition techniques were investigated, which allow for individual devices in the array to be locally coated with separate sorbent materials. The exploration of sorbent coating techniques commenced with the following methods, which are available in the laboratory and cleanroom facilities of Georgia Tech:

- Drop-coating from pipette
- Inkjet printing
- Spray-coating with air brush
- Plasma-coating (through collaboration)

Drop-Coating

Due to the relatively large size of the membrane structures – and the correspondingly large sorbent masses required for full coverage – the possibility of drop coating the sorbent solutions directly from a micro-pipette was the first method to be investigated. Initial tests were performed by drop-casting 4 µL droplets of PIB dissolved in toluene (0.2wt%) with a micro-pipetter onto ridge test structures (Figure 53) remaining from the DRIE process development discussed in Chapter 3.

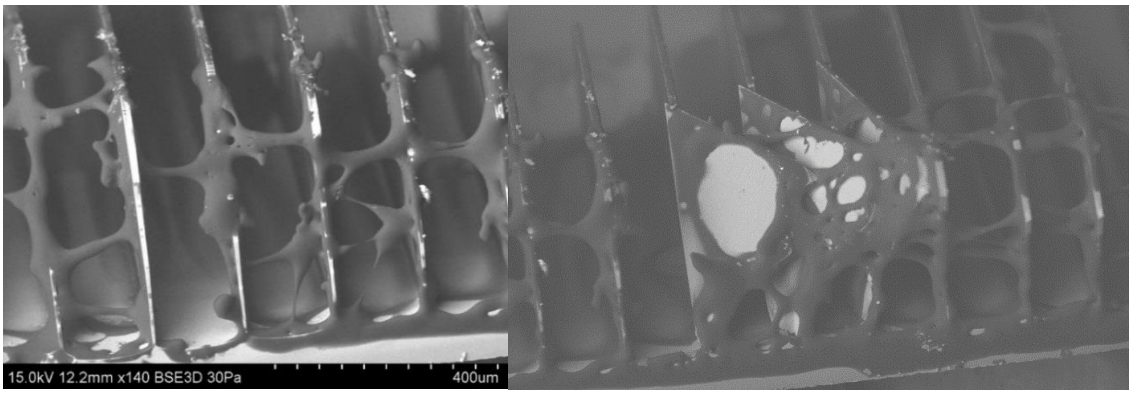

Figure 53 – SEM micrographs of silicon ridge structures coated with PIB by drop-coating of the polymer solution (toluene was used as solvent) from a micro-pipette.

This approach offers simplicity and speed, as entire devices can be coated in a matter of seconds, but resulted in layers that were inconsistent from device to device. As can be seen in the SEM images (Figure 53), the polymer solution does not properly wet the silicon surfaces inside the trenches, resulting in non-uniform deposition. In some cases, drop-coating even resulted in damage to the ridge/pillar structures. Additionally, drop-casting of the sorbent layers proved indiscriminant and difficult to constrain the layers within the boundaries of individual membranes, resulting in unwanted coating of adjacent membranes and much of the supporting substrate. This situation is non-ideal, as the substrate's thermal response is markedly different from that of the suspended membranes. Thus, sorbent coatings deposited on the substrate will capture a portion of the sample analyte concentration, but will not release the captured molecules during thermal desorption, as the substrate is thermally isolated from the self-heating membranes and remains relatively cool. Ultimately, this scenario contributes to a diminished pre-concentration factor. It is suggested that future work revisit this technique, and explore the possibility of utilizing different solvent systems and surface modifications that could render the device surface more amenable to wetting for the dissolved sorbent.

Inkjet Printing

In addition to drop-casting, the use of inkjet printing as a possible coating technique was also explored as it has been demonstrated to be capable of achieving localized polymer deposition onto silicon microstructures [27, 76, 93]. With this approach, the sorbent polymer is typically dissolved in a suitable solvent and subsequently ejected onto the substrate through a micro-nozzle *via* ultrasonic piezoelectric actuation (Figure 54).

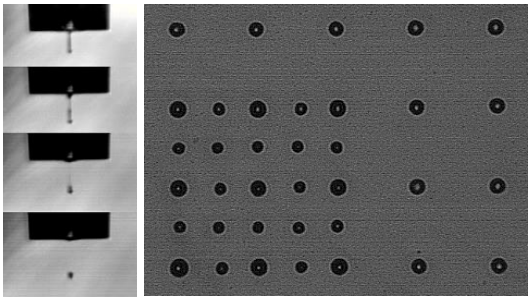

Figure 54 - Stroboscopic images (left) taken during inkjet printing of a solution of polyisobutylene (PIB) dissolved in o-xylene and (right) array of droplets deposited via inkjet printing from a solution of sugar dissolved in water. Printing was performed on a MicroFab JetLab II inkjet printer located in the IEN cleanroom facilities at Georgia Tech.

This versatile technique allows for polymer deposition onto non-planar substrates, and can be used to print precise, arbitrary patterns through the use of software scripting (Figure 54). Initial experiments made use of an ink-jet printing platform (Microfab, JetLab) available in the IEN cleanrooms at Georgia Tech, and consisted of printing simple patterns of PIB dissolved in xylene (0.1wt%) onto both planar silicon surfaces and ridge/pillar test structures. Additional experiments involved printing of relatively thick (1-2 μm) PIB, EPCO, and PVAc patterns, and demonstrated basic feasibility of inkjet printing as a method for coating individual μTPC membranes. In an effort to avoid nozzle clogging, dimethyl sulfoxide (DMSO) was used as a solvent for polyvinylacetate (PVAc), and xylene as a

solvent for EPCO and PIB, due to their relatively high boiling points and thus slow rate of evaporation during the ink-jetting process [93].

When considered as a whole, however, inkjet printing proved to be an ineffective technique for printing high-quality polymer films onto the suspended membranes for a variety of reasons. For example, the range of suitable solvents necessary to dissolve the polymer sorbents can be limited by incompatibility with the printing process itself (specifically, the adhesives used in nozzle construction). It has also been observed that certain polymer/solvent combinations result in non-uniform films, where the deposited polymer film is considerably thicker near the edges of the film and thinner in the center. This phenomenon is known as the "coffee ring" effect (Figure 55) and can be mitigated through the use of multiple solvents in the sorbent mixture, but this adds cost and complexity and still requires specific mixtures to be adjusted for each sorbent mixture [76, 93]. Most importantly, inkjet printing is an inherently serial process and can require considerable time to coat large-area structures, such as the μTPCs, with suitably-thick polymer layers. At quantities of scale, this property of inkjet printing would limit its utility significantly. Additionally, it was discovered that the viscosity of the dissolved polymer/solvent solution must be kept low to avoid frequent nozzle-clogging. This necessity required patterns to be printed multiple times in order to build up sufficient thickness, resulting in increased effective deposition time. When these factors are considered as a whole, inkjet printing was found to be non-ideal for this application due to its time-consuming nature, despite its other desirable features.

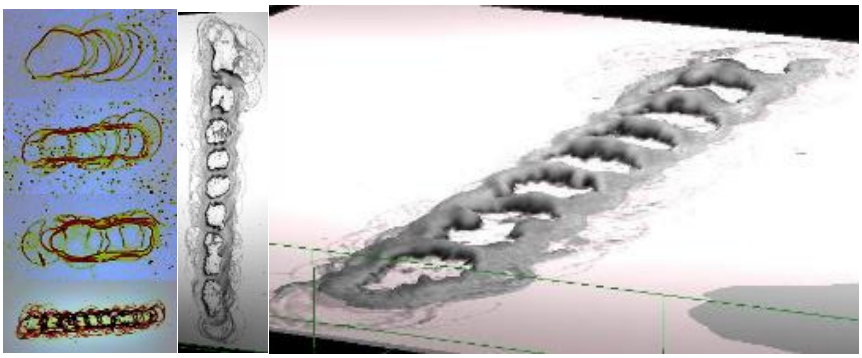

Figure 55 - Optical microscope (left) and enhanced 3D (center, right) images of printed EPCO film exhibiting the coffee ring effect. Printing was performed on a MicroFab JetLab II inkjet printer. Enhanced 3D images were obtained using the LEXT confocal microscope, located in the IEN cleanroom facilities at Georgia Tech.

Spray Coating

As an alternative to inkjet printing, a spray-coating technique was investigated for accomplishing localized sorbent deposition in a more cost-effective, scalable manner. This technique employs the use of a vapor atomizer in conjunction with laser-cut shadow masks (Figure 56) to achieve localized polymer deposition that is capable of coating individual membranes in the μTPC arrays. As with inkjet printing, the sorbent polymer is dissolved in a suitable solvent and the mixture is sprayed out of the nozzle of the atomizer (Figure 57). The shadow mask is placed against the top surface of the die and aligned to the underlying devices. Once aligned, the mask is locked in place with a custom-built fixture (Figure 56) and subsequently placed in the vapor stream from the atomizer until the desired film thickness has been achieved. Sorbent film deposition rate can be controlled by the viscosity of the sorbent/solvent solution, the adjustable aperture of and nitrogen flow through the atomizer, and distance between the aperture and the target. The shadow masks were designed with CAD software (Figure 56) and laser-cut with the Resonetics IR Laser located in the IEN facilities.

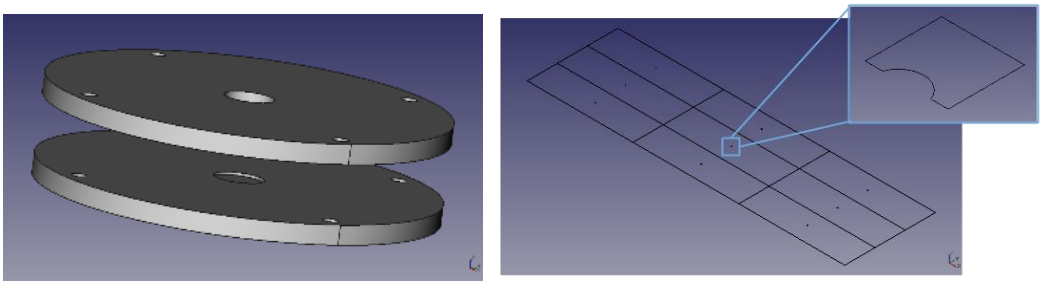

Figure 56 – Design and rendering of (left) fixture for securing shadow masks in place during spray coating and (right) array of individual shadow masks of varying shapes and sizes. The inset on the right shows a magnified image of a single shadow mask designed for use with the integrated chemical sensors.

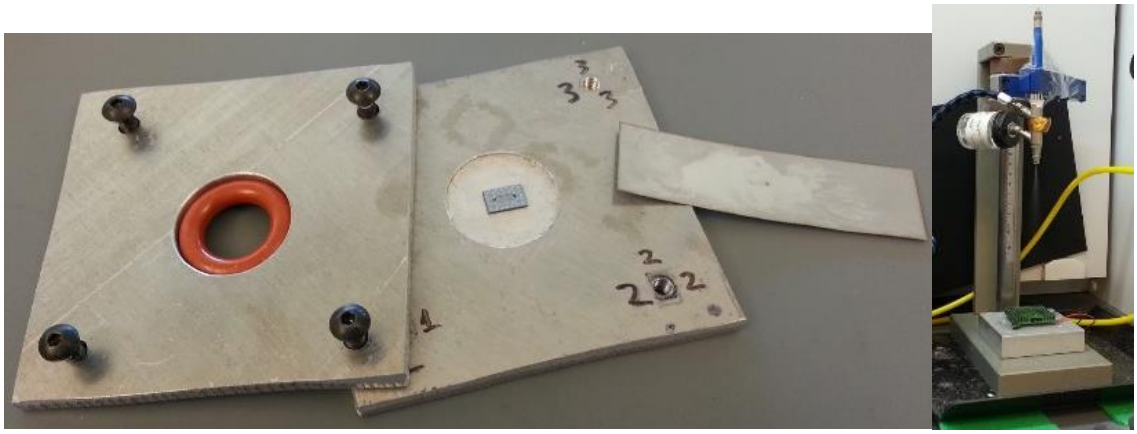

Figure 57 – Photographs of (left) spray-coating fixture machined from steel, with accompanying shadow mask and die to be spray coated, and (right) vapor atomizer used for spray coating.

As demonstrated in Figure 58, the shadow masking technique can even be used to deposit a sorbent layer onto the integrated chemical sensors and prevents polymer deposition in masked areas.

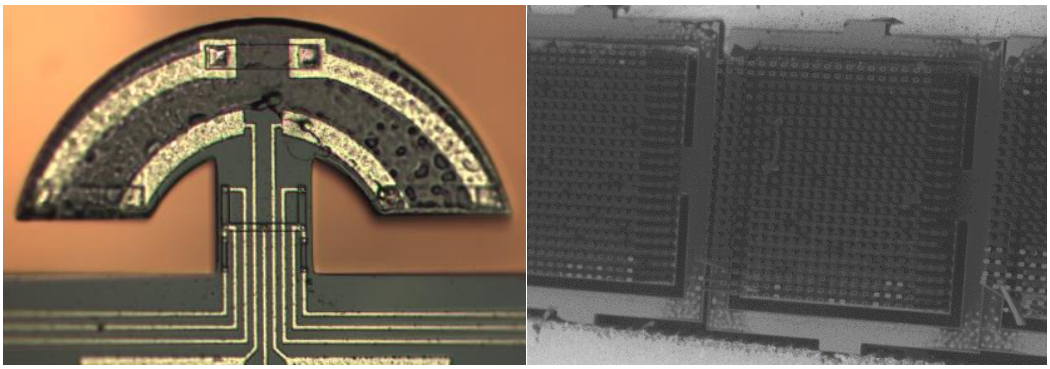

Figure 58 – Photograph of resonator (left) coated with PECH via shadow masking and SEM image of an array (right) of 1 mm x 1 mm µTPC membranes spray-coated with PIB.

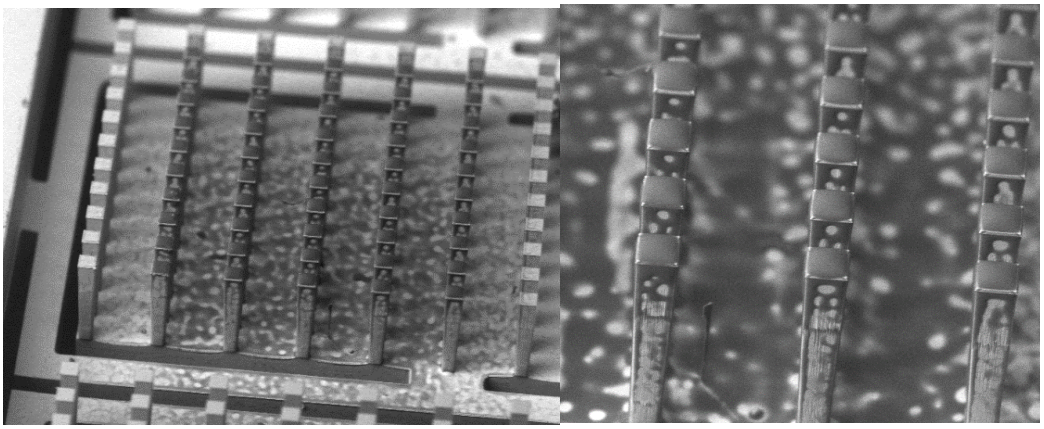

Figure 59 - SEM image of thin PIB coating, which was deposited with a shadow mask onto a suspended 2 mm x 1 mm µTPC membrane. As seen in the figure, the location of the coating can be precisely controlled, allowing sorbent to be deposited only in regions useful for pre-concentration.

The result is a quickly deposited, relatively uniform film that is constrained only to regions useful for pre-concentration and sensing (i.e. the suspended membranes and sensors). Furthermore, the shadow masking approach confers several additional advantages when compared with inkjet printing and drop-coating. One such advantage is flexibility in solvent choice. Since the atomizer is of metallic and glass construction, nearly any solvent used to dissolve polymer-based sorbents now becomes available for use. This not only lowers cost by enabling the use of less expensive solvents, but also expands new possibilities for the deposition of previously unavailable sorbents (due to solvent incompatibility with the ink-jet printer). In short, this improvement is not a difference of

degree but of kind. For example, spray-coating in this way enables devices to be coated with PECH or Tenax TA, which cannot be readily inkjet printed due to the aggressive solvents (e.g. chloroform, dichloromethane) necessary for polymer dissolution. Furthermore, the shadow masking technique can be easily scaled to coat multiple devices at the wafer level, in parallel. When these considerations are taken into account, shadow masking offers significant potential, especially for low-cost applications at scale. With the use of high concentration solutions and multiple coating steps, film thicknesses in excess of 200µm on planar surfaces can be achieved in less than an hour.

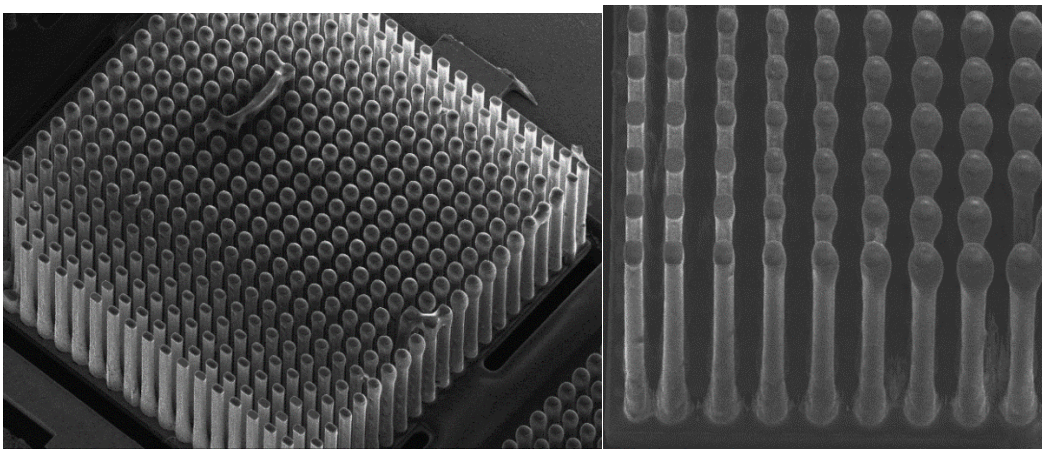

Figure 60 - SEM image of thick (approx. 50 µm) OV-1 sorbent coating deposited by shadow masking onto a suspended 2 mm x 2 mm µTPC membrane. As shown in the image on the right, the location of the coating can be precisely controlled.

For the reasons discussed above, spray coating was chosen as the preferred coating technique due to its simplicity and immediate effectiveness. Future work will revisit the other coating techniques more in depth, and will also explore the possibility of using plasma deposition to deposit uniform polymer films. In the research group of Prof. D. Hess at Georgia Tech, plasma deposition has been used to deposit fluorocarbons [104]. While uniform films result, this technique generally yields highly cross-linked polymer films, which might in their current form not be suitable for TPCs (polymers like PIB are rubbery

and act similar to sponges for VOCs). The use of multi-sorbent films (e.g. DVB/PDMS/Carbowax) and activated carbon particles – such as those used in conventional SPME [24, 50] and other uTPC systems [1, 3, 17, 21, 38] – is suggested as a fruitful investigation for future work. In anticipation of this possibility, several of the µTPC designs implemented wide ridge and pillar spacings that could accommodate relatively large activated carbon granules.

Packaging Concept

With a viable coating technique in place, development shifted to a suitable packaging strategy. As touched on during the mask layout stage, external circuit interface specifications require the chips to be mounted into a 28-pin ceramic DIL package. Furthermore, the packaging design has a significant influence on the pre-concentration factor, as the effective dead volume is directly determined by the packaged chamber and interconnect volumes. With these requirements in mind, a custom packaging approach was designed that minimizes the total dead volume to approximately 10 µL and simultaneously forces the analyte-loaded gas stream through the high surface-area, sorbent-coated regions of the µTPC on the back surface of the suspended membranes (Figure 61). In this case, a uniform coating thickness of 50 µm results in a total sorbent volume of 2.5 µL for an array of the 2 mm x 2 mm devices. With a partition coefficient of 1000x for toluene into PIB, release of the sorbed toluene into a 10 µL chamber volume would result in a pre-concentration factor of 250x. If, however, the chamber volume were 200 µL, the pre-concentration factor would be reduce to only 12.5x which clearly demonstrates the importance of the packaged dead volume. The packaging process has been designed so that

the packaged dies interface seamlessly with both the existing gas testing platform and measurement circuitry, as illustrated in Figure 61.

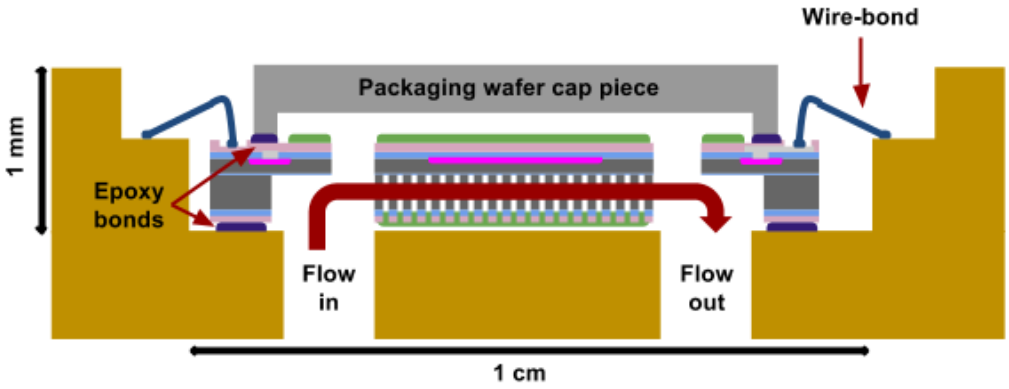

Figure 61 - Profile view of µTPC packaging concept. A silicon capping piece (light gray) diced from a separately-processed packaging wafer is bonded to a µTPC die (dark gray) with epoxy. The bottom surface of the µTPC die is bonded with epoxy to the ceramic DIL package (gold) with the inlet/outlet ports on the die aligned to the laser-cut vias on the ceramic DIL package. The packaging results in a dead volume of approximately 10µL and is designed to be gas-tight with chamber walls that are inert with respect to VOC sorption.

Packaging Wafer Design

In anticipation of the final packaging requirements, a packaging wafer mask set was designed during the mask layout stage. The packaging wafer process sequence requires two additional photomasks and was designed to allow the front surface of the µTPC arrays to be capped and sealed with an inert, gas-tight, low-volume chamber.

To accomplish this, each die on the packaging wafer consists of a raised silicon ring that encircles the µTPC array on the corresponding device wafer (Figure 62), while maintaining access to the wire-bonding pads around the perimeter of the die. Due to the necessary tolerances associated with bonding the capping piece, the introduction of additional setbacks between the ring, µTPC array, and wire-bond pads were required.

Ultimately, this design choice, in conjunction with the limit to maximum die size, introduced the most significant constraints on the footprints for the µTPC arrays.

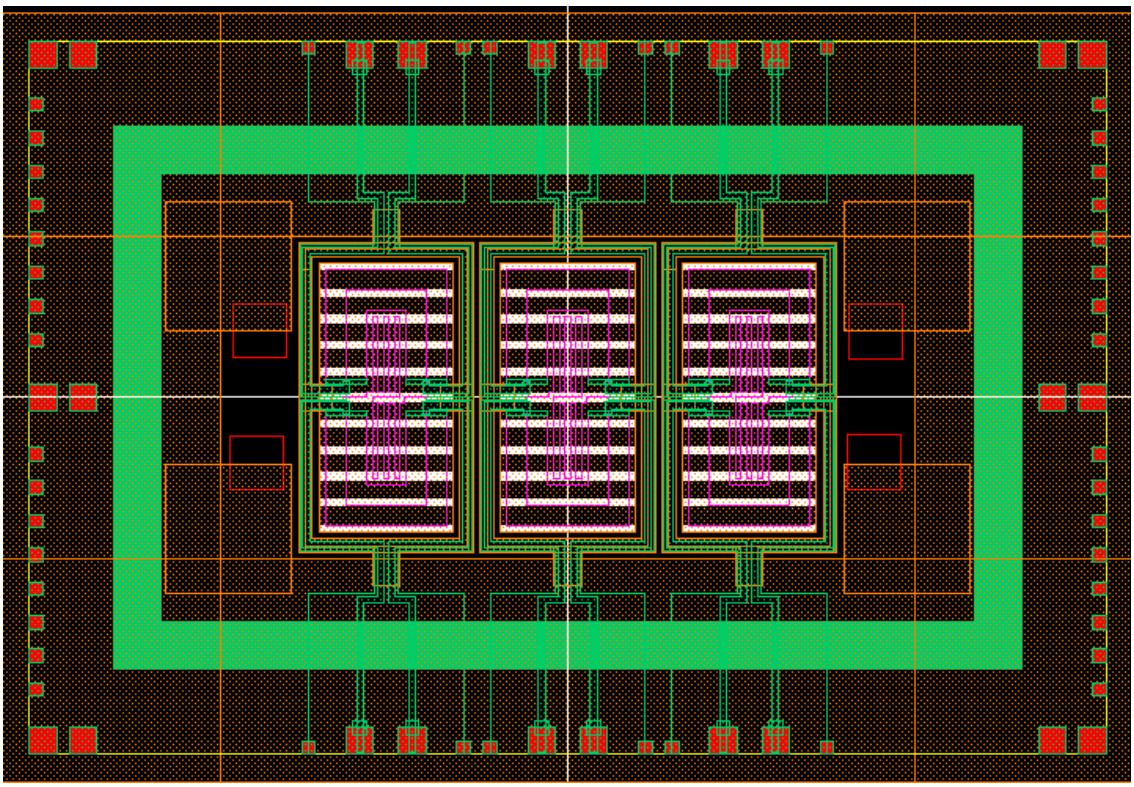

Figure 62 - Detail from mask layout for 2 mm x 1 mm µTPC die, showing placement of the packaging wafer die onto the µTPC die. The green ring surrounding the µTPC array represents the raised silicon ridge on the packaging wafer capping piece.

The full fabrication sequence of the packaging wafer requires three mask steps (Figure 63), and represents new process development. Processing begins with the deposition and patterning of a thin metal layer onto a bare silicon wafer. The patterning of the metal layer re-uses Mask 3 from the SOI process flow, and is used only to aid in alignment of the packaging die (i.e. not for electrical connections) to the device wafer. Next, several microns of dielectric are deposited and patterned on the front surface of the wafer for use as a DRIE hard mask. The wafer is then etched *via* DRIE partially through its bulk thickness, but stops short of reaching the back surface. At this point, additional dielectric layers are deposited onto the back surface and patterned to serve as a DRIE hard

mask for forming the raised silicon rings. A final DRIE etch from the back surface creates the raised ring structures, and the completed wafer is ready for bonding to the device wafer. The etched through-holes from the front surface are used as windows to see through to the device wafer below during alignment. With the full 3-mask processing sequence, the packaging wafer is capable of being aligned to the underlying device layer and bonded at the wafer level (i.e., all die bonded simultaneously), which lends itself to large-scale manufacturing.

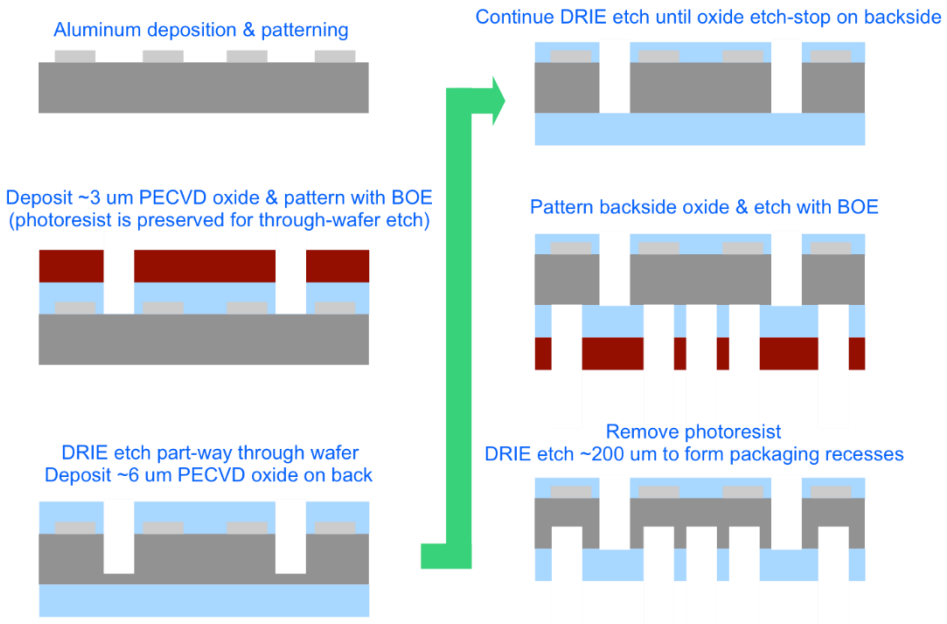

Figure 63 - Process flow diagram showing full fabrication sequence for µTPC packaging wafer. If the capping pieces are to be bonded individually by hand, the process sequence can be simplified to a single mask step where DRIE of silicon is used to form the raised silicon rings.

If individual die are required to be bonded separately, however, the processing sequence can be simplified to just a single mask step with a DRIE etch to form the raised circular rings. This approach is more suitable for rapid prototyping and proof-of-concept work, and is the method employed in the presented packaging results. Figure 64 shows photographs of several diced capping die from a completed packaging wafer, and an

individual capping die that has been bonded to a glass slide with epoxy placed on top of the raised ring structure.

Figure 64 - Photographs of several diced die (left) from completed packaging wafer, and single die bonded to glass slide with epoxy (right). To seal the top surface of the µTPC die, epoxy is applied to the raised silicon ring of a capping die, which is subsequently bonded to the µTPC die.

Laser Cutting

While the silicon capping pieces produced by the packaging wafer serve to seal the µTPC chamber from the top, the chamber must also be sealed from the back surface. To achieve this goal, fluidic vias were laser-cut directly into the ceramic DIL package as shown in Figure 65.

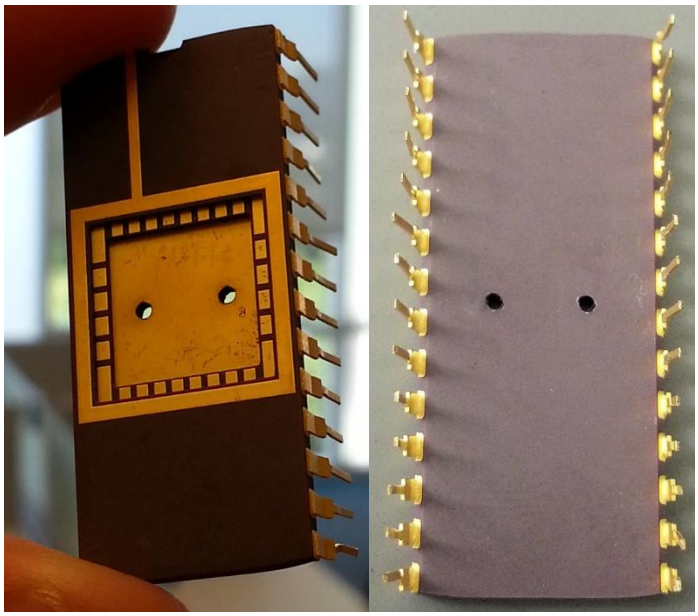

Figure 65 - Views from the top surface (left) and bottom surface (right) of ceramic DIL package, which has been laser-cut in preparation for packaging of a µTPC die. The laser-cut vias are designed to align with the inlet and outlet ports on the µTPC die.

The vias were arranged so that they are located directly beneath the inlet and outlet ports on the µTPC die. In this way, the µTPC chip – already sealed from the top with the silicon capping piece – can be directly bonded to the gold surface of the ceramic DIL package and the vias act as extensions of the on-chip inlet and outlet ports. Figure 66 is a photograph of a completely packaged device.

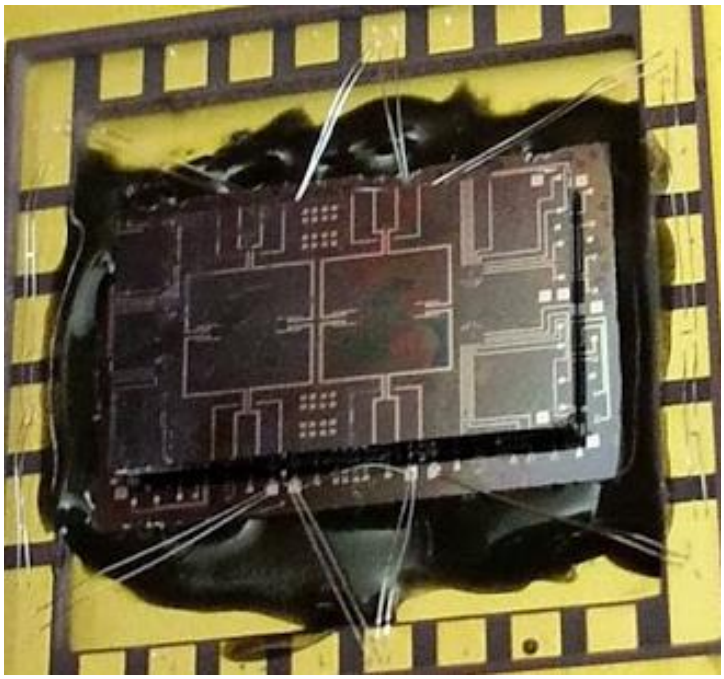

Figure 66 - Photograph of fully-packaged µTPC die, which has been placed over the laser-cut vias and bonded with epoxy on the bottom surface. The top surface of the die has been sealed by bonding a silicon capping piece with epoxy. As can be seen from the figure, the packaging has been designed to allow wire-bonding between the die and package.

When applying the epoxy during bonding, care was taken to ensure that minimal epoxy enters the inside of the µTPC chamber, as illustrated in Figure 64. In this way, the chamber walls exposed to gas samples are essentially composed of inert materials (e.g. silicon, gold, ceramic) and should not contribute significantly to sorption of VOC concentrations during measurement.

Furthermore, it is assumed that the partition coefficient of the epoxy is orders of magnitude less than the partition coefficients of the sorbent coatings, which minimizes the risk of unwanted sorption even further. However, the partition coefficient for the epoxy has not yet been verified by experiment, but is suggested for future work. If the epoxy is found to interfere with µTPC sorption, the use of alternative epoxies based on inert materials (e.g. ceramics, PTFE) can be explored. Following packaging, the entire fluidic

pathway was tested for leaks and was found to be gas-tight for both nitrogen and air flows of up to 100 ml/min.

CHAPTER 6 – CHEMICAL MEASUREMENTS

With packaging complete, the devices were ready to interface with the existing gas flow system (Figure 67) for initial evaluation of chemical performance. Measurements commenced with testing of the integrated chemical sensors, which were controlled by an amplifying feedback loop and exposed alternately to pure nitrogen carrier gas and defined concentrations of VOCs in the custom gas set-up.

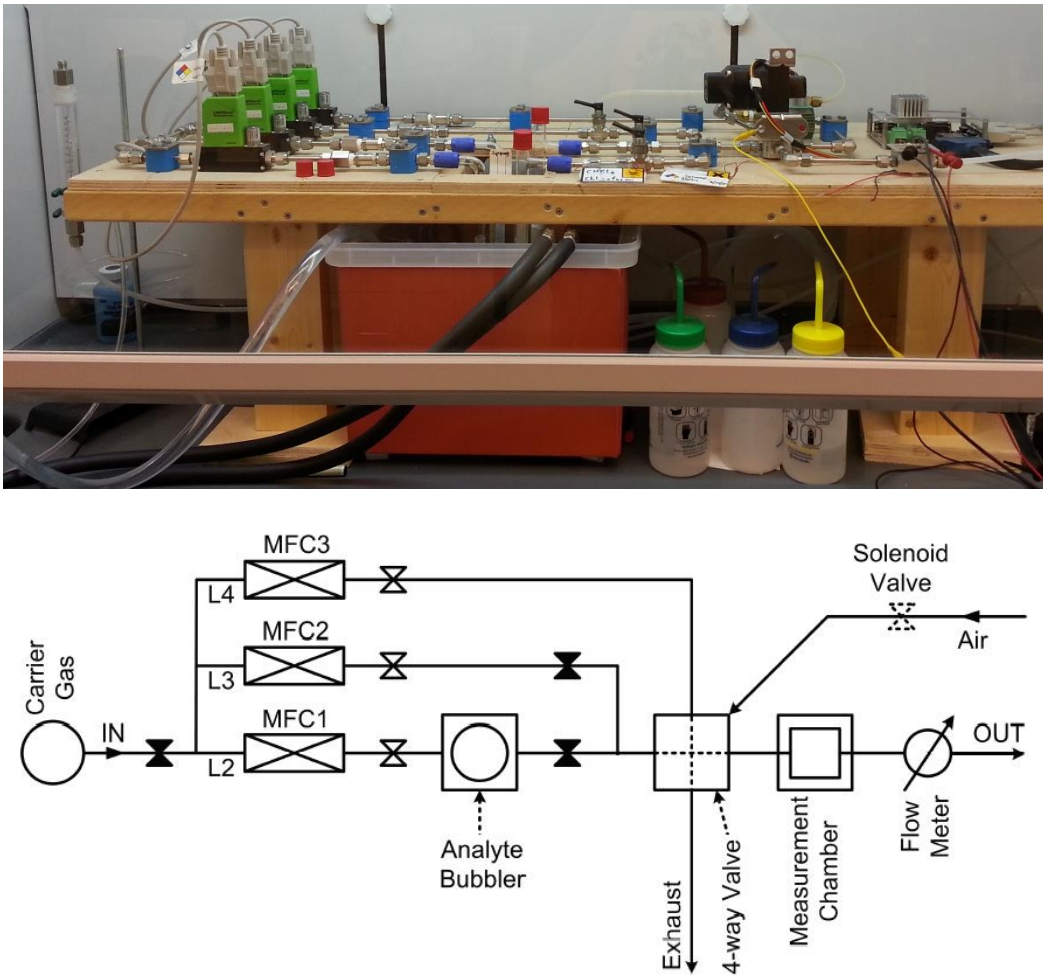

Figure 67 - Photograph (top) and schematic diagram (bottom) of custom gas setup. Flow rates are controlled by precision mass flow controllers (MFCs) and known VOC concentrations are generated by flowing carrier gas through a temperature-controlled bubbler and diluting with carrier gas. A pneumatic 4-way valve enables rapid switching between reference carrier and analyte gas streams.

Integrated Sensor Performance

As an example, Figure 68 shows the frequency response of a PECH-coated resonator to different concentrations of toluene. The data were collected at a constant temperature of 20 ºC and a flow rate of 80 ml/min through the measurement chamber. Between successive exposures to the analyte-loaded gas stream, the gas flow over the resonator is changed to pure nitrogen carrier gas. A four-way valve enables fast switching and allows the investigation of signal transients [74, 89]. From the baseline frequency data, a short-term frequency stability of 3×10^{-8} was extracted using the Allan variance method.

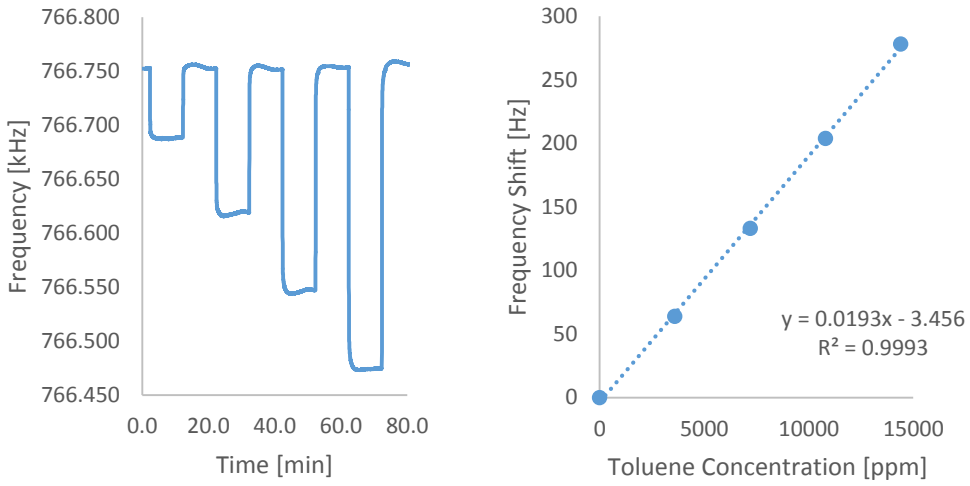

Figure 68 - Experimentally observed frequency shift of PECH-coated resonator as a function of time (left); the microsensor is subsequently exposed to different toluene concentrations (3600-7200-10800-14400 ppm). Between successive toluene exposures, the chamber is flushed with nitrogen as carrier gas. The response of the sensor with respect to toluene concentration is reversible and very linear (right).

An analysis of the measured frequency data reveals that the sensors exhibit a linear response with respect to toluene concentration (Figure 68, right). Using the observed chemical sensitivity of 0.019 Hz/ppm for toluene and the Allan variance of 3×10^{-8}, limits of detection below 5 ppm for toluene can be expected for this device. However, these LoD values need to be confirmed by measurements at ppm-level analyte concentrations.

Another important observation from the gas measurement data is that the sensor's response is fully reversible with time constants well below 1 minute even for relatively thick polymer films.

Pre-Concentration Measurement

With suitable operation of the integrated chemical sensors confirmed, chemical testing shifted toward observation of the pre-concentration effect. In order to highlight the novel design of the µTPC – which allows for measurements to take place in a static, non-flowing environment – an experimental setup was constructed which was capable of trapping a fixed volume of sample gas inside the µTPC chamber. This setup consisted of utilizing the custom gas flow setup to flow a known concentration of analyte over the µTPC until the analyte concentration in the sorbent was in equilibrium with the analyte concentration in the environment. Once at equilibrium, the inlet/outlet ports to the µTPC were quickly sealed with a mechanical clamp (Figure 69). Initial experiments were carried out with a µTPC chip that had been mounted into a ceramic DIL package, but not bonded to the package with epoxy. The µTPC die was not sealed from the top surface with a capping piece, but was sealed into a larger chamber with the use of a second ceramic DIL package (containing an array of chemical sensors) and a thin nitrile gasket (Figure 69).

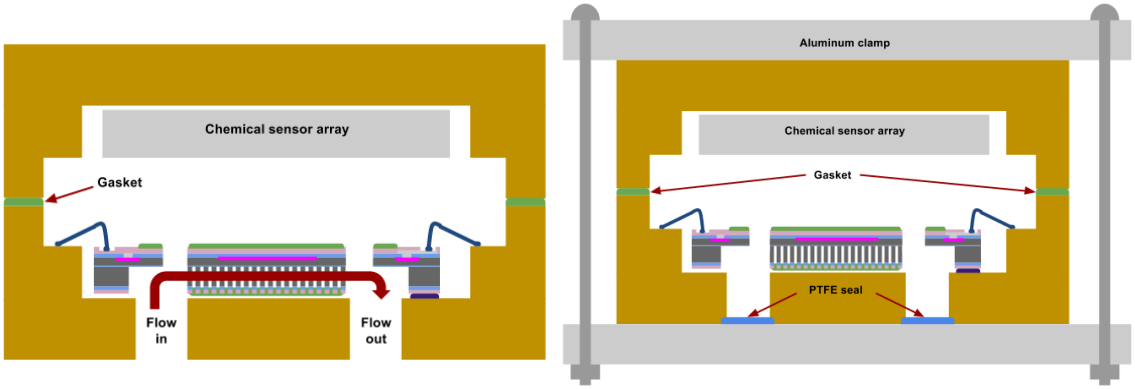

Figure 69 - Experimental test setup for measuring pre-concentration factor. The µTPC and chemical sensors are first exposed (left) to a constant toluene concentration until equilibrium is reached. Once in equilibrium, the inlet/outlet ports to the chamber are quickly sealed (right) with a mechanical clamp, trapping a fixed volume of toluene inside the chamber. Applying heating power to the µTPC during thermal desorption drives sorbed analyte molecules out of the µTPC sorbent, which raises the ambient toluene concentration inside the chamber. Analyte uptake into the chemical sensors then increases due to the increased ambient concentration.

The experiment was performed by first exposing a µTPC and chemical sensors coated with PEUT to a constant 5000 ppm concentration of toluene until equilibrium was reached. Once in equilibrium, the inlet/outlet ports into the chamber were quickly sealed with a mechanical clamp, trapping a fixed volume of gas inside the chamber. Due to the condition prior to clamping, all sorption into the sorbent layers on both the chemical sensors and the µTPC was presumed to be in equilibrium with the analyte concentration in the gas phase. Once the chamber was sealed, application of heating power to the µTPC drives sorbed analyte molecules out of the µTPC sorbent (i.e. thermal desorption), which raises the analyte concentration inside the chamber. Analyte uptake into the chemical sensors then increased due to the increased ambient concentration. After several seconds, the entire package heats up (due to the power generated in the µTPC), which begins to reduce the temperature-dependent sorption capacity of the sorbent layer on the chemical sensors. At this point, sorbed analyte desorbs from the chemical sensor and a new equilibrium (based on the elevated temperature) is established inside the chamber.

By first performing an initial control experiment – where only pure N_2 (i.e. no analyte) is introduced into the chamber – the response of the system to temperature alone can be recorded. This response is then subtracted from the total response due to both temperature and analyte effects (Figure 70), resulting in a plot of the system's response to analyte only. As can be seen from the figure, the aggregate sensor response shows the sensor shifting in frequency due to the increased mass uptake – as if it had been exposed to a higher gas concentration than that which was originally introduced into the chamber.

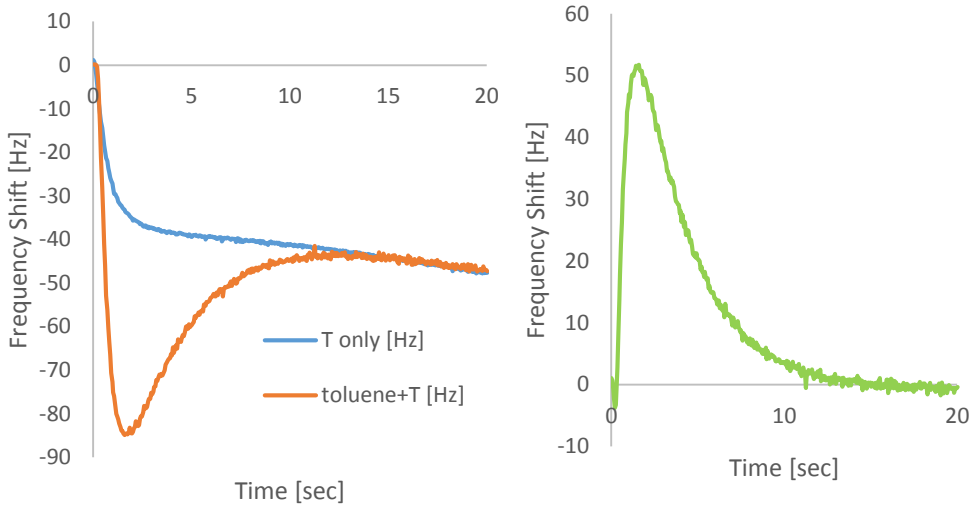

Figure 70 - Experimentally observed pre-concentration factor. The plot (left) shows a comparison between the sensor signal when the µTPC is exposed to N_2 only (blue) vs. 5000 ppm of toluene (orange). The plot (right) shows the aggregate response, where temperature effects have been removed leaving only the response to toluene. The response of the sensor alone (i.e. without the µTPC connected) was approximately 100 Hz when exposed to 5000 ppm of toluene; thus, an additional increase of 50 Hz due to pre-concentration has boosted the signal by 50%. Thermal desorption was performed by applying 100mW of heating power to the µTPC for 30 sec.

While significant as a proof-of-concept demonstration, the observed PC factor of 50% is considerably lower than expected. This is almost certainly a result of the large dead volumes introduced by interfacing with the cantilever-based sensors on a separate DIL package. In the experimental setup used to collect these data, the total dead volume inside of the sealed chamber is approximately 200 µL, nearly twenty times larger than the 10 µL

volume possible with the more sophisticated packaging detailed in Chapter 5. As the increased ambient concentration experienced by the chemical sensor during thermal desorption is a function of the volume into which the sorbed molecules are released, reducing the dead volume is critical. Thus, the pre-concentration factor is expected to increase to at least 20 with use of the improved packaging. Furthermore, the experiment described above involved pre-concentration of a relatively high-concentration sample, where the chemical sensor might be saturated prior to thermal desorption. The μTPC system, however, was designed for optimal operation of very low-concentration samples (e.g. ppb), and it is expected that the pre-concentration factor will increase further when the capability of testing at these concentration levels is available. Future work will involve installing a calibrated gas permeation tube delivery system capable of reaching these low concentrations.

CHAPTER 7 – OUTLOOK & FUTURE WORK

In summary, the development of a MEMS-based micro thermal pre-concentration (μTPC) system for enhanced detection of volatile organic compounds (VOCs) in the gas phase has been demonstrated. The novel system features integrated chemical sensing technology, and can be used to improve the performance of previously developed cantilever-based resonant micro-sensors by temporarily increasing the effective concentration seen by the sensors. The system features arrays of suspended, thermally-isolated μTPC devices and offers the potential for coarse pre-filtering of complex gas mixtures. Experimental measurements confirm that even the largest hotplates (2 mm x 2 mm) can be heated to 200˚C with less than 500mW of heating power, and exhibit thermal time constants below 1 second. Additionally, the design of the system enables novel modes of operation without the need of an external fluidic system, with initial tests of the system demonstrating a pre-concentration factor of 50% for toluene in a static, no-flow setup.

While significant milestones have already been achieved, this endeavor is a multi-generational one, which will require several years to reach full maturity. Future work will focus on increasing the pre-concentration factor of the system through various means. For example, improved techniques for the localized deposition of sorbent materials will be investigated, with an emphasis on utilizing plasma-deposited and activated carbon-based sorbents. The implementation of multi-layer sorbents comprised of several different sorbent types may also prove fruitful in this regard. The viability of the drop-casting technique may be improved by exploring the possibility of different solvent systems and surface modifications that could render the device surface more amenable to wetting. Also,

the effect of sorbent coating thickness on device performance can be explored and optimized.

In addition to sorbent layer improvements, the packaging design must also be enhanced. For example, it became clear during the thermal evaluation of the devices that there was evidence of the package itself heating up more than expected. To mitigate this undesirable effect, a heatsink could be coupled to the ceramic package with thermally conductive paste, or active cooling could be employed to ensure the ceramic package stays at a more stable temperature during measurement. Additionally, it is yet unclear if the bonding epoxy is sufficiently inert to the sorption of VOCs. If this epoxy proves unsuitable, other epoxies based on ceramic or PTFE chemistries could be employed as more inert alternatives. If even these epoxies do not render the μTPC chamber sufficiently inert, it could even be possible to coat the walls of the chamber with parylene. Deposition of parylene over the sorbent-coated membrane surfaces could be prevented by heating the μTPC membranes during parylene coating, as parylene deposition is inhibited onto hot surfaces. Such a technique holds substantial possibility for increasing the pre-concentration factor by truly rendering all other surfaces inside the chamber inert.

Perhaps the richest area for improvement is in the testing setup. While it was important to first demonstrate the system's novel measurement capabilities in a static, no-flow arrangement, all other μTPCs encountered in the literature utilized some sort of flow system with zero dead-volume valves that allowed for sharp injection into a GC column or measurement chamber. Such an approach could be explored with this system as well, along with an investigation of optimal flow rates, desorption heating powers, and heating durations. The effect of more sophisticated heating patterns could also improve system

performance, in both a static, no-flow arrangement as well as a forced-flow setup. Low-cost, low-power microcontrollers in a feedback arrangement could generate the desired heating patterns, and could even improve the total system's portability, allowing automatic operation on mobile platforms for extended periods of time. Such microcontrollers could further be used to remove temperature effects in real-time by comparing the output of a sensor to that of an uncoated, reference device. This type of support circuitry would be necessary to fully realize the system's capability of operating in real-time with all four integrated sensors.

In addition to circuit improvements, challenging the system with much lower analyte concentrations is also likely to improve performance, as the integrated sensors will be able to operate far away from their saturation points. To accomplish this, however, will require significant modification to the existing gas flow setup and will likely require the installation and calibration of a gas permeation tube delivery system for generating such low concentrations in a reliable and consistent manner. Clearly, much work remains for the system demonstrated here to reach its full potential, but the possibilities are very exciting.

APPENDIX A – SUPREME SIMULATION CODE

```
*SUPREM OUTPUT FILE*
      ************************************************************
      ***                      TSUPREM-4 (TM)                  ***
      ***      Version D-2010.03-0, System K (AMD64: Linux)    ***
      ***                Copyright (C) 1988-2007               ***
      ***                      Synopsys, Inc.                  ***
      ***                                                      ***
      ***  This software and the associated documentation are  ***
      ***  confidential and proprietary to Synopsys, Inc.  Your ***
      ***  use or disclosure of this software is subject to the ***
      ***  terms and conditions of a written license agreement ***
      ***  between you, or your company, and Synopsys, Inc.    ***
      ***                                                      ***
      ***              Compiled: February 09, 2010             ***
      ***       TSUPREM-4 is a trademark of Synopsys, Inc.     ***
      ************************************************************

                            17-Mar-2015 16:35:01
 Entering source file modifiedStanfordDoping.sup.
assign name=plength n.val=0.01
assign name=pwidth n.val=0.005
# Establish the mesh
# Use default X spacing for 1-D
# Specify a finer mesh in the Y-direction for more accuracy
line y loc=0.0 spacing=0.01 tag=top
line y loc=10.0 spacing=0.10 tag=bottom

# initialize the silicon
initialize <100> impurity=phosphorus i.resistivity=10
** Automatic X grid generation:  lines at X=0 and X=1 micron.
   2 lines in the x direction.
   256 lines in the y direction.
# make plots on the screen (instead of postscript file)
```

```
option device=X
# use detailed oxidation model
method vertical pd.full
##

# Processing
# perform a pre dep diffusion
diffusion time=40 temperature=930 boron=3.82e20
diffusion continue time=90 temperature=930 t.final=600
select z=boron title="Predep Boron"
plot.1d x.val=0
pause
# plot the results of the predepimplant
select z=log10(abs(doping)) title="Doping Profile, before and after drive-in"
plot.1d x.val=0 y.min=13 y.max=21 x.min=-0.2 x.max=2.0

# drive-in
diffusion time= 60 temperature= 600 t.final=950 inert
diffusion continue  time= 5 dryo2
diffusion continue time=30 weto2
diffusion continue time=30 t.final=1000 inert
diffusion continue time=30 dryo2
diffusion continue time=20 inert
diffusion continue time=100 t.final=600

# plot results after the anneal
select z=log10(abs(doping))
plot.1d x.val=0 color=2 ^axes ^clear

#Annealing Metal in Lindberg Furnace
diffusion time=40 temperature=30 t.final=350 inert

*** Warning:  Temperature (30 C) is below 400 degrees; impurity diffusion may
***           be inaccurate and program may have numerical difficulties.

diffusion continue time=33 t.final=450 inert
```

```
diffusion continue temperature = 450 time=150 inert

diffusion continue time=120 t.final=33 inert

select z=log10(abs(doping))

plot.1d x.val=0 color=3 ^axes ^clear

# print the results

select z=doping

print.1d x.val=0 layers

 Num      Material       Top     Bottom  Thickness        Integral

   1         oxide   -0.0895     0.0687     0.1582     -2.3372e+14

   2       silicon    0.0687     1.2972     1.2285     -2.7373e+14

   3       silicon    1.2972    10.0000     8.7028      3.9028e+11

select z=doping

extract silicon x.val=0 value=0 d.extrac assign name=Dj

  Extracted result:  1.22849

electric x.val=0

******************** STRUCTURE INFORMATION **********************

LAYER    MATERIAL THICKNESS REGION DIFTYP THICKNESS       TOP    BOTTOM

    2       oxide    0.1582                  0.1582   -0.0895    0.0687

    1     silicon    9.9313      2      p    1.2083    0.0687    1.2770

                                  1      n    8.7013    1.2987   10.0000

*****************************************************************

 Bias step   1:    0.00 (Volts)

     ****************************************************************

       Material    Thickness   Type   Junction Depth   Sheet Resistance

     ----------------------------------------------------------------

          oxide      1580 A

        silicon      9.93 um     P           1.23 um       248   ohm/sq

                                 N           9.93 um      13.8 K ohm/sq

     ****************************************************************

 Exiting source file modifiedStanfordDoping.sup.

 *** END TSUPREM-4 ***
```

APPENDIX B – COMSOL SIMULATION CODE EXAMPLE

```
function out = model
%
% MT_1mmx1mmx20um_100umLegs_Ridges_h15_p500mW.m
%
% Model exported on Jun 20 2015, 18:42 by COMSOL 4.4.0.195.

import com.comsol.model.*
import com.comsol.model.util.*

model = ModelUtil.create('Model');

model.modelPath('C:\Users\cantilever\Desktop\MT_COMSOL\CodeModels');

model.modelNode.create('mod1');

model.geom.create('geom1', 3);
model.geom('geom1').feature.create('BLK1', 'Block');
model.geom('geom1').feature.create('BLK10', 'Block');
model.geom('geom1').feature.create('BLK11', 'Block');
model.geom('geom1').feature.create('BLK12', 'Block');
model.geom('geom1').feature.create('BLK13', 'Block');
model.geom('geom1').feature.create('BLK14', 'Block');
model.geom('geom1').feature.create('BLK15', 'Block');
model.geom('geom1').feature.create('BLK16', 'Block');
model.geom('geom1').feature.create('BLK17', 'Block');
model.geom('geom1').feature.create('BLK18', 'Block');
model.geom('geom1').feature.create('BLK19', 'Block');
model.geom('geom1').feature.create('BLK2', 'Block');
model.geom('geom1').feature.create('BLK20', 'Block');
model.geom('geom1').feature.create('BLK21', 'Block');
model.geom('geom1').feature.create('BLK22', 'Block');
model.geom('geom1').feature.create('BLK23', 'Block');
model.geom('geom1').feature.create('BLK24', 'Block');
model.geom('geom1').feature.create('BLK25', 'Block');
model.geom('geom1').feature.create('BLK26', 'Block');
model.geom('geom1').feature.create('BLK27', 'Block');
model.geom('geom1').feature.create('BLK28', 'Block');
model.geom('geom1').feature.create('BLK29', 'Block');
model.geom('geom1').feature.create('BLK3', 'Block');
model.geom('geom1').feature.create('BLK30', 'Block');
model.geom('geom1').feature.create('BLK31', 'Block');
model.geom('geom1').feature.create('BLK32', 'Block');
model.geom('geom1').feature.create('BLK33', 'Block');
model.geom('geom1').feature.create('BLK34', 'Block');
model.geom('geom1').feature.create('BLK35', 'Block');
model.geom('geom1').feature.create('BLK36', 'Block');
model.geom('geom1').feature.create('BLK4', 'Block');
model.geom('geom1').feature.create('BLK5', 'Block');
model.geom('geom1').feature.create('BLK6', 'Block');
model.geom('geom1').feature.create('BLK7', 'Block');
model.geom('geom1').feature.create('BLK8', 'Block');
model.geom('geom1').feature.create('BLK9', 'Block');
model.geom('geom1').feature('BLK1').set('axis', {'0' '0' '1'});
model.geom('geom1').feature('BLK1').set('size', {'4.0E-4' '9.0E-4' '2.0E-6'});
model.geom('geom1').feature('BLK1').set('pos', '-4.5E-4,-4.5E-4,-2.0E-6');
model.geom('geom1').feature('BLK10').set('axis', {'0' '0' '1'});
model.geom('geom1').feature('BLK10').set('size', {'2.0E-5' '0.0010' '2.0E-4'});
model.geom('geom1').feature('BLK10').set('pos', '-4.2E-4,-5.0E-4,0.0');
model.geom('geom1').feature('BLK11').set('axis', {'0' '0' '1'});
model.geom('geom1').feature('BLK11').set('size', {'4.0E-4' '9.0E-4' '2.0E-6'});
model.geom('geom1').feature('BLK11').set('pos', '5.0E-5,-4.5E-4,-2.0E-6');
model.geom('geom1').feature('BLK12').set('axis', {'0' '0' '1'});
model.geom('geom1').feature('BLK12').set('size', {'0.0012' '1.0E-4' '2.0E-5'});
model.geom('geom1').feature('BLK12').set('pos', '-6.0E-4,6.0E-4,-2.0E-5');
model.geom('geom1').feature('BLK13').set('axis', {'0' '0' '1'});
model.geom('geom1').feature('BLK13').set('size', {'0.0012' '1.0E-4' '2.0E-5'});
```

```
model.geom('geom1').feature('BLK13').set('pos', '-6.0E-4,-7.0E-4,-2.0E-5');
model.geom('geom1').feature('BLK14').set('axis', {'0' '0' '1'});
model.geom('geom1').feature('BLK14').set('size', {'2.0E-5' '0.0010' '2.0E-4'});
model.geom('geom1').feature('BLK14').set('pos', '-3.8E-4,-5.0E-4,0.0');
model.geom('geom1').feature('BLK15').set('axis', {'0' '0' '1'});
model.geom('geom1').feature('BLK15').set('size', {'2.0E-5' '0.0010' '2.0E-4'});
model.geom('geom1').feature('BLK15').set('pos', '-3.4E-4,-5.0E-4,0.0');
model.geom('geom1').feature('BLK16').set('axis', {'0' '0' '1'});
model.geom('geom1').feature('BLK16').set('size', {'0.0010' '0.0010' '2.0E-5'});
model.geom('geom1').feature('BLK16').set('pos', '-5.0E-4,-5.0E-4,-2.0E-5');
model.geom('geom1').feature('BLK17').set('axis', {'0' '0' '1'});
model.geom('geom1').feature('BLK17').set('size', {'2.0E-5' '0.0010' '2.0E-4'});
model.geom('geom1').feature('BLK17').set('pos', '-3.0000000000000003E-4,-5.0E-4,0.0');
model.geom('geom1').feature('BLK18').set('axis', {'0' '0' '1'});
model.geom('geom1').feature('BLK18').set('size', {'2.0E-5' '0.0010' '2.0E-4'});
model.geom('geom1').feature('BLK18').set('pos', '-2.6000000000000003E-4,-5.0E-4,0.0');
model.geom('geom1').feature('BLK19').set('axis', {'0' '0' '1'});
model.geom('geom1').feature('BLK19').set('size', {'2.0E-5' '0.0010' '2.0E-4'});
model.geom('geom1').feature('BLK19').set('pos', '-2.2E-4,-5.0E-4,0.0');
model.geom('geom1').feature('BLK2').set('axis', {'0' '0' '1'});
model.geom('geom1').feature('BLK2').set('size', {'2.0E-5' '0.0010' '2.0E-4'});
model.geom('geom1').feature('BLK2').set('pos', '-1.8E-4,-5.0E-4,0.0');
model.geom('geom1').feature('BLK20').set('axis', {'0' '0' '1'});
model.geom('geom1').feature('BLK20').set('size', {'2.0E-5' '0.0010' '2.0E-4'});
model.geom('geom1').feature('BLK20').set('pos', '-1.4000000000000001E-4,-5.0E-4,0.0');
model.geom('geom1').feature('BLK21').set('axis', {'0' '0' '1'});
model.geom('geom1').feature('BLK21').set('size', {'1.0E-4' '0.0014' '2.0E-5'});
model.geom('geom1').feature('BLK21').set('pos', '-6.999999999999999E-4,-7.0E-4,-2.0E-5');
model.geom('geom1').feature('BLK22').set('axis', {'0' '0' '1'});
model.geom('geom1').feature('BLK22').set('size', {'2.0E-4' '1.0E-4' '2.0E-5'});
model.geom('geom1').feature('BLK22').set('pos', '-1.0E-4,5.0E-4,-2.0E-5');
model.geom('geom1').feature('BLK23').set('axis', {'0' '0' '1'});
model.geom('geom1').feature('BLK23').set('size', {'2.0E-4' '1.0E-4' '2.0E-5'});
model.geom('geom1').feature('BLK23').set('pos', '-1.0E-4,-5.999999999999998E-4,-2.0E-5');
model.geom('geom1').feature('BLK24').set('axis', {'0' '0' '1'});
model.geom('geom1').feature('BLK24').set('size', {'2.0E-5' '0.0010' '2.0E-4'});
model.geom('geom1').feature('BLK24').set('pos', '-1.0000000000000002E-4,-5.0E-4,0.0');
model.geom('geom1').feature('BLK25').set('axis', {'0' '0' '1'});
model.geom('geom1').feature('BLK25').set('size', {'1.0E-4' '2.0E-4' '2.0E-5'});
model.geom('geom1').feature('BLK25').set('pos', '-8.000000000000001E-4,-1.0E-4,-2.0E-5');
model.geom('geom1').feature('BLK26').set('axis', {'0' '0' '1'});
model.geom('geom1').feature('BLK26').set('size', {'2.0E-5' '0.0010' '2.0E-4'});
model.geom('geom1').feature('BLK26').set('pos', '-6.000000000000002E-5,-5.0E-4,0.0');
model.geom('geom1').feature('BLK27').set('axis', {'0' '0' '1'});
model.geom('geom1').feature('BLK27').set('size', {'1.0E-4' '2.0E-4' '2.0E-5'});
model.geom('geom1').feature('BLK27').set('pos', '7.000000000000001E-4,-1.0E-4,-2.0E-5');
model.geom('geom1').feature('BLK28').set('axis', {'0' '0' '1'});
model.geom('geom1').feature('BLK28').set('size', {'2.0E-5' '0.0010' '2.0E-4'});
model.geom('geom1').feature('BLK28').set('pos', '-1.9999999999999998E-5,-5.0E-4,0.0');
model.geom('geom1').feature('BLK29').set('axis', {'0' '0' '1'});
model.geom('geom1').feature('BLK29').set('size', {'1.0E-4' '0.0014' '2.0E-5'});
model.geom('geom1').feature('BLK29').set('pos', '6.000000000000001E-4,-7.0E-4,-2.0E-5');
model.geom('geom1').feature('BLK3').set('axis', {'0' '0' '1'});
model.geom('geom1').feature('BLK3').set('size', {'2.0E-5' '0.0010' '2.0E-4'});
model.geom('geom1').feature('BLK3').set('pos', '1.9999999999999998E-5,-5.0E-4,0.0');
model.geom('geom1').feature('BLK30').set('axis', {'0' '0' '1'});
model.geom('geom1').feature('BLK30').set('size', {'2.0E-5' '0.0010' '2.0E-4'});
model.geom('geom1').feature('BLK30').set('pos', '5.9999999999999995E-5,-5.0E-4,0.0');
model.geom('geom1').feature('BLK31').set('axis', {'0' '0' '1'});
model.geom('geom1').feature('BLK31').set('size', {'2.0E-5' '0.0010' '2.0E-4'});
model.geom('geom1').feature('BLK31').set('pos', '9.999999999999999E-5,-5.0E-4,0.0');
model.geom('geom1').feature('BLK32').set('axis', {'0' '0' '1'});
model.geom('geom1').feature('BLK32').set('size', {'2.0E-5' '0.0010' '2.0E-4'});
model.geom('geom1').feature('BLK32').set('pos', '1.4E-4,-5.0E-4,0.0');
model.geom('geom1').feature('BLK33').set('axis', {'0' '0' '1'});
model.geom('geom1').feature('BLK33').set('size', {'2.0E-5' '0.0010' '2.0E-4'});
model.geom('geom1').feature('BLK33').set('pos', '1.8E-4,-5.0E-4,0.0');
model.geom('geom1').feature('BLK34').set('axis', {'0' '0' '1'});
model.geom('geom1').feature('BLK34').set('size', {'2.0E-5' '0.0010' '2.0E-4'});
model.geom('geom1').feature('BLK34').set('pos', '-5.0E-4,-5.0E-4,0.0');
model.geom('geom1').feature('BLK35').set('axis', {'0' '0' '1'});
```

```
model.geom('geom1').feature('BLK35').set('size', {'2.0E-5' '0.0010' '2.0E-4'});
model.geom('geom1').feature('BLK35').set('pos', '2.2E-4,-5.0E-4,0.0');
model.geom('geom1').feature('BLK36').set('axis', {'0' '0' '1'});
model.geom('geom1').feature('BLK36').set('size', {'2.0E-5' '0.0010' '2.0E-4'});
model.geom('geom1').feature('BLK36').set('pos', '2.6000000000000003E-4,-5.0E-4,0.0');
model.geom('geom1').feature('BLK4').set('axis', {'0' '0' '1'});
model.geom('geom1').feature('BLK4').set('size', {'2.0E-5' '0.0010' '2.0E-4'});
model.geom('geom1').feature('BLK4').set('pos', '3.0000000000000003E-4,-5.0E-4,0.0');
model.geom('geom1').feature('BLK5').set('axis', {'0' '0' '1'});
model.geom('geom1').feature('BLK5').set('size', {'2.0E-5' '0.0010' '2.0E-4'});
model.geom('geom1').feature('BLK5').set('pos', '3.4E-4,-5.0E-4,0.0');
model.geom('geom1').feature('BLK6').set('axis', {'0' '0' '1'});
model.geom('geom1').feature('BLK6').set('size', {'2.0E-5' '0.0010' '2.0E-4'});
model.geom('geom1').feature('BLK6').set('pos', '3.8E-4,-5.0E-4,0.0');
model.geom('geom1').feature('BLK7').set('axis', {'0' '0' '1'});
model.geom('geom1').feature('BLK7').set('size', {'2.0E-5' '0.0010' '2.0E-4'});
model.geom('geom1').feature('BLK7').set('pos', '4.2E-4,-5.0E-4,0.0');
model.geom('geom1').feature('BLK8').set('axis', {'0' '0' '1'});
model.geom('geom1').feature('BLK8').set('size', {'2.0E-5' '0.0010' '2.0E-4'});
model.geom('geom1').feature('BLK8').set('pos', '4.6E-4,-5.0E-4,0.0');
model.geom('geom1').feature('BLK9').set('axis', {'0' '0' '1'});
model.geom('geom1').feature('BLK9').set('size', {'2.0E-5' '0.0010' '2.0E-4'});
model.geom('geom1').feature('BLK9').set('pos', '-4.6E-4,-5.0E-4,0.0');
model.geom('geom1').setGeom('C:\Users\cantilever\Desktop\MT_COMSOL\CodeModels\MT_1mmx1mmx
20um_100umLegs_Ridges_h15_p500mW_geom1.mphbin');

model.material.create('mat1');
model.material('mat1').propertyGroup.create('Enu',  'Young''s  modulus  and  Poisson''s
ratio');
model.material('mat1').propertyGroup.create('RefractiveIndex', 'Refractive index');

model.physics.create('ht', 'HeatTransfer', 'geom1');
model.physics('ht').feature.create('hs1', 'HeatSource', 3);
model.physics('ht').feature('hs1').selection.set([8 23]);
model.physics('ht').feature.create('temp1', 'TemperatureBoundary', 2);
model.physics('ht').feature('temp1').selection.set([1 324]);
model.physics('ht').feature.create('hf1', 'HeatFluxBoundary', 2);
model.physics('ht').feature('hf1').selection.set([2 3 4 5 6 7 8 9 11 12 14 15 16 17 18 20
21 22 23 24 25 26 27 28 30 31 32 33 34 35 36 38 39 45 46 47 48 49 50 52 55 56 57 58 59 60
61 63 66 67 68 69 70 71 72 74 77 78 79 80 81 82 83 85 88 89 90 91 92 93 94 96 99 100 101
102 103 104 105 107 110 111 112 113 114 115 116 118 121 122 123 124 125 126 127 129 132 133
134 135 136 137 139 140 142 143 145 148 150 151 152 154 155 156 157 158 159 161 163 165 166
167 168 170 171 172 173 174 175 177 178 179 180 184 186 187 189 192 193 194 195 196 197 198
199 200 201 203 206 207 208 209 210 211 212 213 214 215 217 220 221 222 223 224 225 226 228
231 232 233 234 235 236 237 239 242 243 244 245 246 247 248 250 253 254 255 256 257 258 259
261 264 265 266 267 268 269 270 272 275 276 277 278 279 280 281 283 286 287 288 289 290 291
292 294 297 298 299 300 302 303 305 306 307 308 309 311 312 313 314 316 317 319 320 321 322
323]);

model.mesh.create('mesh1', 'geom1');
% The mesh object below is lost and cannot be exported
model.mesh('mesh1').feature.create('obj', 'MeshObject');
model.mesh.create('mesh2', 'geom1');
model.mesh('mesh2').feature.create('ftet1', 'FreeTet');

model.material('mat1').name('Silicon');
model.material('mat1').propertyGroup('def').set('heatcapacity', '703[J/(kg*K)]');
model.material('mat1').propertyGroup('def').set('thermalexpansioncoefficient',    {'4.15e-
6[1/K]' '0' '0' '0' '4.15e-6[1/K]' '0' '0' '0' '4.15e-6[1/K]'});
model.material('mat1').propertyGroup('def').set('relpermittivity',  {'12.1'  '0'  '0'  '0'
'12.1' '0' '0' '0' '12.1'});
model.material('mat1').propertyGroup('def').set('thermalconductivity', {'163[W/(m*K)]' '0'
'0' '0' '163[W/(m*K)]' '0' '0' '0' '163[W/(m*K)]'});
model.material('mat1').propertyGroup('def').set('relpermeability', {'1' '0' '0' '0' '1' '0'
'0' '0' '1'});
model.material('mat1').propertyGroup('def').set('density', '2330[kg/m^3]');
model.material('mat1').propertyGroup('def').set('electricconductivity', {'1e-12[S/m]' '0'
'0' '0' '1e-12[S/m]' '0' '0' '0' '1e-12[S/m]'});
model.material('mat1').propertyGroup('Enu').set('youngsmodulus', '131E9[Pa]');
model.material('mat1').propertyGroup('Enu').set('poissonsratio', '0.27');
model.material('mat1').propertyGroup('RefractiveIndex').set('n', '');
```

```
model.material('mat1').propertyGroup('RefractiveIndex').set('ki', '');
model.material('mat1').propertyGroup('RefractiveIndex').set('n', {'3.48' '0' '0' '0' '3.48'
'0' '0' '0' '3.48'});
model.material('mat1').propertyGroup('RefractiveIndex').set('ki', {'0' '0' '0' '0' '0' '0'
'0' '0' '0'});

model.physics('ht').feature('solid1').set('minput_frequency', 'freq');
model.physics('ht').feature('os1').set('minput_frequency', 'freq');
model.physics('ht').feature('init1').set('T', '293.15');
model.physics('ht').feature('hs1').set('Q', '250e-3/(0.4e-3*0.9e-3*2e-6)');
model.physics('ht').feature('temp1').set('T0', '293.15');
model.physics('ht').feature('hf1').set('HeatFluxType', 'InwardHeatFlux');
model.physics('ht').feature('hf1').set('h', '50');
model.physics('ht').feature('hf1').set('Text', '293.15');

model.mesh('mesh1').feature('obj').set('filename', '$FILENAME$_mesh1_obj.mphbin');
model.mesh('mesh1').run;
model.mesh('mesh2').feature('size').set('hauto', 8);
model.mesh('mesh2').run;

model.study.create('std1');
model.study('std1').feature.create('time', 'Transient');

model.sol.create('sol1');
model.sol('sol1').study('std1');
model.sol('sol1').attach('std1');
model.sol('sol1').feature.create('st1', 'StudyStep');
model.sol('sol1').feature.create('v1', 'Variables');
model.sol('sol1').feature.create('t1', 'Time');
model.sol('sol1').feature('t1').feature.create('fc1', 'FullyCoupled');
model.sol('sol1').feature('t1').feature.create('d1', 'Direct');
model.sol.create('sol2');
model.sol('sol2').study('std1');

model.study('std1').feature('time').set('initstudyhide', 'on');
model.study('std1').feature('time').set('initsolhide', 'on');
model.study('std1').feature('time').set('notstudyhide', 'on');
model.study('std1').feature('time').set('notsolhide', 'on');

model.result.create('pg1', 'PlotGroup3D');
model.result('pg1').feature.create('vol1', 'Volume');

model.study('std1').feature('time').set('rtolactive', true);
model.study('std1').feature('time').set('mesh', {'geom1' 'mesh1'});
model.study('std1').feature('time').set('tlist', 'range(0,0.1,3)');

model.sol('sol1').attach('std1');
model.sol('sol1').feature('st1').name('Compile Equations: Time Dependent');
model.sol('sol1').feature('st1').set('studystep', 'time');
model.sol('sol1').feature('v1').set('control', 'time');
model.sol('sol1').feature('t1').set('storeudot', false);
model.sol('sol1').feature('t1').set('control', 'time');
model.sol('sol1').feature('t1').set('tlist', 'range(0,0.1,3)');
model.sol('sol1').feature('t1').set('bwinitstepfrac', '1.0');
model.sol('sol1').feature('t1').set('atolglobalmethod', 'unscaled');
model.sol('sol1').feature('t1').set('solfile', false);
model.sol('sol1').feature('t1').feature('fc1').active(false);
model.sol('sol1').feature('t1').feature('fc1').set('damp', '1.0');
model.sol('sol1').feature('t1').feature('fc1').set('ratelimitactive', true);
model.sol('sol1').feature('t1').feature('d1').set('linsolver', 'spooles');
model.sol('sol1').feature('t1').feature('d1').set('errorchk', 'off');
model.sol('sol2').name('COMSOL 3.5a Solution');
model.sol('sol2').runAll;

model.result('pg1').set('data', 'dset2');
model.result('pg1').set('solnum', '31');
model.result('pg1').set('solrepresentation', 'solnum');

model.name('CADENCE_1mmx1mmx20um_100umLegs_Ridges_CONVECTION.mph');

model.geom('geom1').feature('BLK10').setIndex('size', '5.0E-4', 2);
```

```
model.geom('geom1').runPre('fin');
model.geom('geom1').feature('BLK14').setIndex('size', '5.0E-4', 2);
model.geom('geom1').feature('BLK15').setIndex('size', '5.0E-4', 2);
model.geom('geom1').feature('BLK17').setIndex('size', '5.0E-4', 2);
model.geom('geom1').feature('BLK18').setIndex('size', '5.0E-4', 2);
model.geom('geom1').feature('BLK19').setIndex('size', '5.0E-4', 2);
model.geom('geom1').feature('BLK2').setIndex('size', '5.0E-4', 2);
model.geom('geom1').runPre('fin');
model.geom('geom1').feature('BLK20').setIndex('size', '5.0E-4', 2);
model.geom('geom1').feature('BLK24').setIndex('size', '5.0E-4', 2);
model.geom('geom1').feature('BLK26').setIndex('size', '5.0E-4', 2);
model.geom('geom1').feature('BLK28').setIndex('size', '5.0E-4', 2);
model.geom('geom1').feature('BLK3').setIndex('size', '5.0E-4', 2);
model.geom('geom1').feature('BLK30').setIndex('size', '5.0E-4', 2);
model.geom('geom1').feature('BLK31').setIndex('size', '5.0E-4', 2);
model.geom('geom1').feature('BLK32').setIndex('size', '5.0E-4', 2);
model.geom('geom1').feature('BLK33').setIndex('size', '5.0E-4', 2);
model.geom('geom1').feature('BLK34').setIndex('size', '5.0E-4', 2);
model.geom('geom1').feature('BLK35').setIndex('size', '5.0E-4', 2);
model.geom('geom1').feature('BLK36').setIndex('size', '5.0E-4', 2);
model.geom('geom1').feature('BLK4').setIndex('size', '5.0E-4', 2);
model.geom('geom1').feature('BLK5').setIndex('size', '5.0E-4', 2);
model.geom('geom1').feature('BLK6').setIndex('size', '5.0E-4', 2);
model.geom('geom1').feature('BLK7').setIndex('size', '5.0E-4', 2);
model.geom('geom1').feature('BLK8').setIndex('size', '5.0E-4', 2);
model.geom('geom1').feature('BLK9').setIndex('size', '5.0E-4', 2);
model.geom('geom1').runPre('fin');
model.geom('geom1').run;

model.mesh.remove('mesh1');
model.mesh.remove('mesh2');
model.mesh.create('mesh1', 'geom1');
model.mesh('mesh1').run;

model.result('pg1').run;
model.result('pg1').run;
model.result.dataset.create('cpt1', 'CutPoint1D');
model.result.create('pg2', 'PlotGroup1D');
model.result('pg2').run;
model.result.dataset('cpt1').set('pointx', '0');
model.result('pg2').run;
model.result('pg2').set('ylabelactive', 'on');
model.result('pg2').set('ylabel', 'Temperature [K]');
model.result('pg2').set('xlabelactive', 'on');
model.result('pg2').set('xlabel', 'Time [sec]');
model.result.numerical.create('av1', 'AvSurface');
model.result.numerical('av1').selection.set([26]);
model.result.dataset.remove('cpt1');
model.result('pg2').run;
model.result.remove('pg2');
model.result('pg1').run;
model.result('pg1').run;
model.result.remove('pg1');

model.sol('sol1').runAll;

model.result.export.create('img1', 'Image3D');
model.result.export('img1').set('unit', 'px');
model.result.export('img1').set('height', '600');
model.result.export('img1').set('width', '800');
model.result.export('img1').set('lockratio', 'off');
model.result.export('img1').set('resolution', '96');
model.result.export('img1').set('size', 'manual');
model.result.export('img1').set('antialias', 'on');
model.result.export('img1').set('title', 'on');
model.result.export('img1').set('legend', 'on');
model.result.export('img1').set('logo', 'on');
model.result.export('img1').set('options', 'off');
model.result.export('img1').set('fontsize', '9');
model.result.export('img1').set('customcolor', [1 1 1]);
model.result.export('img1').set('background', 'color');
```

```
model.result.export('img1').set('qualitylevel', '92');
model.result.export('img1').set('qualityactive', 'off');
model.result.export('img1').set('imagetype', 'png');
model.result.export('img1').set('axisorientation', 'on');
model.result.export('img1').set('grid', 'on');
model.result.export.create('plot1', 'Plot');
model.result.export.remove('img1');
model.result.export.remove('plot1');
model.result.create('pg1', 'PlotGroup3D');
model.result('pg1').run;
model.result('pg1').set('data', 'dset1');
model.result('pg1').feature.create('vol1', 'Volume');
model.result('pg1').run;
model.result('pg1').run;

model.physics('ht').feature('hf1').set('h', 1, '5');

model.sol('sol1').runAll;

model.result('pg1').run;

model.physics('ht').feature('hf1').set('h', 1, '500');

model.sol('sol1').runAll;

model.result('pg1').run;

model.physics('ht').feature('hf1').set('h', 1, '100');

model.sol('sol1').runAll;

model.result('pg1').run;
model.result('pg1').run;
model.result('pg1').run;

model.physics('ht').feature('hf1').set('h', 1, '223');

model.sol('sol1').runAll;

model.result('pg1').run;

model.physics('ht').feature('hf1').set('h', 1, '75');

model.sol('sol1').runAll;

model.result('pg1').run;

model.physics('ht').feature('hf1').set('h', 1, '25');

model.sol('sol1').runAll;

model.result('pg1').run;

model.physics('ht').feature('hf1').set('h', 1, '20');

model.sol('sol1').runAll;

model.result('pg1').run;

model.physics('ht').feature('hf1').set('h', 1, '10');

model.sol('sol1').runAll;

model.result('pg1').run;

model.physics('ht').feature('hf1').set('h', 1, '15');

model.sol('sol1').runAll;

model.result('pg1').run;
```

```
model.physics('ht').feature('hs1').set('Q', 1, '0.5*275e-3/(0.4e-3*0.9e-3*2e-6)');

model.sol('sol1').runAll;

model.result('pg1').run;

model.name('MT_1mmx1mmx20um_100umLegs_Ridges.mph');

model.result('pg1').run;
model.result.table.create('tbl1', 'Table');
model.result.table('tbl1').comments('Surface Average 1 (T)');
model.result.numerical('av1').set('table', 'tbl1');
model.result.numerical('av1').setResult;
model.result.create('pg2', 1);
model.result('pg2').set('data', 'none');
model.result('pg2').feature.create('tblp1', 'Table');
model.result('pg2').feature('tblp1').set('table', 'tbl1');
model.result('pg2').run;

model.physics('ht').feature('hs1').set('Q', 1, '250e-3/(0.4e-3*0.9e-3*2e-6)');

model.sol('sol1').runAll;

model.result('pg1').run;
model.result('pg2').run;
model.result('pg2').feature('tblp1').set('linestyle', 'dotted');
model.result('pg2').feature('tblp1').set('linecolor', 'blue');
model.result('pg2').feature('tblp1').set('linestyle', 'cycle');
model.result('pg2').feature('tblp1').set('linewidth', '1');
model.result('pg2').feature('tblp1').set('linemarker', 'none');
model.result('pg2').feature('tblp1').set('legend', 'on');
model.result('pg2').run;
model.result('pg2').run;
model.result('pg1').run;
model.result('pg2').run;
model.result.table('tbl1').save('C:\Users\cantilever\Desktop\MT_COMSOL\Figures\MT_1x1_Tau
Plot_h15.txt');
model.result.table('tbl1').save('C:\Users\cantilever\Desktop\MT_COMSOL\Figures\MT_1x1_Tau
Plot_h15.csv');
model.result('pg1').run;
model.result('pg1').run;

model.name('MT_1mmx1mmx20um_100umLegs_Ridges.mph');

model.result('pg1').run;
model.result('pg2').run;
model.result.numerical('av1').set('table', 'tbl1');
model.result.numerical('av1').appendResult;
model.result('pg2').run;
model.result('pg1').run;
model.result('pg2').run;
model.result('pg2').run;
model.result('pg2').run;
model.result('pg2').run;
model.result.remove('pg2');
model.result.numerical('av1').set('table', 'tbl1');
model.result.numerical('av1').appendResult;
model.result('pg1').run;
model.result.create('pg2', 1);
model.result('pg2').set('data', 'none');
model.result('pg2').feature.create('tblp1', 'Table');
model.result('pg2').feature('tblp1').set('table', 'tbl1');
model.result('pg2').run;
model.result('pg2').run;
model.result.remove('pg2');
model.result.table.create('tbl2', 'Table');
model.result.table('tbl2').comments('Surface Average 1 (T)');
model.result.numerical('av1').set('table', 'tbl2');
model.result.numerical('av1').setResult;
model.result.create('pg2', 1);
model.result('pg2').set('data', 'none');
```

```
model.result('pg2').feature.create('tblp1', 'Table');
model.result('pg2').feature('tblp1').set('table', 'tbl2');
model.result('pg2').run;

model.physics('ht').feature('hf1').set('h', 1, '50');

model.sol('sol1').runAll;

model.result('pg1').run;
model.result('pg2').run;
model.result('pg1').run;
model.result('pg2').run;
model.result.remove('pg2');
model.result.table.create('tbl3', 'Table');
model.result.table('tbl3').comments('Surface Average 1 (T)');
model.result.numerical('av1').set('table', 'tbl3');
model.result.numerical('av1').setResult;
model.result.create('pg2', 1);
model.result('pg2').set('data', 'none');
model.result('pg2').feature.create('tblp1', 'Table');
model.result('pg2').feature('tblp1').set('table', 'tbl3');
model.result('pg2').run;
model.result('pg1').run;
model.result.table('tbl3').save('C:\Users\cantilever\Desktop\MT_COMSOL\Figures\MT_1x1_Tau
Plot_h50_p500mW.csv');

model.physics('ht').feature('hf1').set('h', 1, '15');

model.result('pg2').run;
model.result.remove('pg2');

model.sol('sol1').runAll;

model.result('pg1').run;
model.result.table.create('tbl4', 'Table');
model.result.table('tbl4').comments('Surface Average 1 (T)');
model.result.numerical('av1').set('table', 'tbl4');
model.result.numerical('av1').setResult;
model.result.create('pg2', 1);
model.result('pg2').set('data', 'none');
model.result('pg2').feature.create('tblp1', 'Table');
model.result('pg2').feature('tblp1').set('table', 'tbl4');
model.result('pg2').run;
model.result.table('tbl4').save('C:\Users\cantilever\Desktop\MT_COMSOL\Figures\MT_1x1_Tau
Plot_h15_p500mW.csv');
model.result('pg1').run;

out = model;
```

REFERENCES

1. Li, M., Biswas, S., Nantz, M., et al., A microfabricated preconcentration device for breath analysis. Sensors and Actuators B: Chemical, vol. 180, pp. 130-136, April, 2013.
2. Liu, F., Li, F., Khademhosseini, A., et al., Multiparametric MEMS Biosensors With Integrated Impedance Spectroscopy and Gravimetric Measurements for Water Toxicity Sensing. ASME 2013 2nd Global Congree on NanoEngineering for Medicine and Biology, Boston, Massachusetts, USA, February 4-6, 2013.
3. Lahlou, H., X. Vilanova, and X. Correig, Gas phase micro-preconcentrators for benzene monitoring: A review. Sensors and Actuators B: Chemical, vol. 176, pp. 198-210, January, 2013.
4. Korotcenkov, G. and B.K. Cho, Engineering approaches for the improvement of conductometric gas sensor parameters: Part 1. Improvement of sensor sensitivity and selectivity (short survey). Sensors and Actuators B: Chemical, vol. 188, pp. 709-728, November, 2013.
5. Fouletier, J. and P. Fabry, Chemical and biological microsensors : applications in liquid media. 2010, London Hoboken, NJ: ISTE ;Wiley. 1 online resource (xii, 340 pages).
6. Lazarus, N., S.S. Bedair, and C.C. Lo, CMOS-MEMS capacitive humidity sensor. Journal of Microelectromechanical Systems, vol. 19, 1, pp. 183-191, February, 2010.
7. Zampolli, S., Elmi, I., Mancarella, F., et al., Real-time monitoring of sub-ppb concentrations of aromatic volatiles with a MEMS-enabled miniaturized gas-chromatograph. Sensors and Actuators B: Chemical, vol. 141, 1, pp. 322-328, Aug 2009.
8. Boisen, A. and T. Thundat, Design & fabrication of cantilever array biosensors. Materials today, 2009.
9. Senesac, L. and T.G. Thundat, Nanosensors for trace explosive detection. materials today, 2008.
10. Elmi, I., Zampolli, S., Cozzani, E., et al., Development of ultra-low-power consumption MOX sensors with ppb-level VOC detection capabilities for emerging applications. Sensors and Actuators B: Chemical, vol. 135, 1, pp. 342-351, Dec, 2008.
11. Lang, H.P. and C. Gerber, Microcantilever sensors. STM and AFM studies on (bio) molecular systems: Unraveling the Nano World, vol. 285, 2008.
12. Seo, J.H. and O. Brand, High-Factor In-Plane-Mode Resonant Microsensor Platform for Gaseous/Liquid Environment. Microelectromechanical Systems, 2008.
13. McDonagh, C., C.S. Burke, and B.D. MacCraith, Optical chemical sensors. Chemical reviews, 2008. 108(2): p. 400-422.
14. Zellers, E., Reidy, S., Veeneman, R., et al, An integrated micro-analytical system for complex vapor mixtures. Solid-State Sensors, 2007.
15. Wright, L.K., Collin, W., Serrano, G., et al., Microfabricated gas chromatograph for rapid, trace-level determinations of gas-phase explosive marker compounds. Analytical Chemistry, vol. 86, 1, 2013.
16. Park, J., Cai, Q., Heldsinger, D., et al., Vapor recognition with an integrated array of polymer-coated flexural plate wave sensors. Sensors and Actuators B: Chemical, vol 62, 2, pp 121-130, 2000.
17. Serrano, G., T. Sukaew, and E.T. Zellers, Hybrid preconcentrator/focuser module for determinations of explosive marker compounds with a micro-scale gas chromatograph. Journal of Chromatography A, 2013.
18. Akbar, M. and M. Agah, A microfabricated propofol trap for breath-based anesthesia depth monitoring. Microelectromechanical Systems, 2013.
19. Dow, A.B.A. and W. Lang, Design and fabrication of a micropreconcentrator focuser for sensitivity enhancement of chemical sensing systems. Sensors Journal, 2012.
20. Vellekoop, M.J., Acoustic wave sensors. Theory, design and physicochemical applications: by D.S. Ballantine, R.M. White, S.J. Martin, A.J. Ricco, E.T. Zellers, G.C. Frye and H. Wohltjen, published by Academic Press, San Diego, 1997, ISBN 0-12-077460-7, 436 pages. Sensors and Actuators A: Physical, 1997. 63(1): p. 79.
21. Hoover, A., et al., Improved performance of micro-fabricated preconcentrators using silica nanoparticles as a surface template. Journal of Chromatography A, 2013.
22. Narayanan, S. and M. Agah, Fabrication and characterization of a suspended TCD integrated with a gas separation column. Journal of Microelectromechanical Systems, vol 22, 5, 2013.
23. Chang, H., J. Bryant-Genevier, and E.T. Zellers, Microfabricated gas chromatograph for on-site determination of trichloroethylene in indoor air arising from vapor intrusion. 1. Field evaluation. Environmental science & technology, vol 46, 11, 2012.
24. Wong, M.Y., et al., A preconcentrator chip employing μ-SPME array coated with in-situ-synthesized carbon adsorbent film for VOCs analysis. Talanta, 2012.
25. Li, M., et al., Preconcentration and analysis of trace volatile carbonyl compounds. Analytical chemistry, 2012.
26. Mohsen, Y., et al., Selection and characterization of adsorbents for the analysis of an explosive-related molecule traces in the air. Sensors and Actuators B: Chemical, 2013.
27. Ashraf-Khorassani, M., L.T. Taylor, and M. Agah, MEMS-based multi-inlet/outlet preconcentrator coated by inkjet printing of polymer adsorbents. Sensors and Actuators B: Chemical, 2008.
28. Sukaew, T., et al., Multi-stage preconcentrator/focuser module designed to enable trace level determinations of trichloroethylene in indoor air with a microfabricated gas chromatograph. Analyst, 2011.
29. Lu, C.J., S.W. Pang, and E.T. Zellers, Multiple-stage microfabricated preconcentrator-focuser for micro gas chromatography system. Journal of Microelectromechanical Systems, 2005.
30. Alfeeli, B. and M. Agah, Selective preconcentration by temperature manipulation of cascaded Micro preconcentrators. Solid-State Sensors, 2009.
31. Alfeeli, B. and M. Agah, Micro preconcentrator with embedded 3D pillars for breath analysis applications. Sensors, 2008.
32. Pang, S.W., C.J. Lu, and E.T. Zellers, High sensitivity three-stage microfabricated preconcentrator-focuser for micro gas chromatography. Transducers, Solid State sensors, Actuators and Microsystems, 2003.
33. Pang, S.W., C.J. Lu, and E.T. Zellers, Microfabricated preconcentrator-focuser for a microscale gas chromatograph. Journal of Microelectromechanical Systems, 2003.
34. Lu, C.J. and E.T. Zellers, Multi-adsorbent preconcentration/focusing module for portable-GC/microsensor-array analysis of complex vapor mixtures. Analyst, 2002.

35. Lu, C.J. and E.T. Zellers, A dual-adsorbent preconcentrator for a portable indoor-VOC microsensor system. Analytical chemistry, 2001.
36. Pang, S.W., R.A. Veeneman, and E.T. Zellers, Microfabricated preconcentrator for quantitative analysis of low concentration volatile organic compounds. Solid-State Sensors, 2005.
37. Taylor, L.T. and M. Agah, Design, modeling, and fabrication of MEMS-based multicapillary gas chromatographic columns. Microelectromechamical Systems, vol 18, 1, 2009.
38. Sukaew, T., Micro-scale Preconcentrators for Vapor-Phase Air Contaminants: Optimizing the Design and Operating Conditions for Integration with Micro-scale Gas Chromatographic Instrumentation, University of Michigan, 2013.
39. Zareian-Jahromi, M.A. and M. Agah, Selective micro preconcentration of propofol for anesthetic depth monitoring by using seedless electroplated gold as adsorbent. Engineering in Medicine and Biology Society, 2009.
40. Lahlou, H., et al., A planar micro-concentrator/injector for low power consumption microchromatographic analysis of benzene and 1, 3 butadiene. Microsystem Technologies, vol 18, 4, pp 489-495, 2012.
41. Mohsen, Y., et al., Development of a gas micro-preconcentrator for the analysis of explosive traces: study and characterization of various adsorbing materials. Development of a gas micro-preconcentrator for the analysis of explosive traces: study and characterization of various adsorbing materials, 2012.
42. Narayanan, S., A. Garg, and M. Agah, Matrix GC: Multi-dimensional Analysis/Detection using Integrated Columns. MicroGC: Of Detectors and Columns, 2014.
43. Lalauze, R., Chemical sensors and biosensors. 2012, London, Hoboken, N.J.: Iste ; Wiley. xvi, 429 p.
44. Shakeel, H. and M. Agah, High-performance multicapillary gas separation columns with MPG stationary phases. Sensors, 2011.
45. Kurzawski, P., A. Hierlemann, and E.T. Zellers, Evaluation of multitransducer arrays for the determination of organic vapor mixtures. Analytical chemistry, 2008.
46. Jin, C. and E.T. Zellers, Limits of recognition for binary and ternary vapor mixtures determined with multitransducer arrays. Analytical chemistry, 2008.
47. Barrettino, D., et al., Monolithic CMOS multi-transducer gas sensor microsystem for organic and inorganic analytes. Sensors and Actuators B: Chemical, 2007.
48. Park, J., G.Z. Zhang, and E.T. Zellers, Personal monitoring instrument for the selective measurement of multiple organic vapors. AIHAJ-American Industrial Hygiene Association, Mar/Apr, 61, 2, 2000.
49. Akbar, M., et al., A purge and trap integrated microGC platform for chemical identification in aqueous samples. Analyst, 2014.
50. Lai, H., et al., Identification of volatile chemical signatures from plastic explosives by SPME-GC/MS and detection by ion mobility spectrometry. Analytical and bioanalytical Chemistry, vol 396, 8, 2010.
51. Zhong, Q., W.H. Steinecker, and E.T. Zellers, Characterization of a high-performance portable GC with a chemiresistor array detector. Analyst, 2009.
52. Grall, A.J., E.T. Zellers, and R.D. Sacks, High-speed analysis of complex indoor VOC mixtures by vacuum-outlet GC with air carrier gas and programmable retention. Environmental science & Technology, 2001.
53. Kim, S.K., H. Chang, and E.T. Zellers, Microfabricated gas chromatograph for the selective determination of trichloroethylene vapor at sub-parts-per-billion concentrations in complex mixtures. Analytical chemistry, 2011.
54. Wang, B. and E.V. Anslyn, Chemosensors : principles, strategies, and applications. Wiley series in drug discovery and development. 2011, Hoboken, N.J.: John Wiley and Sons. 1 online resource (x, 498 pages, [12] pages of plates).
55. Alfeeli, B. and M. Agah, MEMS-based selective preconcentration of trace level breath analytes. Sensors Journal, 2009.
56. Hsieh, M.D. and E.T. Zellers, Adaptation and evaluation of a personal electronic nose for selective multivapor analysis. Journal of occupational and environmental Hygiene, 1, 3, 2004.
57. Akbar, M. and M. Agah, A golden micro-trap for anesthetic depth monitoring using human breath samples. MEMS 2012 IEEE 25th International Conference on, 2012.
58. Akbar, M. and M. Agah, VT MEMS Lab., Virginia Tech, Blacksburg, VA, USA. Sensors, 2012.
59. Dietrich, A.M., B. Alfeeli, and M. Agah, The possibilities will take your breath away: breath analysis for assessing environmental exposure. Environmental science & Technology, 2011.
60. Jain, V., et al., Characterization of poly (2, 6-diphenyl-< i> p</i>-phenylene oxide) films as adsorbent for microfabricated preconcentrators. Microchemical Journal, 98, 2, 2011.
61. Alfeeli, B., L.T. Taylor, and M. Agah, Evaluation of Tenax TA thin films as adsorbent material for micro preconcentration applications. Microchemical Journal, 2010.
62. Alfeeli, B. and M. Agah, Micro preconcentrator for handheld diagnostics of cancer biomarkers in breath. Sensors, 2010.
63. Seo, J.H., et al., Microfabricated passive vapor preconcentrator/injector designed for microscale gas chromatography. Lab on a Chip, 2012.
64. Paul, D., et al., Comprehensive two-dimensional gas chromatographic separations with a microfabricated thermal modulator. Analytical Chemistry, 2012.
65. Gorder, K.A., E.M. Dettenmaier, and E.T. Zellers, Microfabricated gas chromatograph for on-site determinations of TCE in indoor air arising from vapor intrusion. 2. spatial/temporal monitoring. Environmental science & technology, 2012.
66. Zellers, E.T., G. Serrano, and H. Chang, A micro gas chromatograph for high-speed determinations of explosive markers. Solid-State Sensors, 2011.
67. Driscoll, J., et al., First-generation hybrid MEMS gas chromatograph. Lab on a Chip, 2005.
68. Lu, C.J., et al., Portable gas chromatograph with tunable retention and sensor array detection for determination of complex vapor mixtures. Analytical chemistry, 2003.
69. Lovette, J., et al., Highly stable surface functionalization of Microgas chromatography columns using layer-by-layer self-assembly of silica nanoparticles. Analytical Chemistry, 2013.
70. Alfeeli, B. and M. Agah, Toward handheld diagnostics of cancer biomarkers in breath: Micro preconcentration of trace levels of volatiles in human breath. Sensors Journal, 2011.
71. Renaghan, L., Z. Hasnain, and M. Agah, A fabrication technology for three-dimensional micro total analysis systems. Journal of Micromechanics and Microengineering, 2010.

72. Alfeeli, B., D. Hogg, and M. Agah, Solid-phase microextraction using silica fibers coated with tenax-TA films. Procedia Engineering, 2010.
73. Alfeeli, B., M.A. Zareian-Jahromi, and M. Agah, Micro preconcentrator with seedless electroplated gold as self-heating adsorbent. Sensors, 2009.
74. Su, J., et al., Assessing polymer sorption kinetics using micromachined resonators. TRANSDUCERS, 2011.
75. Truax, S., Demirci, K., Beardslee, L., et al., Mass-Sensitive Detection of Gas-Phase Volatile Organics Using Disk Microresonators. Analytical Chemistry, 2011.
76. Li, B., et al., Inkjet printed chemical sensor array based on polythiophene conductive polymers. Sensors and Actuators B: Chemical, 2007. 123(2): p. 651-660.
77. Zellers, E.T. and M. Han, Effects of temperature and humidity on the performance of polymer-coated surface acoustic wave vapor sensor arrays. Analytical chemistry, 1996.
78. Zellers, E.T., S.A. Batterman, and M. Han, Optimal coating selection for the analysis of organic vapor mixtures with polymer-coated surface acoustic wave sensor arrays. Analytical chemistry, 1995.
79. Reidy, S., et al., Temperature-programmed GC using silicon microfabricated columns with integrated heaters and temperature sensors. Analytical chemistry, 2007.
80. Jia, C., S.A. Batterman, and E.T. Zellers, Rapid determination of ETS markers with a prototype field-portable GC employing a microsensor array detector. Journal of Environmental Monitoring, 2007.
81. Lu, C.J., C. Jin, and E.T. Zellers, Chamber evaluation of a portable GC with tunable retention and microsensor-array detection for indoor air quality monitoring. Journal of Environmental Monitoring, 2006.
82. Whiting, J.J., et al., A portable, high-speed, vacuum-outlet GC vapor analyzer employing air as carrier gas and surface acoustic wave detection. Analytical chemistry, 2001.
83. Smith, H., E.T. Zellers, and R. Sacks, High-speed, vacuum-outlet GC using atmospheric-pressure air as carrier gas. Analytical Chemistry, 1999.
84. Martin, M.D., T.J. Roussel, and S. Cambron, Performance of stacked, flow-through micropreconcentrators for portable trace detection. International Journal for Ion Mobility Spectrometry, 2010.
85. Zhang, G.Z. and E.T. Zellers, Portable instrument employing a surface acoustic wave sensor with a regenerable reagent coating for direct measurement of 1, 3-butadiene and styrene. Review of scientific instruments, 1995.
86. Collin, W.R., et al., Microfabricated gas chromatograph for rapid, trace-level determinations of gas-phase explosive marker compounds. Analytical Chemistry, 2013.
87. Camara, E.H.M., et al., A micro gas preconcentrator with improved performance for pollution monitoring and explosives detection. Analytica chimica Acta, 2011.
88. Voiculescu, I., R.A. McGill, and M.E. Zaghloul, Micropreconcentrator for enhanced trace detection of explosives and chemical agents. Sensors Journal, 2006.
89. Kummer, A.M., T.P. Burg, and A. Hierlemann, Transient signal analysis using complementary metal oxide semiconductor capacitive chemical microsensors. Analytical chemistry, 2006.
90. Manginell, R.P., D.R. Adkins, and M.W. Moorman, Mass-sensitive microfabricated chemical preconcentrator. Microelectromechanical Systems, 2008.
91. Zellner, P. and M. Agah, A Single-Mask Single-Etch Process for Constructing Three Dimensional Micro Total Analysis Systems. 2008.
92. Hierlemann, A., O. Brand, and H. Baltes, Complementary metal oxide semiconductor cantilever arrays on a single chip: mass-sensitive detection of volatile organic compounds. Analytical Chemistry, 73, 13, 2002.
93. Carron, C., et al., Cantilever-based resonant gas sensors with integrated recesses for localized sensing layer deposition. IEEE Sensors, 2013.
94. Beardslee, L.A., et al., Detection of Anti-IgG Using Cantilever-type Resonant Microstructures Vibrating in In-plane Flexural Modes. IEEE Sensors, 2012.
95. Carron, C., et al., Cantilever-Based Resonant Microsensor with Integrated Temperature Modulation. Hilton Head Solid-State Sensors, Actuators and Microsystems Workshop, 2014.
96. Ohira, S.I. and K. Toda, Micro gas analyzers for environmental and medical applications. Analytica Chimica Acta, 2008.
97. Chiriac, R.E., et al., Development of a pre-concentrator-thermo-desorber/micro-gas chromatograph/mass spectrometer coupling for on-site analyses of emissions of volatile organic compounds from landfills. International Journal of Environmental and Analytical Chemistry, 2007.
98. Waggoner, P.S. and H.G. Craighead, Micro-and nanomechanical sensors for environmental, chemical, and biological detection. Lab on a Chip, 2007.
99. Ho, C., et al., Overview of Sensors and Needs for Environmental Monitoring. Sensors, 2005. 5(1): p. 4-37.
100. Najafi, K., R.D. Sacks, and E.T. Zellers, A wireless integrated microsystem for environmental monitoring. Solid-State Circuits Conference, February, 2004.
101. Tassi, F., et al., Sampling and analytical procedures for the determination of VOCs released into air from natural and anthropogenic sources: A comparison between SPME (Solid Phase Micro Extraction) and ST (Solid Trap) methods. Applied Geochemistry, 2012. 27(1): p. 115-123.
102. Truax, S.B., K.S. Demirci, L.A. Beardslee, et al., Mass-sensitive detection of gas-phase volatile organics using disk microresonators. Analytical Chemistry, 2011.
103. Beardslee, L.A., A.M. Addous, and S. Heinrich, Thermal excitation and piezoresistive detection of cantilever in-plane resonance modes for sensing applications. Microelectromechanical Systems, 2010.
104. Vaswani, S., J. Koskinen, and D.W. Hess, Surface modification of paper and cellulose by plasma-assisted deposition of fluorocarbon films. Surface and Coatings Technology, 2005. 195(2–3): p. 121-129.